RUPRECHT-KARLS-UNIVERSITÄT HEIDELBERG

Sönke Schäfer

Development of a Fully Microfabricated Two Pixel Magnetic Calorimeter

Diploma Thesis

HD-KIP 07-30

KIRCHHOFF-INSTITUT FÜR PHYSIK

Faculty of Physics and Astronomy
University of Heidelberg

Diploma Thesis
in Physics

submitted by
Sönke Schäfer
born in Kronberg

2007

Development of a Fully Microfabricated Two Pixel Magnetic Calorimeter

This diploma thesis has been carried out by Sönke Schäfer
at the Kirchhoff Institute for Physics
under the supervision of
Professor Christian Enss

In the framework of this thesis the feasibility to microfabricate single metallic magnetic calorimeter detectors and detector arrays has been studied. These detectors consist of an absorber for x-rays and a paramagnetic temperature sensor placed in a weak magnetic field. At working temperatures below 100 mK any energy deposition in the detector produces a temperature rise which changes the magnetization of the sensor material. By a read out scheme with sensitive low noise SQUID magnetometers, the absorption of single x-ray quanta can be detected and their energy can be measured precisely. The requirements of an application for high precision spectroscopy in the soft x-ray range on highly charged ions at the Heidelberg EBIT of the MPI for Nuclear Physics was taken into account for the consideration of a suitable detector design. Therefore, the steps of a microfabrication process were developed and optimized. This process allows for a fabrication of calorimeter arrays with mushroom shaped detectors increasing the sensible area by overhanging absorbers. On a single chip, two detectors were fabricated and read out by two separate circuits. Both detectors were characterized and the thermal crosstalk was analysed. In addition to measurements in the flux-locked-loop mode, magnetization measurements and spectra were obtained in open-loop mode. In this mode of operation electrothermal-feedback effects were observed which result in changing the decay times of the pulses. In particular, in this mode faster pulses can be achieved which allows higher count rates.

Entwicklung eines Mikrostrukturierten Magnetischen Kalorimeters mit Zwei Röntgensensoren

Im Rahmen dieser Diplomarbeit wurde die Möglichkeit der Mikrostrukturierung von einzelnen metallischen magnetischen Kalorimetern und von Detektor-Arrays untersucht. Die Detektoren besitzen einen Absorber für Röntgenquanten und einen paramagnetischen Temperatursensor, der sich in einem schwachen Magnetfeld befindet. Bei Betriebstemperaturen unter 100 mK führt bereits ein kleiner Energieeintrag in den Detektor zu einer messbaren Temperaturerhöhung des Sensors. Die damit einhergehende Magnetisierungsänderung des Sensors wird mit Hilfe eines rauscharmen SQUID-Magnetometers nachgewiesen und dient als präzises Maß für die eingetragene Energie. Bei der Entwicklung des Detektors wurden insbesondere die Anforderungen berücksichtigt, die beim Einsatz in geplanten spektroskopischen Untersuchungen an der EBIT am MPI für Kernphysik an ihn gestellt werden. Es wurden Prozessschritte für die Microfabrikation der Detektoren entwickelt und optimiert, die die Herstellung von Kalorimetern mit pilzförmiger Geometrie ermöglichen. In dieser Geometrie mit überhängenden Absorbern kann die sensitive Fläche der Röntgensensoren deutlich vergrößert werden. Der hergestellte Prototyp besitzt zwei separat ausgelesene Röntgensensoren, die gemeinsam auf einem Siliziumsubstrat mikrostrukturiert wurden. Beide wurden eingehend charakterisiert. Desweiteren war es mit dem Aufbau möglich das thermische Übersprechen zwischen den Detektoren zu untersuchen. Zusätzlich zu Messungen im Flux-Locked-Loop Modus wurden auch Magnetisierungsdaten sowie Spektren im Open-Loop Modus aufgezeichnet. Im Open-Loop Modus wurden elektrothermische Rückkopplungseffekte beobachtet, die dazu eingesetzt werden können, die Thermalisierungszeit der Detektoren gezielt zu verkürzen.

Contents

1 Introduction **1**

2 Metallic Magnetic Calorimeters - A Theoretic Approach **3**

2.1 Detection Principle . . . 3

2.2 Sensor Material . . . 4

2.2.1 Erbium doped Gold – Au:Er . . . 5

2.2.2 Heat Capacity and Magnetization . . . 7

2.2.3 Detector Signal . . . 9

2.2.4 Influence of the Nuclear Spin in ^{167}Er . . . 11

2.3 Limiting Factors of the Energy Resolution . . . 13

2.3.1 Limiting Noise Contributions . . . 13

2.3.2 Energy Fluctuations . . . 16

3 Experimental Techniques **23**

3.1 Adiabatic Demagnetization Refrigerator . . . 23

3.2 Superconducting Magnetometers – dc-SQUIDs . . . 25

3.2.1 The dc-SQUID . . . 25

3.2.2 Single Stage SQUID Readout . . . 26

3.2.3 dc-SQUID Noise . . . 27

3.2.4 Two Stage SQUID Readout . . . 28

3.2.5 Data Acquisition . . . 31

3.3 Readout Geometries . . . 32

3.3.1 Meander Shaped Readout Geometry . . . 32

3.3.2 The MagCal 14/15 . . . 34

3.3.3 Wiring . . . 36

3.3.4 Magnetic Field Distribution . . . 36

3.3.5 Signal Size of a Meander Type MMC Detector . . . 38

3.3.6 Magnetic Johnson Noise of a Meander Shaped Detection Coil 39

4 Design considerations for a MagCal 15 **41**

5 Microfabrication **45**

5.1 Sputtering the alloy Au:Er 45

5.2 Microfabricating a detector with overhanging absorber 46

5.2.1 Microstructured detectors on a MagCal 15 chip 48

6 Experimental Results **51**

6.1 Noise at 4K 51

6.2 Noise at Low Temperatures 52

6.3 Magnetization of the Au:Er Sensor 53

6.4 X-Ray Spectroscopy 56

6.4.1 Pulse Shape 56

6.4.2 Pulse Height 57

6.4.3 The X-Ray Spectrum of a ^{55}Fe-Source 58

6.5 Thermal Crosstalk 61

6.6 Detector Operation in Open-Loop Mode 62

6.6.1 Magnetization Measurement 63

6.6.2 Acquisition of Pulses 64

7 Summary **71**

Bibliography **73**

Acknowledgments **75**

1. Introduction

Wilhelm Conrad Röntgen published his observation, made in 1895 while experimenting with cathode rays, in the Würzburgs Physical-Medical Society journal titled "On a new kind of ray: A preliminary communication"[Rön96] only three weeks after their first observance. The nature of these rays were inexplicable at that time, which is the reason why Röntgen gave them the name x-rays. For this discovery he was awarded the first Nobel Prize in 1901. Since then, x-rays have become a powerful tool for investigations in the diverse fields of natural sciences and medical applications.

Astronomy is a field were the observation of x-rays is an important source of information. The x-ray spectrum emitted by interstellar objects like supernovae, the coronas of stars and black holes have recently become accessible by means of space telescopes like Chandra and XMM-Newton. To gain a deeper understanding of these spectra which contain informations on temperature, density and matter composition of the plasmas, reliable laboratory data is necessary. Therefore, x-ray spectroscopic measurements on laboratory plasmas which can be produced and stored in devices like the Heidelberg Electron Beam Ion Trap (EBIT) at the MPI for Nuclear Physics are of major importance. Characteristic radiation emitted by the trapped highly charged ions (HCIs) due to recombinations with free electrons can be studied. The data provides a powerful aid for the interpretation of spectra from satellite missions.

In 1903 Pierre Currie and A. Laborde detected calorically the radiation of a radium source by the heat which it produced in an absorber [CA03]. Today calorimetric detectors are commonly based on a suggestion by F. Simon [Sim35] roughly 25 years ago. To increase the temperature rise in an absorber material, the heat capacity of the calorimeter should be reduced by operating it at low temperatures. The concept of Metallic Magnetic Calorimeters (MMC) has been introduced in 1993 [Ban93b]. It uses the temperature dependence of the magnetization of a paramagnetic sensor material. Due to the energy deposition by an incident x-ray the temperature in the sensor rises which lets the magnetization decrease. This change in magnetization can be read out by a sensitive magnetometer. Opposed to earlier approaches where dielectric materials were used [Büh88], a metallic sensor provides the fast thermalization time needed to effectively detect x-ray photons with a reasonable counting rate. Recently, an energy resolution of $\triangle E_{\mathrm{FWHM}} = 2.7\mathrm{eV}$ was achieved with a MMC type detector [Lin07]. The motivation for the research discussed in this work was to study the possibility of microstructuring detector arrays with high energy resolution in order have the possibility to investigate rare x-ray emission at the EBIT. Moreover the presence of more detectors on the same chip allows the investigation on magnetic and thermal crosstalk.

In the chapters following this introductory part, the principles of a metallic magnetic calorimeter developed in the framework of this thesis are discussed in detail.

A theoretic approach to MMC detectors is given in chapter 2. The calorimetric detection principle of metallic magnetic low temperature detectors is presented. Af-

ter introducing the sensor material Au:Er and the discussion of its thermodynamic properties, like heat capacity and magnetization, the expected detector response is discussed by means of an adequate model. The influence on the detector signal of a nuclear spin carried by the isotope ^{167}Er, present in natural erbium, is simulated and discussed. The last section is devoted to the fundamental limitation of the energy resolution possible to achieve with MMC type detectors.

Chapter 3 will address the technique to reach the temperature range in which the detectors are operated, namely the adiabatic demagnetization refrigeration process. In this context a liquid helium bath cryostat with an ADR stage is presented. The second part of this chapter gives an introduction to the working principle of superconducting magnetometers, so called SQUIDs. The readout of the detector signals with these devices, which depends on a special feedback circuitry that linearize the SQUID signal, is explained. A variety of detector geometries are presented before introducing the chip design used throughout this work in which the readout SQUID is an integral component of the detector chip. For this specific design simulations concerning the expected signal size and the magnetic Johnson noise are discussed.

Regarding certain preconditions, set by the application for x-ray spectroscopy at the Heidelberg EBIT, in chapter 4 the geometric parameters for a new detector design are considered which feature a large sensible area obtained with overhanging absorbers.

To be able to fulfill the geometric parameters resulting from the simulation in chapter 4, a microstructuring process was developed which is introduced in chapter 5. Besides lithographic patterning of photoresists and the etching of the overhanging absorbers, this process includes the sputter deposition of Au:Er thin films. Detailed informations on the parameters used in each single step is given in the text. A two pixels detector was structured onto two meanders with separate readout circuitry, each of them consists of a Au:Er sensor and an overhanging gold absorber.

In chapter 6 the results from spectroscopic measurements obtained irradiating the detectors with a ^{55}Fe source are analyzed and presented. The predicted behavior for the noise of the detector signal, the magnetization of the sensor material and the pulse heights at different temperatures are compared to the experimental results. Also the linearity of the detector in the presented measurement is discussed. In a second part, measurements are presented which were acquired reading out the SQUID in open loop mode. This operation mode has the advantage of a low power dissipation on the chip, which leads to lower sensor temperature and a better energy resolution. Additionally the detectors show electro-thermal-feedback effects which lead to the possibility of making the dacay time of thermal pulses shorter.

2. Metallic Magnetic Calorimeters - A Theoretic Approach

In the previous chapter one energy dispersive and one wavelength dispersive detector, namely a semiconductor detector and a flat crystal spectrometer were discussed. The first having a limited energy resolution but high energy band width, the latter showing a high energy resolution but small band width. In the following sections an energy dispersive detector which combines high energy resolution with broad energy band width is presented and discussed.

2.1 Detection Principle

A Metallic Magnetic Calorimeter (MMC) exploits the calorimetric principle in the sense that it measures the heat caused by the absorption of a particle or x-ray. Fig. 2.1 shows the basic components of such a detector. A metallic absorber is in good thermal contact with a metallic, paramagnetic temperature sensor. The sensor is weakly connected to a thermal bath and positioned in a weak magnetic field. The magnetization of the sensor is precisely monitored by a low noise dc-SQUID magnetometer.

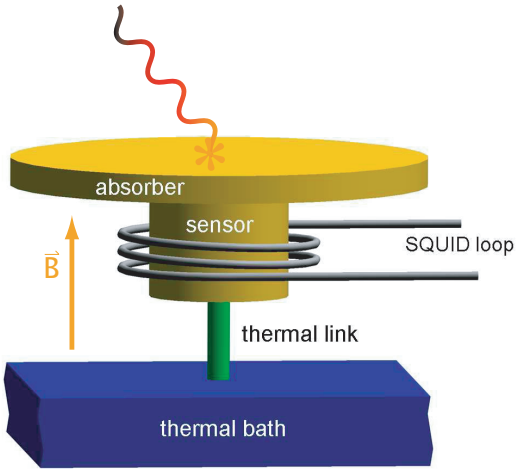

Figure 2.1 Schematic drawing of a magnetic calorimeter.

An energy deposition δE in the absorber-sensor system with the total heat capacity C_{tot} increases the temperature of the system by

$$\delta T = \frac{\delta E}{C_{\mathrm{tot}}} \quad . \tag{2.1}$$

The measurement of the deposited energy can therefore be reduced to a temperature measurement if the total heat capacity of spins and all other degrees of freedom like electrons and phonons, is known.

Due to the paramagnetic behavior of the sensor material, the magnetization M of the sensor decreases by

$$\delta M = \frac{\partial M}{\partial T}\delta T = \frac{\partial M}{\partial T}\frac{\delta E}{C_{\mathrm{tot}}} \ , \tag{2.2}$$

according to the temperature rise δT. In order to get a feeling for the achievable sensitivity of MMCs, we want to consider a set of non interacting magnetic moments with spin $S = 1/2$. An external field effectuates a Zeeman splitting of the states, given by

$$\triangle E_{\mathrm{z}} = g\mu_{\mathrm{B}}B \ , \tag{2.3}$$

where g is the Landé factor and $\mu_{\mathrm{B}} = 9.274 \cdot 10^{-24}\,\mathrm{JT}^{-1}$ the Bohr-magneton. Due to a deposition of energy δE in the system, the number of spins aligned parallel to the magnetic field changes by $\delta N = \delta E/\triangle E_{\mathrm{z}}$. Consequently the magnetization of the system changes according to

$$\delta m = \delta N g\mu_{\mathrm{B}} = \frac{\delta E}{E_{\mathrm{z}}}g\mu_{\mathrm{B}} = \frac{\delta E}{g\mu_{\mathrm{B}}B}g\mu_{\mathrm{B}} = \frac{\delta E}{B} \tag{2.4}$$

As we will see in section 3.2 SQUID-magnetometers provide very sensitive devices to measure magnetization changes. In the following a magnetometer with a sensing coil that is simply given by a circular loop of radius $R = 50\,\mu\mathrm{m}$ is considered. If a cylindrical sensor with dimensions smaller then R is placed in the center of the loop, the magnetic flux changes proportional to the change of the magnetic moment:

$$\delta\phi = \mu_0\frac{G}{R}\delta m \ , \tag{2.5}$$

where μ_0 is the permeability of free space. Assuming that an energy of 5 keV is deposited in a system of non-interacting spins located in a field of $B = 5\,\mathrm{mT}$, the change of flux in the circular loop described above is $\delta\phi \cong 1\,\phi_0$, where ϕ_0 is the magnetic flux quantum. Knowing that modern dc-SQUIDs possess a spectral power density of white flux noise below $1\,\mu\Phi_0/\sqrt{\mathrm{Hz}}$, we can expect the contribution of the magnetometer noise to the energy resolution to be below 1 eV even if integration times well below 1 ms are used. Of course this estimate is somewhat too simple because it ignores all other degrees of freedom of the sensor and absorber material as well as the interaction between the magnetic moments. In the next sections we will step by step include these details in the description of the detector. The measurement of magnetization, an equilibrium thermodynamic property, makes it possible to predict the detector performance if the properties of the magnetic moments as well as the interaction among them and with their surrounding is understood.

2.2 Sensor Material

A sensor in particle and x-ray detection has to have two key characteristics, high sensitivity and a fast thermalization time. Already from equation 2.2 two other re-

quirements on the sensor material can be deduced, a magnetization which depends strongly on temperature and a small total heat capacity. Therefore, first investigations were done as early as 1988 [Büh88] with dielectrics having a small heat capacity, doped with paramagnetic ions which show a strong temperature dependence. Due to the lack of conduction electrons, thermalization times in these materials are only determined by the weak spin-phonon coupling and thus unacceptably long, being of the order of seconds. To overcome this problem metallic hosts for the paramagnetic ions were suggested in 1993 [Ban93a]. Though having to accept an additional heat capacity arising from the electron mediated spin-spin interaction, the strong coupling of conduction electrons to the magnetic moments decrease thermalization times to below microseconds.

2.2.1 Erbium doped Gold – Au:Er

The constituents of the sensor material used in this work are gold (Au) and the rare earth metal erbium (Er). Erbium has an electron configuration of $[\mathrm{Xe}]4f^{12}6s^2$ and thus a $4f$ shell which is only partially filled. Pure gold is diamagnetic and has a face-centered-cubic (fcc) lattice structure. Erbium as a dopant in gold occupies regular fcc

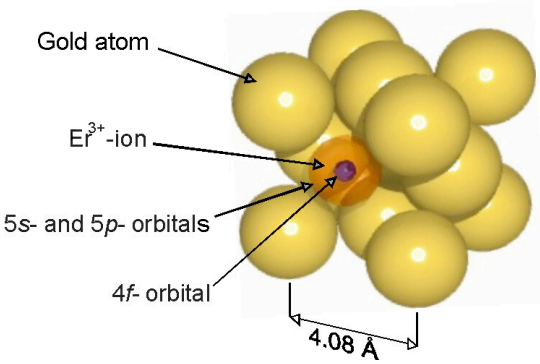

Figure 2.2 Section of a gold fcc lattice where one erbium ion occupies a regular lattice site. The $4f$ shell has a radius of 0.3 Å and lies deep in the ion well sheltered from the crystal field by the outer $5p$ shell of radius 1Å.

lattice sites giving three of its electrons to the conduction band. The resulting Er^{3+} ions have the electron configuration $[\mathrm{Kr}]4d^{10}4f^{11}5s^25p^6$ and thus show paramagnetic behavior due to the permanent magnetic moments of the unpaired electrons in the $4f$ shell. At temperatures below 50 K the magnetic susceptibility of the alloy Au:Er is dominated by the paramagnetic behavior of the erbium ions.

Figure 2.3 shows the magnetic susceptibility of Au doped with 600 ppm erbium in the temperature range between 300 K and 100 μK [Her00, Fle03]. Experimental data is indicated by circles. At temperatures above $T = 100$K the susceptibility is in good agreement with the Curie law[1] for $J = 15/2$ and $g_J = 1.2$. In this temperature region the influence of the crystal field on the paramagnetic behavior of the erbium ions is negligible. The magnetic moment μ can thus be calculated by Hund's rule from the orbital angular momentum $\mathbf{L}$, the spin angular momentum $\mathbf{S}$ and the total

[1] $\chi = \frac{M}{\mu_0 B} = \frac{\mu_0 n g_J^2 J(J+1)\mu_B^2}{3k_B T} = \frac{C}{T}$

angular momentum **J** by

$$\mu = g_J \mathbf{J} \quad , \quad g_J = 1 + \frac{J(J+1) + S(S+1) - L(L+1)}{2J(J+1)} \tag{2.6}$$

where g_J is the Landé factor, having in this case a value of $g_J = 1.2$.

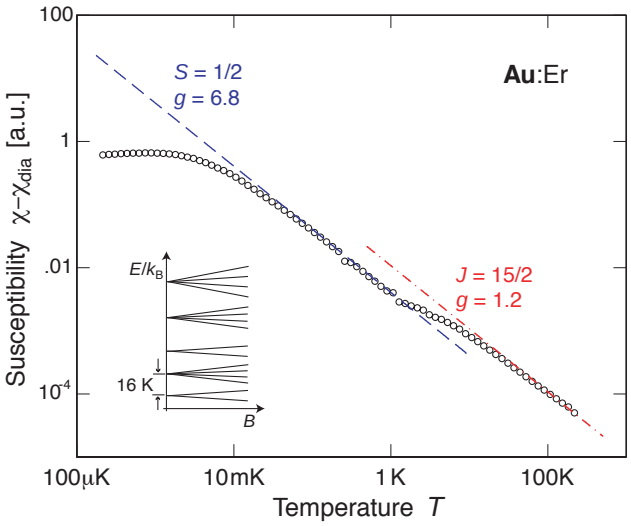

Figure 2.3 Magnetic susceptibility of a Au:Er (600 ppm) sample versus temperature. The diamagnetic contribution by the gold lattice has been subtracted from the experimental data. The dashed lines indicate the Curie law for two different sets of constants (see text). The inset shows a sketch of the energy levels of the erbium ions in an external magnetic field

For temperatures below $T = 100\,\mathrm{K}$ the influence of the crystal field has to be taken into account since it lifts the degenerate energy levels of the Er^{3+} ground state, splitting them into a series of multiplets of which the energetically lowest is a Γ_7-Kramers-doublet. The resulting energy levels are sketched in the inset of fig. 2.3. At zero field the energy splitting between the doublet and the first energetically higher quartet has been measured by several techniques with results between $\triangle E = 11\,K \cdot k_\mathrm{B}$ and $\triangle E = 19\,K \cdot k_\mathrm{B}$ [WH69, Dav73, SS75, Hah92]. Decreasing temperatures lead to a depopulation of the multiplets at higher energies and accordingly to a deviation of the data from the Curie law. At sufficiently low temperatures and small magnetic fields the behavior of erbium in gold is again very well described by a Curie law corresponding to the quasi spin $\tilde{S} = 1/2$ and the effective, isotropic Landé factor of $\tilde{g} = 34/5$ of the Γ_7-Kramers-doublet. For $T < 50\,\mathrm{mK}$ the susceptibility becomes much less temperature dependent since interactions among the spins start to dominate. At temperatures below $T = 0.9\mathrm{mK}$ a maximum can be observed since the transition temperature into a spin glass has been reached.

The temperature range of interest for Metallic Magnetic Calorimeters lies between 20 mK and 100 mK. In this interval the erbium can be treated as a system of magnetic moments with spin 1/2, in which the interaction between the magnetic moments cannot be neglected. In the following, thermodynamic properties and interaction mechanisms of such a system are discussed in order to allow for a numerical calculation of the expected signal size.

2.2.2 Heat Capacity and Magnetization

At temperatures below 100 mK, Er-ions in gold can be described by a system of magnetic moments with two possible orientations in an external magnetic field **B**. The energy eigenvalues of such a system are given by $E_{m_{\tilde{S}}} = m_{\tilde{S}} \tilde{g} \mu_B B$, where $m_{\tilde{S}} = \pm 1/2$ is the magnetic quantum number of the quasi spin $\tilde{S}$, $g_J = 6.8$ the effective

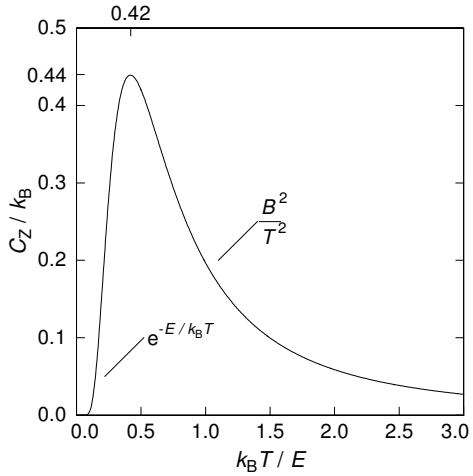

Figure 2.4 Heat capacity versus reduced temperature k_BT/E. Approximations of equation 2.7 for $T \ll E/k_B$ and $T \gg E/k_B$ are given

isotropic Landé factor as described above and B the absolute value of the external magnetic field. The heat capacity C of such a two level system with an energy splitting of $E = \tilde{g}\mu_B B$ is given by the expression

$$C_z = N k_B \left(\frac{E}{k_B T} \right)^2 \frac{e^{E/k_B T}}{(e^{E/k_B T} + 1)^2} \tag{2.7}$$

describing the Schottky anomaly which is pictured in Fig 2.4. The heat capacity has a significant maximum where the thermal energy k_BT equals approximately half the energy splitting E.

The magnetization as a function of temperature and external magnetic field can as well be deduced from equilibrium thermodynamics and we find

$$M = \frac{N}{V} \tilde{g} \mu_B \frac{1}{2} \tanh(h) \tag{2.8}$$

The magnetization is therefore proportional to the density of magnetic moments N/V and to $\tilde{g}\mu_B 1/2$ which is the maximal z-component of the magnetic moment. The factor $\tanh(h)$ represents the relative occupation number difference of magnetic moments aligned parallel and anti parallel to the external magnetic field with argument

$$h = \frac{1/2 \tilde{g} \mu_B B}{k_B T} \propto \frac{B}{T} \ . \tag{2.9}$$

Fig. 2.5 shows the Brillouin function for the present case of $\tilde{S} = 1/2$. Coming from high temperatures where $h \ll 1$ the magnetization is according to the Curie law

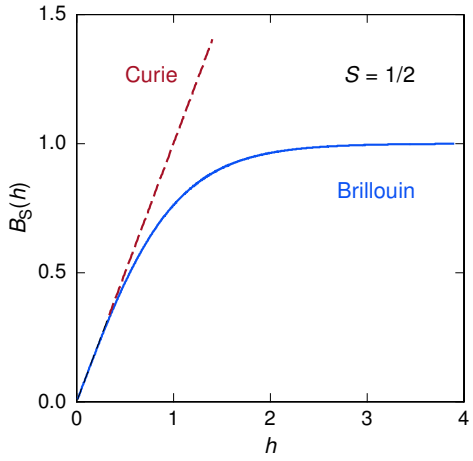

Figure 2.5 For $\tilde{S} = 1/2$ the Brillouin function simplifies to $B_{1/2} = \tanh(h)$. For comparison the Curie law is shown for high temperatures.

proportional to 1/T. At low temperatures ($h \gg 1$) the magnetization starts to saturate as for $T = 0$, all magnetic moments are aligned to the magnetic field and the magnetization reaches its maximum value.

For a thorough understanding of the detector response, reliable methods to calculate the sensor response to an energy deposition are of major importance. Therefore, an accurate theoretical model is needed. For this model the interaction mechanisms among the magnetic moments, namely dipole-dipole interaction and the indirect exchange interaction of Er-ions via the conduction electron, called RKKY[2]-interaction, have to be taken into account. Two approaches were used in previous works [Sch00, Fle03, Dan05] to simulate specific heat and magnetization in the presence of interactions between the magnetic moments, a mean field approximation and a method using the numerical diagonalization of a Hamiltonian which describes clusters of up to 10 interacting spins using periodic boundary conditions. The latter one is used in the following.

On the left in fig. 2.6 the specific heat of a 300 ppm Au:Er sample is shown as a function of temperature for several magnetic fields. Measured data is represented by symbols and the results from the numerical calculation by solid lines. Clearly the temperature of the maximum depends on the magnitude of the external field and the specific heat shows the expected Schottky anomaly. For a system of non interacting spins this maximum would be roughly half as broad. The small contributions to the specific heat by the conduction electrons and phonons of the gold lattice are given. The phononic contribution has been multiplied by a factor of 100 to make it appear in the same range as the other contributions.

In the right diagram of fig. 2.6 a comparison between simulated curves and experimental data for the magnetization is presented for the same sample. The magnetization is plotted as a function of the inverse temperature for different magnetic fields. Towards higher temperatures the magnetization follows the Curie law and for low temperatures, where $\tilde{g}\mu_B B > k_B T$, the expected saturation is visible. Nonetheless, the saturation level lies about 10% lower compared to a system of non interacting

[2]Ruderman-Kittel-Kasuya-Yosida interaction

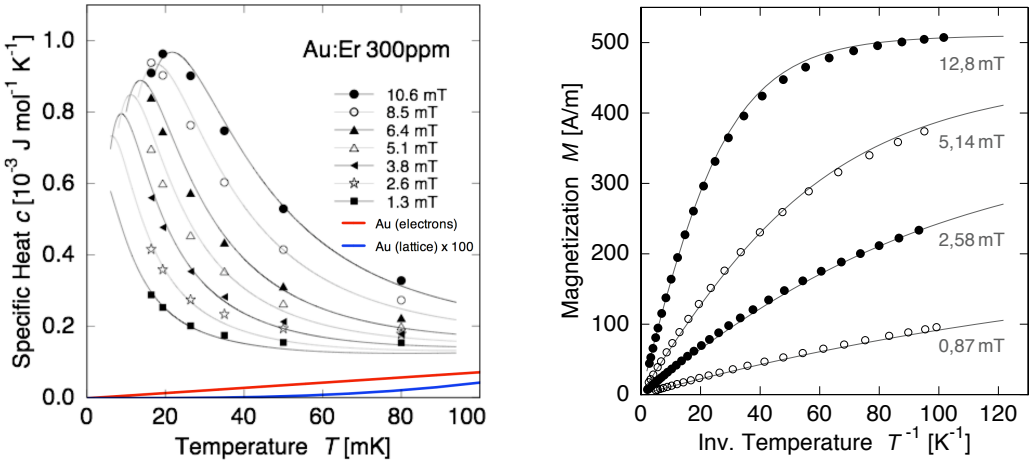

Figure 2.6 Left: Heat capacity versus temperature; Right: Magnetization versus inverse temperature; Simulated data is displayed by solid lines and experimental data by symbols. The measured gold sample was doped with 300 ppm Er, depleted in the isotope ^{167}Er. The fraction of this isotope is only 97.8%.

spins. This is primarily a result of the RKKY-interaction. The good agreement between measured and simulated thermodynamic properties, as was shown here, will be the basis for the calculations of the detector properties in the following sections.

2.2.3 Detector Signal

Even if we have seen that the thermodynamic properties of the sensor material Au:Er can be calculated with confidence, we want to begin our discussion of the signal size of magnetic calorimeters with the simplifying assumption that all the energy absorbed by the detector is deposited in a system of non-interacting spins located in an external field.

In this case, upon the deposition of energy δE, the magnetic moment of the sensor changes by $\delta m = \delta E/B$. If we consider that one spin flip corresponds to a magnetization change of $\delta m = 6.8\,\mu_B$, for an energy deposition of a $\delta E = 5.9\,\text{keV}$ [3] at $T = 50\,\text{mK}$ in a field of $5\,\text{mT}$ approximately 10^9 spins are flipped. If we reconsider the simple geometry from section 2.1, this change in magnetization effectuates a flux change in the magnetometer loop with $R = 50\,\mu\text{m}$ around the sensor of $\delta\phi = \delta m \mu_0 G/r = \phi_0$. So far this simple model neglects all other thermodynamic systems like conduction electrons and phonons as well as the interaction mechanisms between the magnetic moments discussed in section 2.2.2.

To discuss the influence of other thermodynamic systems in our detector setup we have to introduce the absorber used to stop the x-rays. As we will see, the absorber in this work has the dimensions 250x250x5 μm^3 and is made out of high purity gold. The specific heat of a metal is given by $c = \gamma T + \beta T^3$ where $c_e = \gamma T$ is

[3] $\delta E = 5.9\,\text{keV}$ is the energy of the Kα line of Mn^{55} which is commonly used for the calibration of x-ray detectors.

the contribution of the electron system and $c_{\mathrm{ph}} = \beta T^3$ that of the phonon system. For gold $\gamma = 7.3 \cdot 10^{-4}\,\mathrm{J\,mol^{-1}\,K^{-2}}$ and thus for the absorber at 50 mK this contribution to the heat capacity is $C_{\mathrm{e_a}} = 1.1\,\mathrm{pJ/K}$. The contribution by the phononic system is three orders of magnitude smaller ($C_{\mathrm{e_{ph}}} = 1.7\,\mathrm{fJ/K}$) and is therefore neglected in the following. Due to the strong electron-spin coupling, the electron-spin relaxation time is for $T = 50\,\mathrm{mK}$ still $\tau < 1, \mu\mathrm{s}$. Therefore, these two systems are in thermal equilibrium a few microseconds after the absorption of energy.

For the sensor these considerations have been done in section 2.2.2. As can be seen in the left diagram in fig. 2.6, the contribution of the conduction electrons and the phonon system to the specific heat of the sensor are negligible compared to the contribution of the spin system. However, the change of magnetic moment is reduced by the fraction $C_{\mathrm{e}}/(C_{\mathrm{e}}+C_{\mathrm{z}})$ of energy deposited in the system of conduction electrons of the absorber. The fraction of energy absorbed by the system of non-interacting spins goes along with a change of magnetic moment of

$$\delta m = \frac{C_{\mathrm{z}}}{C_{\mathrm{z}} + C_{\mathrm{e}}} \frac{\delta E}{B} \quad . \tag{2.10}$$

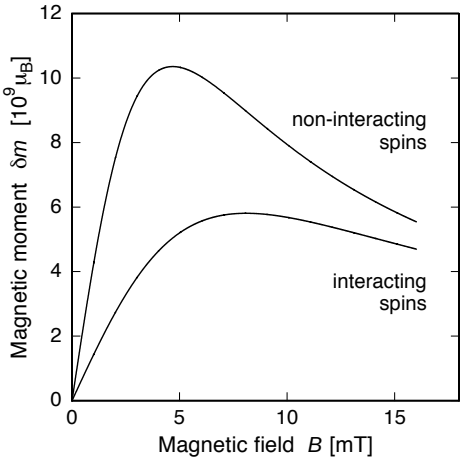

Figure 2.7 Signal size for a MMC with an absorber heat capacity of 1 pJ/K assuming a system of interacting and non interacting spins, respectively, as a function of applied magnetic field at a temperature of $T = 50\,mK$. The gold sensor is doped with 750 ppm erbium. Further details about the detector parameters can be found in the text.

The magnetic field dependence of this detector response is pictured in fig. 2.7. The upper curve represents simulated data for a system of non interacting spins for an absorber with the dimensions mentioned above and a sensor with the dimensions of 160x160x1.5 $\mu\mathrm{m}^3$. For comparison fig. 2.7 shows also the numerically calculated detector response where the RKKY- and the dipole-dipole-interaction is taken into account. In the approximation of small magnetic fields ($\tilde{g}\mu_{\mathrm{B}}B > k_{\mathrm{B}}T$), $C_z \propto B^2$ and thus the signal size increases linearly with the magnetic field. At higher fields the total heat capacity is dominated by the heat capacity of the spin system which leads to $\delta m \propto B^{-1}$. In the limit of very high fields, after having reached the maximum given by the Schottky anomaly, the signal size decreases exponentially. The maximum in signal size is reached in medium magnetic fields where the approximation of

$C_z = qB^2$ is justified, here q is a constant. Therefore, equation 2.10 can be written as

$$\delta m = \frac{qB}{qB^2 + C_\mathrm{e}} \delta E \tag{2.11}$$

and thus the signal size has a maximum where $qB^2 = C_\mathrm{e} = C_\mathrm{z}$.

The lower curve in fig. 2.7 represents simulated data for a system of interacting spins, regarding dipole-dipole- and RKKY-interaction. The simulation was done for the sensor- and absorber dimensions mentioned above. The interaction mechanisms increase the heat capacity and decrease the temperature dependency of the magnetization. Therefore, equation 2.10 has the form

$$\delta m \propto \frac{C_\mathrm{z}}{C_\mathrm{z} + C_\mathrm{e} + C'} \frac{\delta E}{B} \tag{2.12}$$

where C' is the additional heat capacity due to the interaction mechanisms which is almost filed independent under the circumstances discussed here. This leads to a reduction of the maximal signal size. The position of the maximum is now described by $qB^2 = C_\mathrm{e} + C'$ and thus shifted to higher magnetic fields.

2.2.4 Influence of the Nuclear Spin in ^{167}Er

In the natural isotope composition of erbium, the isotope ^{167}Er with an abundance of 23% is the only one that carries a nuclear spin. The influence mentioned in section 2.6 of its nuclear spin of $I = 7/2$ on the detector response can not be neglected. The interaction energy between the magnetic dipole moment of the nucleus and the spin of the electrons is characterized by the hyperfine coupling constant A. For the $^{167}Er^{3+}$ system $A = -0.0335\,K \cdot k_\mathrm{B}$ and the hyperfine enhanced g-factor of the nucleus is $g_\mathrm{N} = -29$ [SS75]. The hyperfine splitting of the Γ_7-Kramers-doublet due to ^{167}Er in

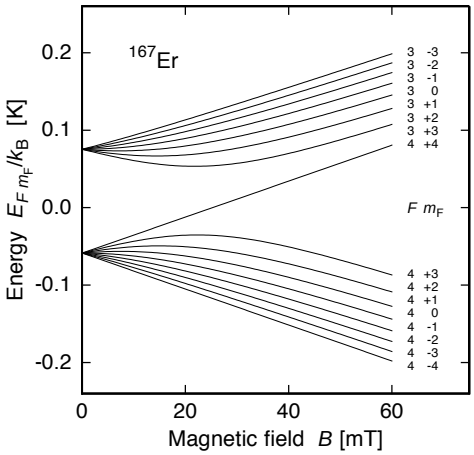

Figure 2.8 Hyperfine splitting of the Γ_7-Kramers-doublet of ^{167}Er in Au as a function of applied magnetic field.

zero field is $140\,\mathrm{mK} \cdot k_\mathrm{B}$. In fig. 2.8 The Zeeman splitting of the energy eigenvalues of the hyperfine levels is shown as a function of an external magnetic field. The

separation into two groups is visible, one at higher energies with the total angular momentum of the nucleus of $F = 3$ and one at lower energies with $F = 4$.

To understand the influence of the detector response, let us assume that the x-ray energy δE is entirely deposited in the ^{167}Er system and that magnetic fields are smaller than 10 mT, as it is typical in the case of MMCs. For the resulting excitation of magnetic moments, there are two cases to consider, excitations with $\triangle F = 0$ and the ones with $\triangle F = 1$. In the first case the z-component of the total angular momentum of the nucleus is $\triangle m_F \neq 0$ and thus the magnetization changes which leads to a detector response. For the second case $\triangle m_F$ can be zero and can have positive and negative sign. Therefore, energy going into these processes does not necessarily change the magnetic moment and in average causes only a negligible contribution to the detector signal.

In fig. 2.9 the influence of this effect on the specific heat can be observed. The specific heat is measured for a gold sample doped with 480 ppm natural erbium and plotted as a function of temperature for five different magnetic fields. Two distinct

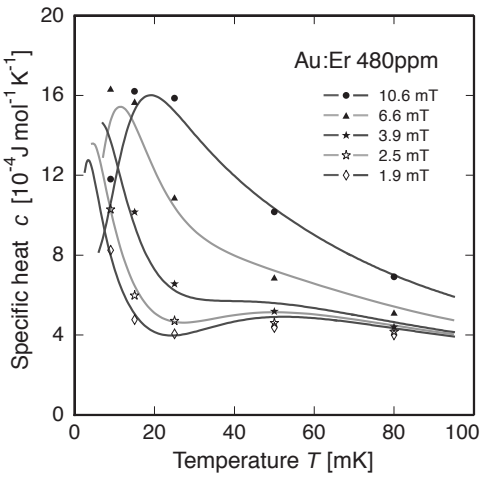

Figure 2.9 Specific heat for a gold sample doped with 480 ppm natural erbium as a function of temperature for different magnetic fields. Measured data is displayed as symbols. Solid lines represent simulated data from a mean field approximation.

maxima are visible. The maximum at low temperature is due to excitations of Er-ions without nuclear spin as well as excitations in ^{167}Er with F=0. The temperature where it is reached is proportional to the magnetic field since the Zeeman splitting of the hyperfine states increases linearly with the magnetic field. The second maximum at $T \approx 55$mK is due to transitions with $\triangle F = 1$ and is nearly independent of the magnetic field. At these temperatures the specific heat of the Au:Er system is dominated by the contribution of the ^{167}Er isotope.

Of course in the real Au:Er system the energy is distributed among all thermodynamic systems, nevertheless this effect will damp the detector signal and thus it is interesting to see to what magnitude this influence is present. In fig. 2.10 the resulting signal size for a detector with a sensor made of natural erbium, with all interaction mechanisms taken into account, is plotted versus the magnetic field. For a comparison the curve from fig. 2.7 which describes the signal of an interacting spin system in the absence of ^{167}Er, is displayed as well. Due to the additional heat capacity that is contributed by the zero-field-splitting of the hyperfine levels in ^{167}Er,

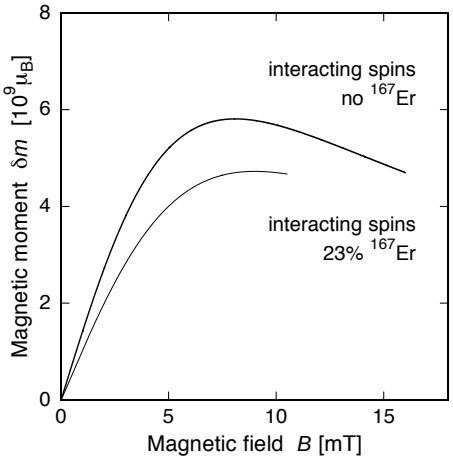

Figure 2.10 Lower curve: Signal size for a MMC with an absorber of heat capacity 1 pJ/K and a gold sensor doped with 750 ppm natural erbium regarding all interaction mechanisms displayed as a function of the applied magnetic field. For comparison, the upper curve from fig. 2.7 regarding only the contribution of spin interaction is displayed as well.

the signal size of a gold sensor doped with natural erbium is reduced.

Since the working temperatures of MMC detectors are in the range of 20 mK to 100 mK, where the heat capacity is strongly influenced by this contribution, only enriched erbium which has the least amount of ^{167}Er should be used as a dopant.

2.3 Limiting Factors of the Energy Resolution

Only a few sources of noise exist which possibly limit the resolution of Metallic Magnetic Calorimeters in a fundamental way. These are the magnetic Johnson noise, the intrinsic noise of the SQUID magnetometer and a noise contribution due to energy fluctuations between the subsystems of the calorimeter and the thermal bath. The discussion of these contributions will reveal some aspects which have to be taken into account for the development and optimization of MMC detectors with high energy resolution.

2.3.1 Limiting Noise Contributions

In general, noise is any undesirable disturbance of the measured signal, nevertheless different types of noise can be determined by their frequency dependence. For instance, a contribution from poorly shielded mains will add discrete lines with a certain width in the spectrum at 50 Hz and its harmonics. Thermal voltage noise in resistors [Nyq28, Joh28] on the other hand is frequency independent, so called white. Practically, noise is a power measured in a certain frequency band $\triangle f$, thus giving it the unit of a power spectral density.

Thermally agitated conduction electrons in normal conducting parts, like sensor and absorber, in the vicinity of the magnetometer loop lead to fluctuations of the magnetic field and thus also of the magnetic flux in the magnetometer. The calculation of this noise contribution will be shown in section 3.3.6.

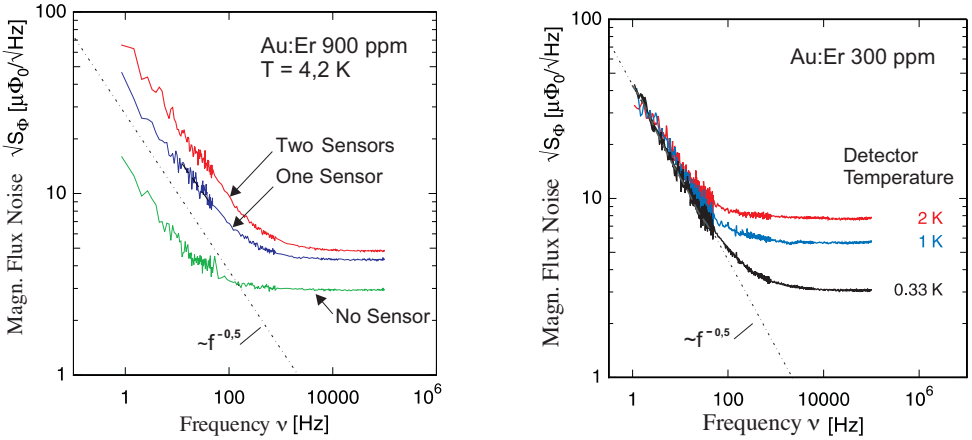

Figure 2.11 Left: noise spectra of a gradiometric SQUID with two 50μm diameter loops. The curves represent the cases where none of the loops, one and both pick up loops are equipped with Au:Er sensors. All curves show the $\sqrt{S_\phi} \propto 1/f$ behavior at low frequencies. Right: comparison of the noise spectra for three different temperatures. Clearly to see there is almost no temperature dependence of the $1/f$ noise contribution.

$1/f$ Noise

At frequencies below 100 Hz the spectral power density of flux noise shows a frequency dependence of

$$\sqrt{S_\phi} \propto 1/\sqrt{f}$$

which is observed in the absence as well as in the presence of an Au:Er sensor [Dan05]. This behavior is shown in the left diagram in fig. 2.11.
The presence of an Au:Er sensor however, lifts not only the white noise level but also the 1/f contribution. The increase of white flux noise can be fully understood by the magnetic Johnson noise, that is caused by the thermal motion of the conduction electrons in the sensor. On the contrary, the increase of the $1/f$ component is not fully understood. As can be seen from fig. 2.11 (left side), the noise amplitude increases with the number of sensors that are placed in the two circular loops of the gradiometric SQUID. In similar measurements [Dan05], the Er concentration of the sensor material was varied and it was found that this noise contribution increased with increasing number of Er-ions, which suggests that this flux noise is generated by fluctuating magnetic moments in the sensor. A thermally driven $1/f$-component can be explained by interaction mechanisms among spins, but the $1/f$-noise contribution discussed here shows almost no temperature dependence from 4.2 K down to 30 mK, as can be seen in the right diagram in fig. 2.11. So far no explanation has been found for this behavior. For interactions among spins in spin glasses this kind of frequency dependence would be not unusual but the transition of Au:Er into a spin glass state occurs at much lower temperatures ($\sim$ 1mK, see fig. 2.3). An explanation might be given by the interaction among the erbium spins and the nuclear quadrupole moments of the gold matrix. Additional experiments have to test this assumption. One possibility would be to use different host materials for the erbium ions. Especially

interesting is the host material silver because it has a nuclear spin $I = 1/2$ and no quadrupole moment.

$1/f^2$ Noise

In former MMC detectors based on gradiometric SQUIDs with circular loops and cylindrical Au:Er sensors an additional noise contribution has been observed [Sch00, Lin07]which has a frequency dependence of

$$\sqrt{S_\phi} \propto 1/f \ .$$

This behavior dominates the noise level at low temperatures ($T < 50$mK), where the MMC is a very sensitive thermometer. The upper curve in fig 2.12 is the noise

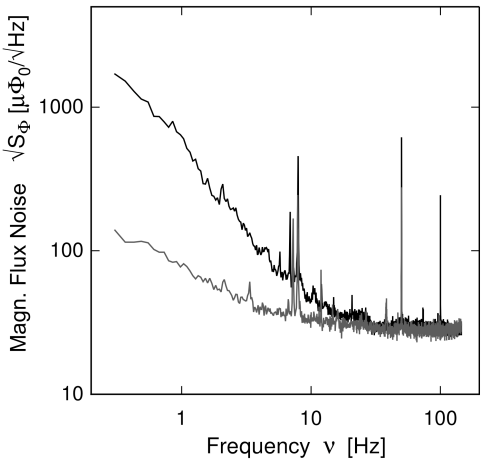

Figure 2.12 Comparison of the noise measurement of a gradiometric detector setup in which one pick up loop is equipped with a sensor (upper curve) and with both pick up loops equipped (lower curve). At low frequencies $\sqrt{S_\phi} \propto 1/f$. For higher frequencies $\sqrt{S_\phi} \propto 1/f^2$ before it levels off into the white noise plateau.

measurement for a setup in which one pickup loop of the gradiometric SQUID is equipped with sensor and absorber. For low frequencies, up to 50 Hz, the spectral power densities for the noise shows the $1/f^2$ dependency. For high frequencies the white noise level determined by a comparably high white noise level of the SQUID electronics is observed. The lower curve represents the noise of the same SQUID setup but with both loops equipped with an Au:Er sensor (900 ppm). The $1/f^2$ behavior is strongly reduced and just the $1/f$ component is observable. Since the noise does decrease with an increasing number of spins in the SQUID loop, this $1/f^2$ noise is not due to a material property of the Au:Er sensor. It seems likely that this contribution is effectuated by temperature fluctuations in the sensor or between the chip and the sensor. One possible origin for these temperature fluctuations could be a fluctuating power dissipation in the shunt resistors of the SQUID. Consequently the temperature of the sensor fluctuates which will lead to a fluctuating magnetization and therefore flux noise.

2.3.2 Energy Fluctuations

The Detector as a Canonical Ensemble

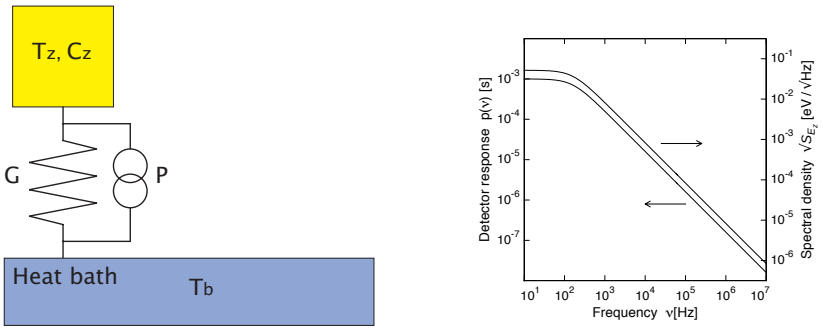

Figure 2.13 Canonical ensemble consisting of one subsystem which is connected to a heat bath. In the diagram the left ordinate gives the detector response on an incident x-ray as a function of frequency. For comparison, the right ordinate shows the noise due to energy fluctuations between subsystem and heat bath.

In statistical physics a canonical ensemble describes a system in thermal equilibrium with a heat bath at a fixed temperature. Therefore, the system is not closed and the energy content fluctuates. Let us assume, the detector consists of an absorber at a temperature T with the heat capacity C connected to a heat bath with temperature T_b like it is pictured in fig. 2.13. The energy of this system fluctuates around an average value with the standard deviation

$$\triangle E_\mathrm{rms} = \sqrt{k_\mathrm{B} C T_\mathrm{b}^2} \tag{2.13}$$

Since the coupling to the heat bath has a finite thermal conductivity G, energy fluctuates between the system and the bath with a characteristic time constant $\tau = C/G$. In our model, the fluctuations are represented by a noise source P parallel to the thermal coupling. Similar to the thermal Johnson noise exhibited by resistors, the spectral density of the power fluctuations through the thermal link connecting the absorber and the heat bath can be given by

$$S_\mathrm{P} = 4 k_\mathrm{B} T^2 G \ . \tag{2.14}$$

The differential equation describing the heat flow between the absorber system and the bath due to the temperature difference $T = T_\mathrm{b} - T_\mathrm{z}$ can be written as

$$C\dot{T}(t) = -T(t) \cdot G + P(t) \tag{2.15}$$

To solve the differential equation we consider one frequency component of the power fluctuation with frequency ω and phase φ

$$P(t) = \tilde{P} \exp(i\omega t + \varphi) \ . \tag{2.16}$$

For the amplitude of the temperature variations at this temperature we find

$$C_z\tilde{T} = \frac{\tau}{1+i\omega\tau}\tilde{P} \ . \tag{2.17}$$

Using $S_\mathrm{P} = \tilde{P}_\mathrm{rms} \cdot \triangle f$ to switch back to the spectral density of power fluctuations through the thermal link, we find for the fluctuations of the energy content

$$\tilde{E}^2_\mathrm{rms} = \frac{\tau^2}{1+(2\pi f\tau)^2} S_\mathrm{P} \triangle f \ . \tag{2.18}$$

Rewritten as spectral power density of energy fluctuations this reads

$$S_\mathrm{E}(f) = \frac{4\tau}{1+(2\pi f\tau)^2} k_\mathrm{B} C T^2 \ , \tag{2.19}$$

where we used the definition of S_P from equation 2.14. In the diagram in fig. 2.13 the spectral density (right ordinate) is shown as a function of frequency. It is frequency independent until a cut off frequency $f_1 = G/(2\pi C)$. For $f \ll f_1$ the level of the plateau is given by $(k_\mathrm{B} C_\mathrm{z} T^2 4\tau)^{1/2}$ and for $f > f_1$ the spectral density decreases proportional to $1/f^2$. An increasing heat capacity C leads thus to a rising plateau while the cut off frequency becomes smaller. A better thermal conductance G on the other hand leads to a lower plateau and an increasing cut off frequency. The integration of equation 2.19, $\int_0^\infty S_\mathrm{E}(f)df$ gives the standard deviation $\triangle E_\mathrm{rms}$ of a canonical ensemble (2.13).

If energy of an incident x-ray is absorbed the energy content of the detector rises instantaneously by $\triangle E = E_\gamma$ and then relaxes exponentially with the time constant τ to its original value

$$\triangle E = E_\gamma \exp(-t/\tau) \ . \tag{2.20}$$

To compare the frequency spectrum of this signal to the one of the energy fluctuations, equation 2.20 can be transformed into frequency space by a continuos Fourier-transformation. The result is given by

$$|\tilde{E}(f)| = E_\gamma \frac{2\tau}{1+(2\pi f\tau)^2} \tag{2.21}$$

and shown in fig 2.13 (left ordinate). The comparison of the function for the signal and for the noise is given by the Signal-to-Noise-Ratio (SNR)

$$\mathrm{SNR}(f) \propto \frac{\tilde{E}(f)\triangle f}{\sqrt{S_\mathrm{E}\triangle f}} \ . \tag{2.22}$$

In this simple model of the detector this ratio is constant throughout the whole frequency range. The consequence can be demonstrated as follows: if the frequency interval $[0, \infty]$ is divided into narrow frequency bands $\triangle f$, a measurement of the energy of an incident x-ray can be carried out independently in each of these frequency bands. Furthermore, the uncertainty $\triangle E([f_i, f_i + \triangle f])$ is the same for all the

frequency bands due to the constant SNR. For an average of N measurements, the uncertainty of the averaged energy measurements decreases with $1/\sqrt{N}$. Therefore the resolving power $E/\triangle E$ increases with $N\triangle f$ and is theoretically not limited in this model.

This unrealistic result is due to the absence of a broad band noise floor at high frequencies that limits the frequency band in which the SNR is high to a finite width leading to a finite resolving power. The most fundamental process that introduces this kind of high frequency noise floor in MMC detectors is discussed in the next section.

A Detector Model with Two Discrete Subsystems

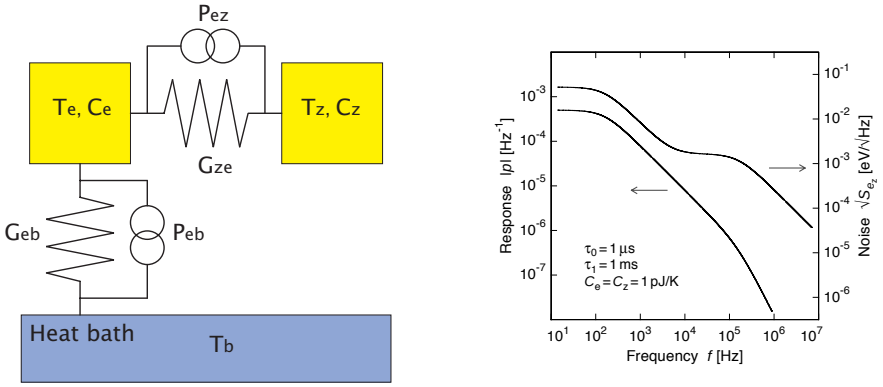

Figure 2.14 In this detector model two subsystems are considered, spins and conduction electrons. They are connected to each other and to the heat bath. As in fig. 2.13 the behavior of detector response and noise due to energy fluctuations is presented in the diagram and explained in the text. The signal to noise ratio is frequency dependent for frequencies higher f_{eff}. This limits the energy resolution to a finite value.

A model that describes the detector as a composition of two systems is pictured in fig. 2.14. The Zeeman system of the magnetic moments at a temperature T_{z} with a heat capacity C_{z} is thermally connected to the system of conduction electrons at a temperature T_{e} with a heat capacity of C_{e}. Both systems are coupled to a heat bath with the temperature T_{b}. The couplings between these systems are given by the thermal conductance G_{ze} and G_{eb}, respectively. P_{ze} and P_{eb} are noise sources which represent the power fluctuations through the thermal links. Analogous to the last section the spectral density of these powers can be written as

$$S_{\mathrm{Pze}} = 4k_{\mathrm{B}}T^2G_{\mathrm{ze}} \tag{2.23}$$

$$S_{\mathrm{Peb}} = 4k_{\mathrm{B}}T^2G_{\mathrm{eb}} \tag{2.24}$$

The heat flow can now be described by a system of coupled differential equations given by

$$C_{\mathrm{z}}\dot{T}_{\mathrm{z}}(t) = -(T_{\mathrm{z}}-T_{\mathrm{e}})G_{\mathrm{ze}} + P_{\mathrm{ze}}(t) \tag{2.25}$$

$$C_{\mathrm{e}}\dot{T}_{\mathrm{e}}(t) = -(T_{\mathrm{e}}-T_{\mathrm{z}})G_{\mathrm{ze}} - (T_{\mathrm{e}}-T_{\mathrm{b}})G_{\mathrm{eb}} - P_{\mathrm{ze}}(t) - P_{\mathrm{eb}}(t) + \dot{Q}(t) \tag{2.26}$$

Here $\dot{Q}(t)$ denotes the energy absorption due to an incident x-ray which is kept zero for the discussion of the energy fluctuations. In a more complex calculation similar to section 2.3.2, the spectral power density S_{Ez} of the fluctuating energy content of the spin system can be deduced

$$S_{\mathrm{Ez}} = k_{\mathrm{B}} C_{\mathrm{z}} T^2 \left(\alpha_0 \frac{4\tau_0}{1+(2\pi f \tau_0)^2} + \alpha_1 \frac{4\tau_1}{1+(2\pi f \tau_1)^2} \right) \quad . \tag{2.27}$$

The characteristic time constants τ_0 and τ_1 can be entirely expressed as a function of the thermal conductivities G_{ze} and G_{eb} and the heat capacities C_{z} and C_{e}. The dimensionless factors α_0 and α_1 are expressions of C_{z}, C_{e}, τ_0 and τ_1. For the relevant case of $\tau_0 \ll \tau_1$ and $0.1C_{\mathrm{e}} < C_{\mathrm{z}} < 10C_{\mathrm{e}}$, the approximation

$$\alpha_0 \approx 1-\beta \tag{2.28}$$

$$\alpha_1 \approx \beta \tag{2.29}$$

holds, where $\beta = C_z/(C_e + C_z)$. In the diagram in fig. 2.14 (right ordinate) the function $\sqrt{S_{\mathrm{Ez}}}$ is displayed for a detector operated at $T_{\mathrm{b}} = 50mK$, where the sensor heat capacity is $C_{\mathrm{S}} = 2\mathrm{pJ/K}$, the absorber heat capacity $C_{\mathrm{e}} = 1\mathrm{pJ/K}$, $\tau_0 = 1\mu\mathrm{s}$ and $\tau_1 = 1\mathrm{ms}$. At low frequencies the function is frequency independent until it reaches a cut off frequency like it was already the case in equation 2.19. The plateau at low frequencies is given by $(4k_{\mathrm{B}}C_{\mathrm{z}}T^2\tau_1\beta)^{1/2}$ with the cut off frequency $f_1 = 1/(2\pi\tau_1)$. For higher frequencies, $\sqrt{S_{\mathrm{E}}}$ drops proportional to $1/f$ before it levels off into a second plateau given by $(4k_{\mathrm{B}}C_{\mathrm{z}}T^2\tau_0(1-\beta))^{1/2}$. For frequencies higher than a second cut off frequency $f_0 = 1/(2\pi\tau_0)$ the spectral density decreases further with $1/f$.

Left to discuss is the response of the detector on the absorption of an incident x-ray illustrated in diagram 2.14 (left ordinate). This behavior can be deduced by solving the differential equations 2.25 and 2.26 if the noise sources P_{ze} and P_{eb} are disregarded and an external energy input $\dot{Q}(t) \neq 0$ is considered. In the following the assumption is made that the electron system thermalizes instantaneously upon energy absorption and thus only the time evolution of the spin system has to be regarded. In [Fle05] this approximation was shown to be justified. The energy input is assumed to be proportional to a delta function

$$\dot{Q}(t) = E_\gamma \delta(t) \quad . \tag{2.30}$$

As was already mentioned before, the energy E_z(t) of the Zeeman system can be monitored accurately with a SQUID magnetometer since the energy is proportional to the flux in the magnetometer loop. The energy of the spin system

$$E_{\mathrm{z}}(t) = E_\gamma p(t) = E_{\mathrm{z}}(e^{-t/\tau_1} - e^{-t/\tau_0}) \quad , \tag{2.31}$$

rises with a time constant τ_0, reaches a maximum and then relaxes with a longer time constant τ_1 to its original value. The undisturbed response of the detector as a function of time is given by $E_\gamma p(t)$. The Fourier transform of $p(t)$ gives the response

function in the frequency domain

$$|\tilde{p}(f)| = \frac{2\tau_1\beta}{\sqrt{1+(2\pi f\tau_0)^2}\sqrt{1+(2\pi f\tau_1)^2}} \tag{2.32}$$

For reasons of simplicity, again the relevant case where $\tau_0 \ll \tau_1$ was chosen. Clearly to see in diagram 2.14, the response functions $|\tilde{p}(f)|$ and the spectral power density of the energy fluctuations $\sqrt{S_{\mathrm{Ez}}(t)}$ do not have the same frequency dependence any more as it was the case in diagram 2.13. At small frequencies the response function is constant until the frequency $f_1 = 1/(2\pi\tau_1)$ for higher frequencies it decreases proportional to $1/f$. The response function does not level into a second plateau but decreases further proportional to $1/f^2$ for frequencies higher than a second cut off frequency $f_0 = 1/(2\pi\tau_0)$.

The signal-to-noise ratio is now frequency dependent and drops proportional to $1/f$ for frequencies higher than the frequency f_{eff} where the spectral density $\sqrt{S_{Ez}}$ levels into the second plateau. This effectively usable bandwidth, where the SNR is high, can be given by

$$f_{\mathrm{eff}} = \frac{1}{2\pi C_{\mathrm{z}}}\sqrt{G_{\mathrm{eb}}G_{\mathrm{ze}}(1+\frac{G_{\mathrm{eb}}}{G_{\mathrm{ze}}})} \tag{2.33}$$

Energy Resolution of a Metallic Magnetic Calorimeter

Assuming that an algorithm based on the so called optimal filtering technique is used to derive the energy of each absorbed x-ray quantum from the corresponding noisy pulse, the expected instrumental line width can be calculated from the signal-to-noise ratio $SNR = |\tilde{p}|/S_{\mathrm{Ez}}$ by

$$\triangle E_{rms} = \left(\int_0^\infty \mathrm{SNR}^2(f)df\right)^{-1/2} . \tag{2.34}$$

Using equation 2.27 and 2.32 we find the exact result

$$\triangle E_{rms} = \sqrt{4k_{\mathrm{B}}T^2C_{\mathrm{e}}}\left(\frac{G_{\mathrm{eb}}}{G_{\mathrm{ze}}}+\frac{G_{\mathrm{eb}}^2}{G_{\mathrm{ze}}^2}\right)^{1/4} . \tag{2.35}$$

Here the signal to noise ratio is already expressed as a function of the characteristic parameters of the given detector setup. The energy resolution has a finite value which is proportional to the energy fluctuations of a canonical ensemble $\sqrt{4k_{\mathrm{B}}T^2C_{\mathrm{e}}}$ and the ratio $(G_{\mathrm{eb}}/G_{\mathrm{ze}})^{1/4}$. So far the detector signals have always been expressed as a function of the time constants τ_0, τ_1 and the heat capacities C_{e} and C_{z}. With the approximation already used in section 2.14, $\tau_0 \ll \tau_1$, equation 2.34 can be written as

$$\triangle E_{\mathrm{FWHM}} \approx 2.35\sqrt{4k_{\mathrm{B}}T^2C_{\mathrm{e}}}\left(\frac{1}{\beta(1-\beta)}\frac{\tau_0}{\tau_1}\right)^{1/4} \tag{2.36}$$

The factor of 2.35 regards the conversion from standard deviation to the Full Width at Half Maximum (FWHM) of the energy distribution of the measurement, assuming this distribution to be gaussian.

In summary, the last sections showed that even if we ignore noise contributions of the read out circuit, the energy resolution of a MMC detector is fundamentally limited by the energy fluctuations among the thermodynamic subsystems of the detector. The best possible energy resolution is achieved in the case $C_e = C_z$ ($\beta = 0.5$), when equation 2.37 shows a minimum with

$$\triangle E_{\mathrm{FWHM}} \approx 2.35\sqrt{4k_{\mathrm{B}}T^2C_{\mathrm{e}}}\sqrt{2}\left(\frac{\tau_0}{\tau_1}\right)^{1/4} . \tag{2.37}$$

In an optimized detector setup, the heat capacities of the subsystems should thus be equal. Further reduction of the energy resolution can be achieved when the rise time τ_1 is short and and the decay time τ_0 is long. The x-ray detectors discussed in this thesis are operated at $T = 50\mathrm{mK}$ and have absorbers with dimensions $240\mathrm{x}240\mathrm{x}5\mu\mathrm{m}^3$ made out of gold. This corresponds to a heat capacity of $C_{\mathrm{e}} \simeq C_{\mathrm{abs}} = 1\mathrm{pJ/K}$. Assuming a rise time of $\tau_0 = 1\mu\mathrm{s}$ we find that the energy resolution of these detectors will be limited to $\triangle E \geq 1.4\mathrm{eV}$.

3. Experimental Techniques

3.1 Adiabatic Demagnetization Refrigerator

In this work an Adiabatic (Electron spin-) Demagnetization Refrigerator (ADR) was used to cool the MMC detector to working temperatures below 100mK. Cooling is achieved by using the magnetic field dependency of the spin entropy of paramagnetic salt pills.

Figure 3.1 shows a schematic cut view of the ADR cryostat used in the experiments discussed hereafter. The cold parts of the cryostat are contained in a vacuum vessel that provides the necessary thermal insulation. A liquid nitrogen bath cools a shield that reduces infrared radiation onto the enclosed parts. The helium bath cools a platform which supports the superconducting magnet coil that is immersed in liquid helium, as well as the two paramagnetic salt pills located in the bore of the magnet in the evacuated volume of the cryostat. The material of the pills, Fer-

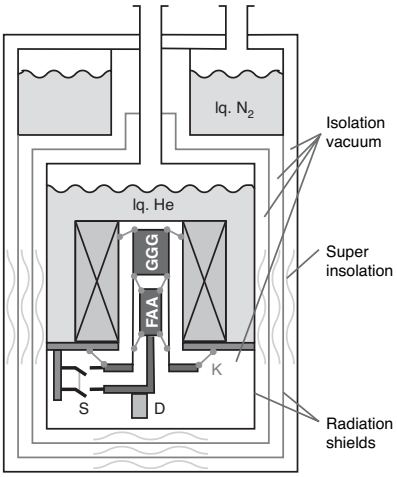

Figure 3.1 Schematic cut view of an ADR cryostat. Evacuated volumes thermally isolate colder from warmer parts. The paramagnetic salt pills (FAA, GGG) are located inside the magnet and are attached to the 4 K bath with kevlar strings (K). They are connected with the experimental platform D. For isothermal magnetization the pills can be contacted to the 4 K bath with a heat switch (S).

ric Ammonium Alum (FAA)[1] and Gadolinium Gallium Garnet (GGG)[2] is chosen in a way that the transition temperature to a magnetically ordered state lies in the milli-Kelvin range. The entropy $S(T, B)$ of the spin system is the dominating contribution to the total entropy. The GGG pill is kept in place by kevlar strings which are anchored at the 4 K stage. The kevlar strings supporting the FAA pill are tied to the GGG stage and thus these two pills have only a weak thermal contact to each other and to the 4 K bath. An annealed copper rod connects the FAA pill with the experimental platform. This platform can be thermally contacted to the 4 K bath by a mechanical heat switch. Experimental platform and heat switch are located in the isolation vacuum.

[1] $Fe_2(SO_4)_3(NH_4)_2SO_4 \cdot 24H_2O$
[2] $Gd_3Ga_5O_{12}$

The starting temperature of the magnetization/demagnetization cycle is determined by the temperature of the liquid helium bath. Under normal pressure, helium boils at a temperature of 4.2 K. Temperatures down to 1.5 K can be reached by pumping on the helium. At the beginning of the cycle the heat switch is closed to allow for a good thermal contact between the pills and the bath. In this situation the magnetic field is at $B = 0\mathrm{T}$ and the spins are randomly oriented. Therefore the entropy is at its maximum $S = Nk_\mathrm{B}\ln(2J+1)$, where N is the number of magnetic moments in the pills, k_B the Boltzmann constant and J the total angular momentum of the ions. In a first step the pills are magnetized. Applying an external field B causes a splitting of the energy levels according to the Zeeman effect. If the splitting between the Zeeman levels is larger than the thermal energy $g\mu_\mathrm{B}B > k_\mathrm{B}T$ the majority of spins occupies the states with lowest energy. The magnetizing is stopped at a field $B_\mathrm{i} = 6\mathrm{T}$ and once thermal equilibrium is reached, the temperature of the salt pills T_i equals the temperature of the bath, the magnetization is a maximum and the entropy $S(T_\mathrm{i}, B_\mathrm{i})$ is comparably small.

In this situation the pills are thermally isolated from the bath when the mechanical heat switch is opend. By demagnetizing slowly, the spin system is kept in thermal equilibrium with the phonon system, hence this process is adiabatic. The Zeeman splitting is continuously getting smaller allowing the (re-)population of higher energy levels. By scattering processes of spins with phonons, energy is transfered from the lattice to the spins resulting in a rising entropy of the spins and effective cooling of the phonon system.

Under the assumption of having a system of non-interacting magnetic moments in which their contribution to the heat capacity dominates, an estimate of the reachable temperatures can be given. Due to these assumptions, the entropy of the spin system does not change while demagnetizing. Furthermore, the entropy is dependent on the ratio of the Zeeman splitting $g\mu_\mathrm{B}B$ and the thermal energy $k_\mathrm{B}T$. The entropy is conserved and at any magnetic field B_f, this can be expressed as $S(B_\mathrm{i}/T_\mathrm{i}) = S(B_\mathrm{f}/T_\mathrm{f})$. If this is rewritten as an expression for the reachable base temperature,

$$T_\mathrm{f} = \frac{B_\mathrm{f}}{B_\mathrm{i}} T_\mathrm{i} \ , \tag{3.1}$$

we see, that in principle, arbitrarily low temperatures can be reached by choosing B_f to be small. In reality the interaction between the spins in the paramagnetic material yields an effective inner magnetic field B_in which makes the reachable base temperature not only dependent on T_i, B_i and B_f but also on the inner magnetic field B_in.

Since this cooling technique is not continuous there is no more cooling power after a complete demagnetization and having reached the lowest temperature T_f. Depending on the parasitic heat input $\dot{Q}$ and the total heat capacity C, the system will warm up according to $\dot{T} = \dot{Q}/C$. To reduce the heat load $\dot{Q}$ during demagnetization and at the lowest temperatures the pills are only connected to the bath by kevlar strings which have a low thermal conductivity. Additionally a system of two paramagnetic salt pills is chosen. The FAA pill reaches temperatures down to

$T_{\mathrm{FAA}} = 22\,\mathrm{mK}$, while the final temperature of the GGG pill is $T_{\mathrm{GGG}} = 250\,\mathrm{mK}$. The higher temperatures of the GGG pill is due to the larger concentration of spins in this material and therefore a higher internal magnetic field. On the other hand the heat capacity of the GGG pill in this situation is much larger therefore acting as a heat sink for all electrical wires going to the experiment mounted on the FAA pill. After having reached the base temperature of 22 mK the FAA salt pill warms up with a typical rate of 0.1 mK/h which corresponds to a parasitic heat input for this cryostat of $\dot{Q} \approx 25\mathrm{nW}$.

3.2 Superconducting Magnetometers – dc-SQUIDs

Presently, SQUIDs[3] are the most sensitive magnetometers and therefore the ideal readout devices for MMC detectors. They exploit the interference of the macroscopic wave function in a superconductor. As a consequence of the macroscopic nature of the wave function, the flux ϕ inside an uninterrupted superconducting loop is conserved. The smallest entity of a flux change $\delta\phi$ in a superconducting ring is given by one flux quantum $\phi_0 = 2.07 \cdot 10^{-15}\,Vs$ [Lon50]. If a superconducting loop is interrupted and if this interruption is only small enough, it represents a weak link for the Cooper pairs which may tunnel through them and thus carry a current dissipationless across an insulating barrier [Jos62].

3.2.1 The dc-SQUID

Figure 3.2 a) shows a sketch drawing of a dc-SQUID[4]. Such a device consists of a superconducting loop with two Josephson junctions, indicated by crosses, connected in parallel. These junctions are commonly made out of insulating metal-oxide layers about 10 Å thick. Shunt resistors R_{s} are connected in parallel to each junction. With-

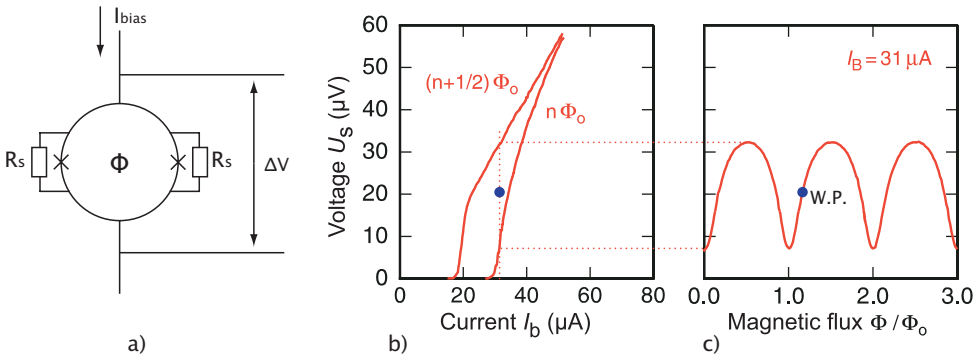

Figure 3.2 dc-SQUID with shunt resistors R_{s} a) and its I-V characteristic b). Such a device is a flux-to-voltage transformer c). The working point is indicated by W.P.

[3] SQUID is the abbreviation for **S**uperconducting **QU**antum **I**nterference **D**evice
[4] For a detailed review about SQUIDs please refer to [CAB03].

out these resistors SQUIDs show hysteretic behavior with increasing and decreasing flux ϕ inside the SQUID loop. dc-SQUIDs are biased with a fixed current I_b which is carried dissipationless by Cooper pairs until a critical current I_c is reached. For currents $I_b > I_c$ a voltage drop across the junctions occurs. Due to the interference of the wave function at the junctions, the critical current depends not only on temperature and the geometry of the junction but has also a periodic dependency on the flux inside the SQUID loop. The I-V characteristic is pictured in fig. 3.2 b) for the cases where the flux inside the SQUID loop is $\phi = (n + 1/2)\phi_0$ and $\phi = n\phi_0$, where n is an integer. The sharp rise can be described by a dynamic resistance $R_{dyn} = \partial U/\partial I_b$. At higher bias currents the characteristic is that of an ohmic behavior determined by the shunt resistors. If the SQUID is biased with a current slightly higher than the highest critical current, the voltage drop across the SQUID depends periodically on the magnetic flux within the SQUID loop. One period of the V-ϕ characteristic, depicted in fig. 3.2 c), equals one ϕ_0. When operated on a steep slope of the V-ϕ characteristic, with a high flux-to-voltage transfer coefficient

$$V_\phi = (\partial V/\partial \phi) \ , \tag{3.2}$$

the SQUID produces an output voltage as a response to a small flux change $\delta\phi \ll \phi_0$. Therefore, a SQUID is effectively a very sensitive flux-to-voltage transformer.

3.2.2 Single Stage SQUID Readout

Without additional circuitry the response of the SQUID is highly nonlinear. The regime where the output voltage of the SQUID depends linearly on the change of flux is only about 25% of one flux quantum. To gain linear flux range, a regulation scheme is applied where any flux signal is compensated by a negative feedback flux, produced by a so called Flux-Locked-Loop (FLL) circuit. This way the working point on the V_{SQ}-ϕ characteristic can be kept steady at the chosen voltage output level V_{wp} of the SQUID.

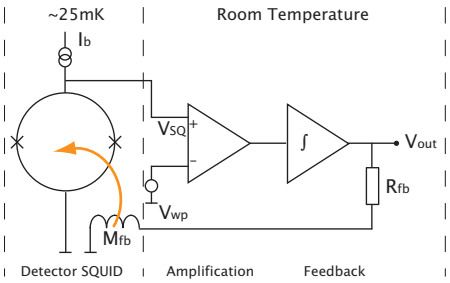

Figure 3.3 Single stage SQUID setup with Flux-Locked-Loop circuit.

In fig. 3.3 a single stage setup is shown where the FLL circuit is implemented. In this setup the SQUID drawn on the left is used to read out the detector. Amplification and SQUID readout is done at room temperature. Any change of flux $\delta\phi$ in the SQUID generates a change of the voltage V_{SQ} across the SQUID. The difference to the voltage level at the working point V_{wp} is then amplified. An integrator is used to generate a current $-I_{fb} \propto \delta\phi$ which is sent through a feedback coil close to the

SQUID. This way the flux $-\phi_{\mathrm{fb}} = M_{\mathrm{fb}} \cdot I_{\mathrm{fb}}$ is inductively coupled into the SQUID compensating the initial flux $\delta\phi$, where M_{fb} is the mutual inductance between the feedback coil and the SQUID loop. The voltage drop across the feedback resistance $V_{\mathrm{out}} = R_{\mathrm{fb}} \cdot I_{\mathrm{fb}} = R_{\mathrm{fb}} \cdot \delta\phi / M_{\mathrm{fb}}$ is proportional to the initial flux change $\delta\phi$ and is used as output signal.

3.2.3 dc-SQUID Noise

Although SQUIDs are superconducting devices, they still exhibit an intrinsic noise level. Naively, only thermal Johnson-Noise $\sqrt{S_{\mathrm{I}}} = \sqrt{4k_{\mathrm{B}}T/2R}$ from the shunt resistors contributes. Due to the self inductance L_{s} of the SQUID loop this results in a flux noise of $\sqrt{S_{\phi_1}} = L_{\mathrm{s}}\sqrt{2k_{\mathrm{B}}T/R}$. For a complete understanding of all noise contributions the evolution of the phase difference across the Josephson junctions as well as the influence of the parasitic junction capacitance have to be considered. A numerical simulation and optimization for the intrinsic flux noise level was done by Tesche and Clarke [Tes77] regarding all these contributions with the result for the flux noise density of optimized SQUIDs given by

$$\sqrt{S_{\phi_1}} = \frac{1}{V_\phi}\sqrt{S_{\mathrm{U,SQUID}}} \simeq L_{\mathrm{s}}\sqrt{16k_{\mathrm{B}}T/R} \ , \tag{3.3}$$

which is about a factor $\sqrt{8}$ larger than the result of the simple approach. $\sqrt{S_{\mathrm{U}}}$ is the total voltage noise as it is measured which is converted into flux noise by multiplying it with the inverse flux-to-voltage transfer coefficient $1/V_\phi$. If typical values for the self inductance of the SQUID loop $L_{\mathrm{s}} = 200\,\mathrm{pH}$ and the shunt resistors $R_{\mathrm{s}} = 4\,\Omega$ are inserted, the flux noise at 50 mK is $\sqrt{S_{\phi_1}} = 0.16\,\mu\Phi_0/\sqrt{\mathrm{Hz}}$.

This expected noise level is very low due to the assumed operation at very low temperature. In many experiments the flux noise is found to be much higher. On the one hand, the finite power dissipation and the weak electron phonon coupling in the shunt resistors lead to a minimal electron temperature of typically 300 mK. On the other hand, parasitic resonances close to the Josephson frequency might prevent the SQUID from being operated under optimal conditions.

Another noise source which adds to the total noise, is contributed by the room temperature read out electronics. In this work a Flux-Locked-Loop electronics designed by the PTB in Berlin[5] was used. It has a very low input voltage noise of $\sqrt{S_{\mathrm{U,el}}} \approx 0.33\mathrm{nV}/\sqrt{\mathrm{Hz}}$ [DH05]. Therefore, the apparent flux noise $\sqrt{S_\phi}$ of a single stage SQUID has the following contributions

$$\sqrt{S_\phi} = \sqrt{S_{\phi_1}} + \frac{1}{V_\phi}\sqrt{S_{\mathrm{U,el}}} \ . \tag{3.4}$$

With a typical value for the flux-to-voltage transfer coefficient of $V_\phi = 200\,\mu\mathrm{V}/\phi_0$ the contribution of the electronics is $\sqrt{S_{\mathrm{U,el}}}/V_\phi = 1.65\,\mu\Phi_0/\sqrt{\mathrm{Hz}}$. Compared to the intrinsic flux noise this value dominates the noise level of a single stage SQUID setup in the case of operational temperatures below 1 K. A natural way to reduce the noise

[5] XXF-1 commercialized by Magnicon, Hamburg, Germany; http://www.magnicon.de/

contribution of the electronics is to amplify already at low temperatures. For this work a two stage SQUID setup was designed, where the detector-SQUID output is amplified at low temperatures by using a secondary SQUID as an amplifier.

3.2.4 Two Stage SQUID Readout

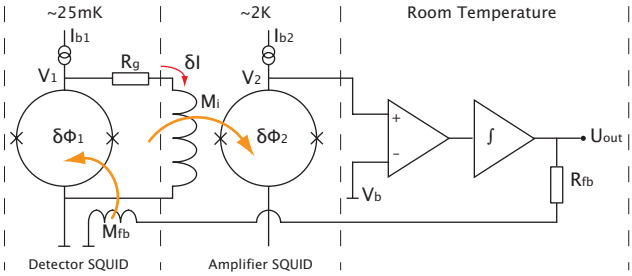

Figure 3.4 Two stage SQUID setup with Flux-Locked-Loop circuit.

In fig. 3.4 a readout scheme is shown where the primary SQUID, used to read out the detector, is followed by a secondary SQUID serving as a current sensor. It amplifies the signal from the detector SQUID and is part of the FLL circuit similar to the one described in 3.2.2. Both SQUIDs are operated with a bias current I_{b1} and I_{b2}, respectively. The input coil of the amplifier SQUID and the resistor R_g are in parallel to the primary SQUID, therefore one part of the bias current I_{b1} of the primary SQUID is flowing through the input coil of the secondary SQUID. Due to a change of flux in the primary SQUID the voltage drop across the SQUID changes. This causes a change of current δI through the input coil of the secondary SQUID which leads to a change of flux $\delta\phi_2 = M_i \cdot \delta I$, where M_i is the mutual inductance between the input coil and the secondary SQUID. For the measurements in this work a SQUID array [6] with a value for the input coupling of $1/M_i = 23\mu A/\phi_0$ was used as secondary SQUID.

An important property of a two stage setup is the ratio

$$G_\phi = \frac{\partial\phi_2}{\partial\phi_1} = M_i \left(\frac{\partial I}{\partial\phi_1}\right)_{R_g, I_b} \tag{3.5}$$

between flux change in the secondary SQUID $\delta\phi_2$ and flux change in the primary SQUID $\delta\phi_1$. It gives the flux-to-flux amplification at the working point and by influencing the shape of the V-ϕ characteristic it has an impact on the performance of this two stage setup.

By looking at the dependence $\phi_2(\phi_1)$ and then $V_2(\phi_2)$ shown in fig. 3.5, the shape of the V_2-ϕ_1 characteristics of the two stage SQUID can be understood. A flux-to-flux amplification of $G_\phi > 1$ usually leads to a characteristics with a double dip as indicated in fig. 3.5 for the blue line marked with circles ($G = 1.2$) and the pink line marked with squares ($G > 3$). In the last case ($G > 3$) the characteristic cuts zero twice during the interval of one ϕ_0 with the same sign of the slope. Both

[6] C3X16A, designed at the PTB Berlin

points represent possible working points but with two different absolute values of the slope. Since the slope and therefore the flux-to-voltage transfer coefficient is much

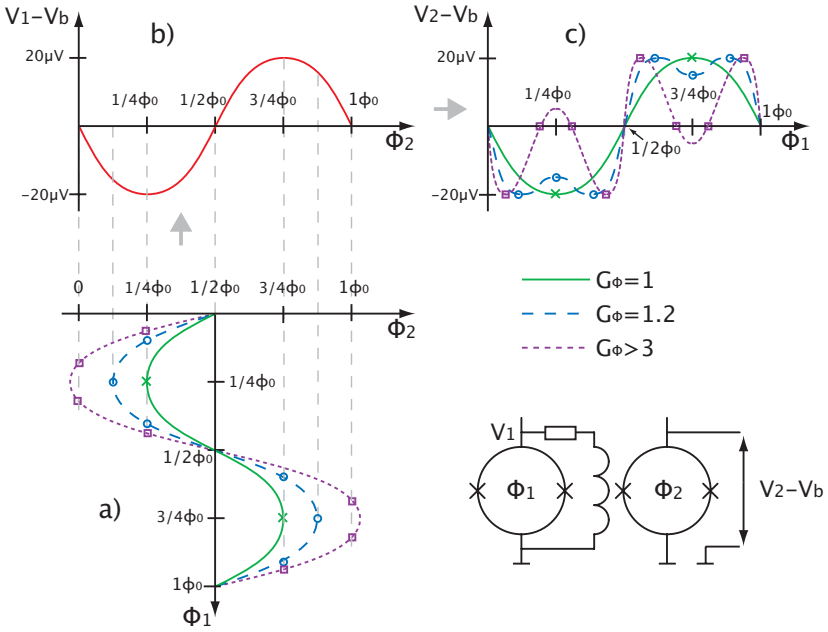

Figure 3.5 a) shows the output signal U_{out} of the secondary SQUID ϕ_2 oscillating between two maximal output voltages. b) shows ϕ_2 compared to the flux ϕ_1 in the primary SQUID for three different values for G_ϕ. c) is constructed out of these two graphs, showing U_{out} as a function of ϕ_1.

smaller at this additional working point the signal-to-noise ratio would be noticeably lower. On the other hand, the slope of the first working point becomes steeper with higher G_ϕ resulting in a higher flux-to-voltage transfer coefficient and thus a higher signal-to-noise ratio. Therefore a flux-to-flux amplification of $1 \leq G_\phi \leq 3$ is optimal which yields a steep slope and a double dip without any undesirable working points with a small slope. To influence the flux-to-flux amplification and the shape of the characteristics in a given setup with fixed input coupling M_i the value of the resistor R_g can be changed.

Fig. 3.6 a) shows the V_2-ϕ_2 characteristics of the amplifier SQUID and fig. 3.6 the V_2-ϕ_1 characteristics of the two stage setup as it was used in this work. The working points (wp) are indicated as well as the slope at these points: $\partial V_2/\partial\phi_2|_{wp} = 1.0\,\text{mV}/\phi_0$ for the amplifier SQUID characteristics and $\partial V_2/\partial\phi_1 = 930\,\mu\text{V}/\phi_0$ for the two stage SQUID setup. As mentioned before the input coupling of the amplifier is $1/M_\text{i} = 23\,\mu\text{A}/\phi_0$. This coupling is rather weak compared to the signal from the primary SQUID leading to no actual flux-to-flux amplification, but to $G_\phi = 0.9$. The two stage characteristics is therefore similar to that of the detector SQUID itself. In the experiment discussed here a small gain resistor of $R_\text{g} = 0.27\,\Omega$ was chosen to reduce the power dissipation on the chip. An explanation for this is given at the end of this section. The two stage characteristics is slightly asymmetric reflecting the asymmetric arrangement of the inductances of the primary SQUID which will be discussed in detail in section 3.12.

The apparent flux noise of the primary SQUID in a two stage setup is a composition of noise contributions from primary SQUID, secondary SQUID and electronics

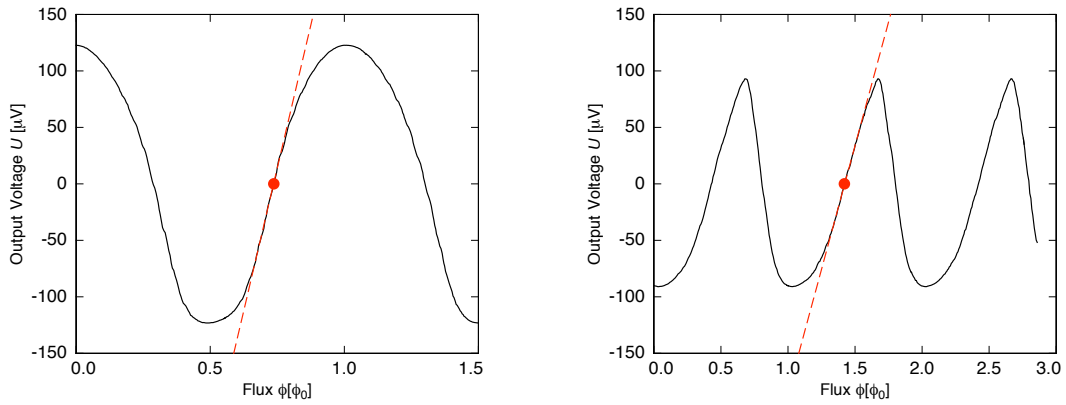

Figure 3.6 SQUID characteristics of the amplifier array and of the two stage setup.

given by

$$\sqrt{S_\phi} = \left(S_{\phi_1} + \frac{4k_\mathrm{B}TR_\mathrm{g}}{V_{\phi_1}^2} + \frac{S_{\phi_2}}{G_\phi^2} + \frac{S_\mathrm{U}}{V_{\phi_2}^2 G_\phi^2} \right)^{1/2} . \tag{3.6}$$

Besides the intrinsic flux noise level of the primary SQUID $\sqrt{S_{\phi_1}}$ an additional noise contribution is the Johnson-noise from the gain resistor given by $\sqrt{4k_\mathrm{B}TR_\mathrm{g}}/V_{\phi_1}$. Since this contribution decreases with temperature the gain resistance should be installed at the lowest temperature. The contributions by the secondary SQUID and the electronics in term three and four are reduced by the flux-to-flux amplification. With a typical flux-to-voltage transfer coefficient of $V_{\phi_2} = 1.0\mathrm{mV}/\phi_0$ and a flux-to-flux amplification of $G_\phi = 3$ at common working temperatures for the secondary SQUID of 2 K the noise contribution by the electronics is reduced to $\sqrt{S_\mathrm{U}}/(V_{\phi_2}G_\phi) \approx 0.3\,\mu\Phi_0/\sqrt{\mathrm{Hz}}$. This value is more than a factor of five smaller compared to the single stage setup given at the end of section 3.2.3. To summarize, the contribution of the read out electronics in a two stage setup can be reduced by increasing the flux-to-flux amplification and by using secondary SQUIDs or SQUID arrays as amplifiers which have a large V_{ϕ_2}.

A two stage SQUID read out has an additional advantage regarding the power dissipation on the silicon chip of the primary SQUID which leads to an unwanted increase in temperature in the paramagnetic sensor since, in the setup discussed here, the Au:Er sensor is placed directly on the SQUID chip. In fig. 3.7 a schematic I-V characteristics is drawn in a situation where in a) a single stage and in b) a two stage setup is operated at the optimal bias current I_b. In a two stage setup the readout of the primary SQUID can be done with low impedance, especially if the resistor R_g is chosen smaller than the dynamical resistance of the SQUID. The applied bias current I_b is split up between the primary SQUID and the branch containing the gain resistor and the input coil of the secondary SQUID. While changing the flux in the primary SQUID the current I_1 through the SQUID and the voltage drop V_1 across it will follow the dashed red line which has a slope of $-R_\mathrm{g}$. The smaller R_g is

chosen, the smaller is the voltage drop across the SQUID. Again the working point is marked with a dot and the power dissipation $P_1 = I_1 \cdot V_1$ is indicated by the shaded area. Comparing a) and b) the power dissipation in a two stage setup is smaller then in a single stage setup. Furthermore the change of current δI_1 per unit of flux change $\delta\phi_1$ (see equation 3.5) is maximized in the limit of small values for R_g. The power dissipation can thus be made very small without negative side effects regarding the noise.

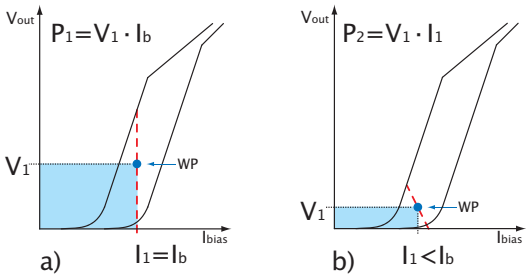

Figure 3.7 I-V characteristic with the voltage output level for a) a single stage setup and b) a two stage setup with a gain resistor. The slope of the dashed line in b) is given by $-R_g$. The power dissipation is marked by the shaded area.

3.2.5 Data Acquisition

The output signal of the SQUID electronics is split into two channels, one serving as a trigger which can be heavily filtered and the other being the signal from the detector which is filtered and recorded in a way that is adequate for the subsequent analysis. Both signals are passed through low noise amplifiers which provide the additional feature of a second order band-pass filter[7]. For the trigger-signal typically a low-pass filter of 30 kHz and a high-pass filter of 30 Hz is chosen in order to provide a steep edge to trigger on. Since this modifies the pulse shape, the acquisition of

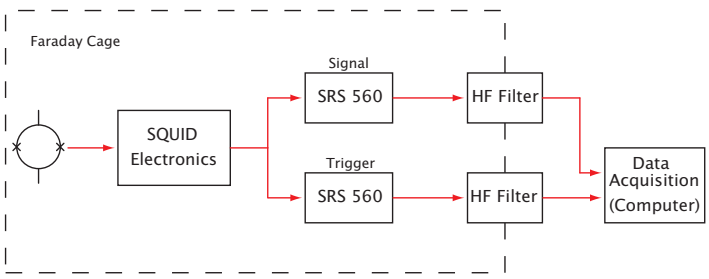

Figure 3.8 Block diagram of how signals from the read out electronics are processed and acquired

the detector signal for pulse shape analysis is done only with low-pass filter settings. The signals are fed through high frequency filters leading out of the faraday cage and are converted from analog to digital signals by a dual channel oscilloscope card[8]. The card allows for the definition of a trigger threshold to identify the transient signals. For each triggered signal 16384 voltage samples with 12 bit resolution are acquired, out of which 1/4 are prior to the trigger. Every third to tenth signal

[7] Type SRS-560, manufactured by Stanford Research, USA
[8] Compuscope SAC-8012A/PCI; GaGe, Montreal, Canada

the corresponding baseline is acquired which contains information about the noise contained in the signal and is therefore important for subsequent data analysis.

3.3 Readout Geometries

Magnetic calorimeters use the magnetization of a paramagnetic sensor in a weak magnetic field as a temperature information. A variety of different geometries are possible to read out the change of flux $\delta\phi$ caused in the magnetometer loop by an incident x-ray in the detector. A cylindrical sensor geometry and a circular magnetometer loop, as pictured in fig. 3.9, has been deployed (see chapter 2) to demonstrate the detection principle and the response of the detector upon energy absorption. The necessary external magnetic field is generated by a coil around the sensor. As the external field is homogeneous, the detector behavior is fairly easy to calculate. MMC detectors with this kind of geometry have been successively used for high resolution x-ray spectroscopy in the past. The best energy resolution achieved so far is $\triangle E = 2.7\text{eV}$ at x-ray energies up to 6keV [Lin07].

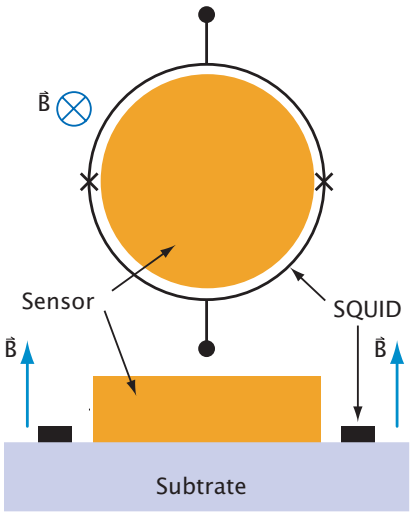

Figure 3.9 Cylindrical readout geometry in which the sensor is placed directly in the SQUID loop.

In picture a) of fig. 3.9 the sensor is directly placed in the circular loop of the SQUID. The coupling between spins in the sensor and in the loop is determined by the mutual geometry of SQUID loop and sensor. Since the magnetometer is operated with a certain bias current, power is dissipated directly on the detector chip. This direct heating of the sensor leads to a higher sensor temperature and thus to a reduced signal-to-noise ratio. When planing for a future application where more than a single detector is operated on one chip, magnetic- and thermal cross talk between the detectors have to be taken into account.

3.3.1 Meander Shaped Readout Geometry

A read out scheme which is quite different from the one just discussed, is based on a meander shaped pick up coil. This feature is very promising, all the more because it

allows for a large filling factor of the coil representing a good coupling between the magnetic moments in the sensor and the coil. We assume the meander shaped pick up coil to be made of a niobium thin film with a transition temperature of $T_c = 9.2\,\mathrm{K}$ on a silicon substrate which is microfabricated using standard photolithographic techniques.

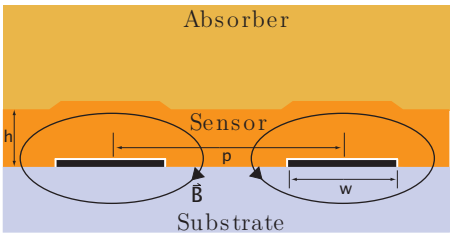

Figure 3.10 Cut view of a meander with sensor and absorber. The geometric parameters width, pitch and sensor height are labeled. To avoid electrical shorts a thin insulation layer (white) separates the meander from the sensor.

The geometry of the meander is defined by a few geometric parameters which will play an important role in the following discussion concerning the magnetic field distribution and the signal size of a meander type MMC detector. Figure 3.10 schematically shows one period of a meander chip as a cut view. Two meander stripes are pictured which have a width w and a pitch p. The stripes are about 500 nm thick. A thin insulation layer electrically separates the metallic sensor from the meander stripes.

In this type of detector geometry the meander serves as a pick up loop as well as to generate the magnetic field which alligns the spins in the sensor. Figure 3.10 already indicates that the magnetic field produced by a meander is inhomogeneous and a multipole field of high order which has the advantage that magnetic cross talk between detectors is diminished. The magnetic field distribution in the sensor volume and its vicinity is discussed in section 3.3.4. In section 3.3.5 the signal size which can be achieved with such a detector geometry is discussed.

As mentioned before, meander type read out schemes do not have an external coil to generate the magnetic field in the sensor. Instead, a persistent current I_0 is prepared in the meander which generates the magnetic field in the meandering pick up coil as described above. The preparation of a persistent current is explained in section 3.12.

Figure 3.11 shows a sketch of a dc-SQUID with a meander shaped SQUID inductance, that allows for the preparation of a large persistent current of up to about 100 mA in the meandering coils. It consists of two meander structures which are connected in parallel to each other and to the two Josephson junctions of the dc-SQUID. Each meander can be covered with a Au:Er temperature sensor. One of the meanders in combination with the Josephson junctions would be sufficient to form a dc-SQUID. However, the meander structure has to serve not only as a magnetometer loop but also as the coil to generate the magnetic field in which the magnetic moments in the sensor material are aligned. Only by adding a second superconducting loop in parallel a current can flow persistently without experiencing dissipation at the junctions. Taking the flux conservation in a superconducting ring and the Kirchhoff rules into account, the consequence of having two parallel loops is that the

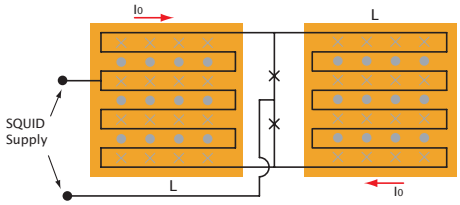

Figure 3.11 dc-SQUID with two meander shaped inductances which are connected in parallel to each other.

flux signal that is effectively seen by the SQUID is a factor of two smaller then a change of flux that occurs in one of the meanders. This loss in signal size is in part compensated since the inductance of the meanders in parallel to each other is only one half of the inductance of one meander. Therefore, the effective inductance of the SQUID is smaller which leads to a smaller achievable flux noise of the SQUID.

3.3.2 The MagCal 14/15

Recently, the design pictured in fig. 3.11 was realized in a cooperation with the IPHT Jena[9] and used throughout this work. A MagCal 14 chip is displayed in fig. 3.12 on

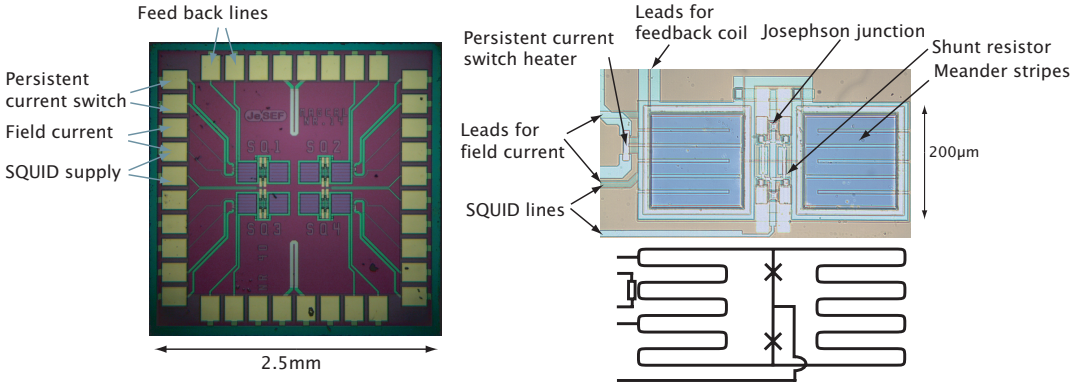

Figure 3.12 MagCal 14 chip with four Meander-integrated-SQUIDs in the center of the chip. The four neighboring meanders in the center, each belonging to a different SQUID, are 60μm apart. On the right, details of the meanders and SQUIDs are pictured (V.Zakosarenko, R.Stolz and H.G.Meyer, IPHT Jena).

the left. The four SQUIDs with meander shaped inductances in the center of the chip can be electrically contacted via bonding pads that are placed along the edges of the chip. The micrograph on the right side shows one of the SQUIDs in detail, as well as the corresponding circuit diagram. Two meandering loops are connected in parallel, each consisting of 8 meander stripes. The meander stripes have a width of $w = 20\,\mu$m and a hight of 400 nm covering a total area of $200 \times 200\,\mu\text{m}^2$. They are 5$\mu$m apart resulting in a pitch of $p = 25\,\mu$m and thus the ratio of width to pitch is $w/p = 0.8$. The flux-voltage characteristics for the SQUIDs, which was shown and discussed in section 3.4, shows a clear asymmetry. This behavior can be explained by the fact that one of the supply lines of the SQUID, the one that contacts the meander,

[9]Institut für Physikalische Hochtechnologie, Jena

is not connected to the center of the meander inductance. Therefore, a change of bias current through the SQUID, as it occurs in a two-stage configuration with small R_g while sweeping the flux in open loop, also causes additional flux in the SQUID, leading to the observed asymmetry. Two different types of SQUIDs have been used in this work – MagCal 14 and MagCal 15. The dimensions and materials of both SQUID designs are identical, but the type MagCal 15 has a 400 nm thick insulation layer made of SiO_x that covers the Nb-meander in order to prevent electrical shorts between the Au:Er sensor and the meander.

The persistent current switch heater as well as the supply lines for heater current and field current are indicated in the micrographs in fig. 3.12. The procedure to generate a persistent current, in other words freeze magnetic flux in the superconducting loop formed by the two meanders, is illustrated in the three steps shown in fig. 3.13.

i) The magnetic flux inside a superconducting ring is conserved. Initially, some magnetic flux ϕ_i is trapped inside the loop of the meanders. A field current I_a up to 150 mA is supplied to the meander which is in this situation still a superconducting ring. There are two possible paths for the current to flow and therefore it splits according to the inductances L_1 and L_2 conserving the magnetic flux ϕ_i.

ii) The persistent current switch heater is a microstructured layer of gold-palladium covering a small extension in one of the meander turns. It stays normal conducting while the meander is superconducting. With the field current applied, a current is applied to the resistor which locally heats the meander structure. The heating pulse has to be high enough to drive the niobium structure normal conducting in this small area. The applied field current flows now completely over the inductance L_1. In this situation the magnetic flux inside the loop of the meanders is $\phi = L_1 I_a$.

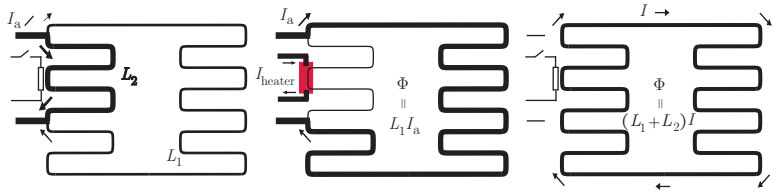

Figure 3.13 The procedure to freeze magnetic flux in the meandering loop is illustrated in three steps. The persistent current switch is represented by a resistor and an electrical switch. Each step is explained in the text.

iii) After the heat pulse, the meanders are again completely superconducting and the magnetic flux $\phi = L_1 \cdot I_a$, surrounded by the meanders, is conserved. After ramping down the current I_a from the external power supply, flux conservation is established by a persistent current

$$I = \frac{L_1}{L_1 + L_2} I_a \ , \tag{3.7}$$

flowing through both meanders, as indicated by fig. 3.13. Counting the number of meander stripes, which produce the inductance L_1 and the number of stripes of L_2,

the relation $L_1/L_2 \approx 1/3$ is found. Thus, the persistent current I_0 flowing through the meander structure is only 75% of the initially applied current I_a.

3.3.3 Wiring

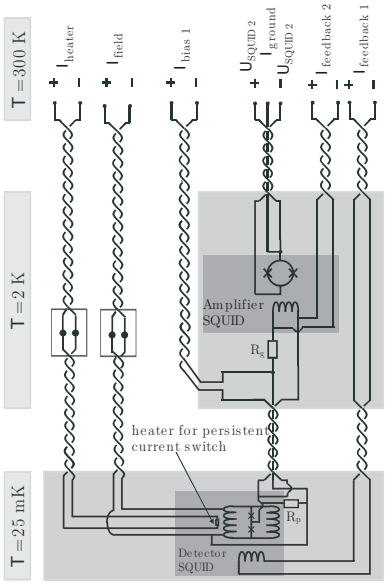

Figure 3.14 Complete wiring for a two stage SQUID setup used to read out an MMC detector

Twisted pairs and triples of copper wire are used between room temperature and 2 K, heat sunk at 77 K and 20 K. Between the 2 K-plate and the experimental platform at FAA temperatures twisted NbTi/CuNi wires are used which are heat sunk at the GGG salt pill. The amplifier SQUID is installed at the bottom plate of the liquid He-bath which is usually operated at a temperature between 1.8 K and 2 K. Figure 3.14 shows schematically the arrangement of the electrical wires used to operate and read out the two stage setup. The field current is supplied by the leads labeled I_{field}. The persistent current switch heater is contacted by the leads labeled I_{heater}. The amplifier is read out by a three wire measurement ($\pm U_{\mathrm{SQUID2}}, I_{\mathrm{ground}}$) to compensate for the voltage drop along the feeding wires. The dark grey shaded areas mark parts of the circuit which are surrounded by a superconducting shield made out of lead.

3.3.4 Magnetic Field Distribution

A simulation of the inhomogeneous magnetic field produced by the meander coil of a MagCal 15 is shown in fig. 3.15. The simulation was done by a finite element program called FEMM[10]. Since this program is designed to solve quasi two dimensional problems, the meander coil is represented by eight infinitely long parallel stripes perpendicular to plane defined by the paper. The magnetic susceptibility of the niobium stripes was chosen to be $\chi_{\mathrm{m}} = -1$, resembling perfect diamagnetism. For the simulation shown in fig. 3.15, the persistent current $I_0 = 60\,\mathrm{mA}$ was chosen and flows

[10]Finite Element Method Magnetics (v.4.0, freeware) by David Meeker; http://femm.berlios .de

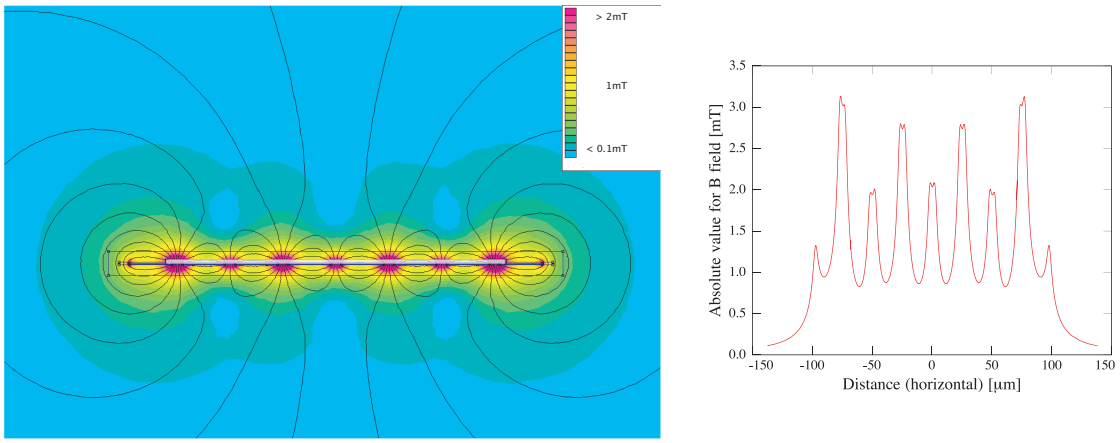

Figure 3.15 Flux density plot for a meander of the MagCal type with a persistent current of $I_0 = 60\,\mathrm{mA}$. On the right, absolute values of the magnetic field $1.5\,\mu\mathrm{m}$ above the niobium stripes are shown as a function of the distance along the meander.

in neighboring stripes in the opposite direction. Effects due to the finite dimension in the direction perpendicular to the stripes, are of course implicitly taken into account. However, the finite size effects in direction of the stripes, like the U-shaped connection between the stripes are neglected in this calculation. The direction of the magnetic field in between the meander stripes is perpendicular to the substrate with an alternating sign according to the direction in which the persistent current is flowing. Directly over each meander stripe the direction of the field is parallel to the substrate. The highest absolute value of the magnetic field of roughly 4 mT is found in between the meander stripes. A sensor with a height of $1.5\,\mu\mathrm{m}$ is indicated in fig. 3.15 by the shaded area. The magnetic susceptibility of the sensor material at $T < 50\,mK$ and x_{Er} is $\chi_{\mathrm{m}} < 0.1$ and thus the influence of the erbium ions on the magnetic field was neglected in this calculation.

The diagram on the right side in fig. 3.15 shows the absolute value of the magnetic field at a height of $1.5\,\mu\mathrm{m}$ above the niobium stripes. Outside the area that is covered by the meander, the absolute value of the magnetic field decreases almost exponentially. At a distance of $30\,\mu\mathrm{m}$ from the most outer stripe which is half the distance to the next meander, the field has decreased to 4% of the maximum value. Therefore, the magnetic fields produced by two neighboring meanders belonging to two SQUIDs operated at the same time, have a very small influence on each other. In other words, the magnetic cross talk will be small.

For the calculation of the detector properties in section 4, the distribution of the absolute values of the magnetic field inside the sensor volume is needed. This distribution $P(B)$ can be obtained by evaluating $|B|$ in the result of the finite element simulation at several thousand points inside the sensor volume. The expression $P(B)dB$ gives the probability that the magnetic field has the absolute value B in the interval $[B, B + dB]$. The distribution function is normalized and fulfills $\int_V P(B)dB = 1$. In fig. 3.16 this function is shown for a MagCal 15 with a $1.5\,\mu\mathrm{m}$ thick Au:Er sensor that covers an area of $160 \times 160\,\mu\mathrm{m}^2$. The geometric parameters regarded in

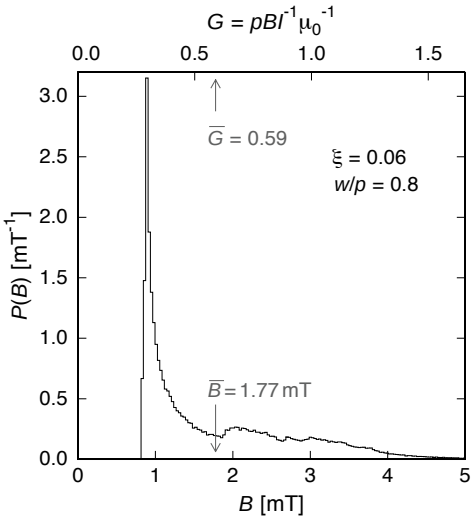

Figure 3.16 Absolute values distribution of the magnetic field inside a sensor 1.5μm high with an area of $160 \times 160\mu\text{m}^2$.

this simulation are thus $w/p = 0.8$ and the reduced sensor height $h/p = 0.06$ The persistent current $I_0 = 60\,\text{mA}$ running in the meander produces an average field of $\bar{B} = 1.77\,\text{mT}$. In addition the distribution is shown as a function of the coupling factor $G = pBr^{-1}\mu_0^{-1}$ which is explained in the next section.

3.3.5 Signal Size of a Meander Type MMC Detector

In section 2.2.3 the detector signal was discussed for a cylindrical sensor in a circular pick up loop placed in an external magnetic field which is approximately homogeneous throughout the sensor volume. This is not true anymore for a meander type geometry. The inhomogeneity of the magnetic field produced by the meander has to be taken into account when calculating the signal size.

A change of the magnetic moment $\delta M(\mathbf{r})d^3r$ in the volume d^3r which is situated at $\mathbf{r}$ leads to a change of flux $d(\delta\phi)$ in the area enclosed by the meander given by

$$d(\delta\phi) = \mu_0 \frac{G(\mathbf{r})}{p} \delta M \mathbf{r} d^3 r \quad . \tag{3.8}$$

As the local magnetization as well as the change of the magnetic moment is parallel to the local magnetic field that is generated by the meander itself, there is a simple relation between the coupling factors $G(\mathbf{r})$ and the absolute value of the magnetic field $B(\mathbf{r})$ at the same position $\mathbf{r}$ inside the sensor:

$$B(r) = \mu_0 G(r/p) \frac{I_0}{p} \quad . \tag{3.9}$$

Using equations 3.8 and 3.9 we can write the expected signal size as

$$\frac{\delta\phi}{\delta E} = \frac{1}{C_{\text{abs}} + \int_V c_{\mathbf{s}}(\mathbf{r}) d^3 r} \int_V \mu_0 \frac{G(\mathbf{r}/p)}{p} \frac{\partial M(B(\mathbf{r}, T))}{\partial T} \quad , \tag{3.10}$$

where the coupling factor and the temperature dependent magnetization have to integrated over the sensor volume $V = A \cdot h$. Here, c_s is the specific heat of the sensor material per volume and C_{abs} the heat capacity of the absorber. It is convenient to rewrite equation 3.10 using the distribution of magnetic fields $P(B)$ inside the sensor volume. Defining the weighted average of a quantity $X(B)$ by

$$\langle X \rangle_B = \int P(B) X \mathrm{d}B \tag{3.11}$$

and using 3.9 to express the factor G by the magnetic field we fiend

$$\frac{\delta\Phi}{\delta E} = \frac{V}{C_{abs} + V \langle c_s \rangle_B} \mu_0 \left\langle \frac{B}{p} \frac{\partial M}{\partial T} \right\rangle_B \quad . \tag{3.12}$$

The following chapter 4 will use this result to discuss the optimization possibilities for a meander type MMC detector in general and for a detector based on a MagCal 15 SQUID chip in particular.

3.3.6 Magnetic Johnson Noise of a Meander Shaped Detection Coil

To simulate the noise contribution due to the sensor and absorber for the MagCal setup, explained in the previous section, an expression for the spectral density for the magnetic Johnson noise will be derived in the following.

The meander can be represented by a superconducting coil. Let us assume a current, alternating with the frequency ω, that generates a magnetic field in the coil with inductance $L(\omega) = L' + iL''(\omega)$. The complex resistance of this coil is given by $Z = i\omega L(\omega)$. In our case losses occur due to eddy currents in normal conducting parts in the vicinity of the coil. They are represented by the real part $R(\omega) = \omega L''(\omega)$ of the impedance of the coil. As a consequence of the dissipation-fluctuation-theorem, the voltage across the coil is not constant but exhibits a voltage noise with a special power density $S_U = 4k_B T R_\omega$.

Each fourier component $\tilde{U}(\omega)$ of this voltage noise can be interpreted as flux noise $\tilde{\phi} = \tilde{U}/\omega$ because of the induction law $U = -\partial\phi/\partial t$. This leads to the expression

$$\sqrt{S_\phi} = \frac{1}{\omega}\sqrt{S_U} = \sqrt{4k_B T \frac{R(\omega)}{\omega^2}} = \sqrt{4k_B T \frac{L''(\omega)}{\omega}} \tag{3.13}$$

for the spectral density of magnetic flux noise. For the geometries and the materials discussed in this thesis the magnetic Johnson noise is frequency independent up to frequencies of several hundred kHz. The roll off at higher frequencies is due to the skin effect. In section 6.1 we compare the measured noise spectrum with the expected magnetic Johnson noise. For this comparison, the resistive losses of the coil were calculated using finite element methods, i.e. the program FEMM which was already mentioned.

4. Design considerations for a MagCal 15

In a recent work [Fle05] a numerical optimization of the energy resolution of MMCs with meander-shaped pick up coil had been presented, where it was assumed that the flux noise of the SQUID is the dominant source of noise. In this case the expression $S = (\partial\phi/\partial E)/\sqrt{L}$ is proportional to the signal-to-noise ratio and has to be maximized. Here $\partial\phi/\partial E$ is the signal size known from section 3.3.5. $L = \ell\mu_0 A_\mathrm{m}/p$ is the inductance of the meandering pick up coil, if finite size effects of the meander are disregarded, where ℓ is a dimensionless constant depending on the ratio of width to pitch of the meander stripes and A_m the area covered by the meander. Using equation 3.12 we find for a meander type MMC detector is given by

$$S = \sqrt{\frac{\mu_0}{\ell}} \frac{h\sqrt{A_\mathrm{m}/p}}{C_\mathrm{abs} + A_\mathrm{m}\, h_\mathrm{s}\, \langle c_s \rangle_G} \left\langle G \frac{\partial M}{\partial T} \right\rangle_G \quad . \tag{4.1}$$

Altogether S depends on nine parameters which have to be taken into account when designing a meander chip and a detector

$$S = S(C_\mathrm{abs}, g, \alpha, T, i_0, x, A_\mathrm{m}, h_\mathrm{s}/p, w/p) \quad . \tag{4.2}$$

Here C_abs is the absorber heat capacity, g the Landé factor of the paramagnetic ions, α the strength of the RKKY interaction, T the temperature of the sensor, $\bar{B}$ the average magnetic field in the sensor and x the concentration of erbium ions in the sensor material. These first six parameters are fixed typically by the material choice and the operating conditions. The other six parameters, i.e. the area A_m, the width w and the pitch p of the meander, as well as the height h_s, the Er-concentration x of the sensor and the field generating current I_0 in the meander, were assumed to be freely adjustable in order to maximize the signal-to-noise ratio.

From the results found in [Fle05] we only want to mention a few general conditions that lead to an optimal signal-to-noise ratio.

- $V\langle c_\mathrm{s}\rangle_G|_{opt} = C_{abs}$
- $h_s/p|_{opt} = 0.36$
- $w/p|_{opt} = 0.425$

Combining these three conditions we find, that the meander area $A_\mathrm{m} = C_{abs}/h_\mathrm{s}\langle c_\mathrm{s}\rangle_G$ is variable without a loss in sensitivity by adjusting the sensor height and the pitch. Since the detector, that was developed in the framework of this thesis, is based on a previously fabricated SQUID with meander-shaped inductances (see section 3.12), not all parameters mentioned above were variable.

The constants g and α are preset by the choice of the sensor material Au:Er. Since the sensor is fabricated by thin film techniques the erbium ion concentration in the sensor material is preset to $x = 750ppm$ by the concentration of the available

sputter target. The temperature T is determined by the refrigeration process and the magnetic field $\bar{B}$ is generated by the persistent current I_0 which is limited by the critical current of the meander coil. The geometric parameter $w/p = 0.8$ as well as the area A_m and thus the inductance of the meander is preset by the SQUID design of the MagCal 15. Although the geometry is not optimal compared to the results from the optimization in [Fle05], the performance of a detector, based on a MagCal 15 chip was simulated and optimized. Regarding the constraint that the inductance can not be varied, the qunatity chosen to be optimized is the signal size $\partial\phi/\partial E$ given by equation 3.12.

Concerning the geometry of the x-ray absorber, also the requirements of the experimental tasks in the EBIT experiment at the MPI for Nuclear Physics were taken into account. These are

- A high quantum efficiency from 3 keV to 10 keV and still 20% at 30 keV
- A sensible area greater than $0.5\mathrm{mm}^2$.

In the following the definition for the quantum efficiency

$$QE = 1 - \exp(h_\mathrm{abs}/l_\mathrm{At}) \tag{4.3}$$

is used, where l_At is the attenuation length of photons with a given energy E_γ in a specific material. The absorber is made out of gold, therefore the attenuation length of 10 keV x-rays in gold has to be considered to achieve the required quantum efficiency. The attenuation[1] length as a function of photon energy is shown in the left diagram in fig. 4.1.

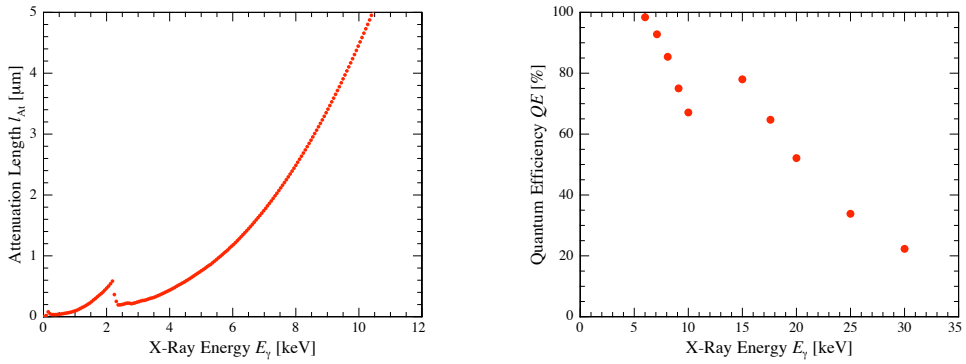

Figure 4.1 The left diagram shows the attenuation length of x-rays in gold. On the right side the quantum efficiency of a 5μm thick gold foil is shown as a function of the x-ray energy.

As can be seen from the diagram, the 10 keV photons have an attenuation length of roughly 5μm. Therefore, the absorber thickness $h_\mathrm{abs} = 5\mu\mathrm{m}$ was chosen. In the right diagram in fig. 4.1 the quantum efficiency of a 5μm thick gold foil is displayed as a

[1] Data taken from http://henke.lbl.gov; Au density $19.32\mathrm{kg/m}^3$ and grazing angle 90°

function of the photon energy. At an x-ray energy of 6 keV, the quantum efficiency is 98.4 % and at 10 keV it has a value of 67 %. For 30 keV x-rays the quantum efficiency is still 22.3 % and thus the first requirement can be fulfilled.
The absorber area defines the sensible area of the detector. To maximize it, the absorber has to be made larger than the area of the sensor resulting in a kind of mushroom shaped detector. For the MagCal 15 this area is limited by the distance of 60μm between the meanders. The meander dimensions are $195 \times 195\mu\text{m}^2$ thus an absorber area of $255 \times 255\mu\text{m}^2$ can be structured if no gap is left between the absorers. With a gap of $5\mu m$ between the absorbers the sensible area per pixel is $250 \times 250\mu\text{m}^2$. If all eight meanders of the MagCal chip are equipped with such an absorber, a sensible area of 0.5mm^2 is reached and the filling factor is 96%.

These considerations define the volume of the absorber and thus also its heat capacity to be $C_{\text{abs}} = 1.1\text{pJ/K}$ at a temperature of 50 mK. Therefore, only the sensor thickness h_{s} and area A_{s} are left to vary in order to maximize the signal height.

As demonstrated in section 3.3.5 the signal size $\partial\phi/\partial E$ is obtained based on the magnetic field distribution which can be simulated with the finite element program FEMM. This calculation was carried out for a detector at a temperature of $T = 50\text{mK}$ and a persistent current of $I_0 = 60\text{mA}$.

In fig. 4.2 the signal size is shown as a function of the sensor thickness h_{s} for a sensor area of $A_{\text{s}} = 160\mu\text{m}^2$. For small sensor thicknesses the sensor heat capacity C_{s}

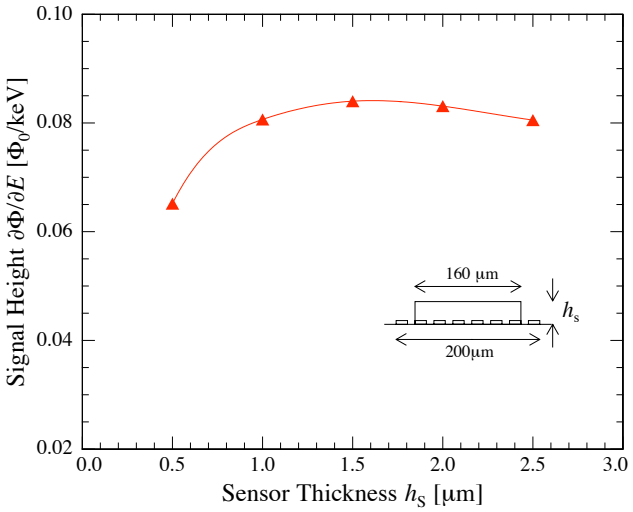

Figure 4.2 Simulated values for signal size as a function of the sensor thickness h_{s} for a sensor with the area $A_{\text{s}} = (160\mu\text{m})^2$. The solid is only a guide for the eye.

is smaller than the absorber heat capacity C_{abs}. Consequently, the energy transfered to the sensor and thus the signal size $\partial\phi/\partial E$ is reduced by the factor

$$\frac{C_{\text{s}}}{(C_{\text{abs}} + C_{\text{s}})} \quad . \tag{4.4}$$

The signal size rises with increasing sensor thickness until the ratio of sensor and total heat capacity maximizes the signal size, resulting in a broad maximum. The optimal sensor height is found to be 1.6μm. For greater sensor thicknesses the signal

size decreases again which can be accounted to the fact that the magnetic field and thus also the magnetization, decreases fast with height over the meander. Therefore, the spins in the sensor material for thicknesses higher then 2μm do not effectively contribute to the signal size.

In fig. 4.3 the signal size is shown as a function of the sensor area A_s for three different sensor heights. Data was simulated for sensor areas of $(120\mu\text{m})^2$, $(160\mu\text{m})^2$, $(180\mu\text{m})^2$ and $(200\mu\text{m})^2$. For small areas the three cases show a similar behavior.

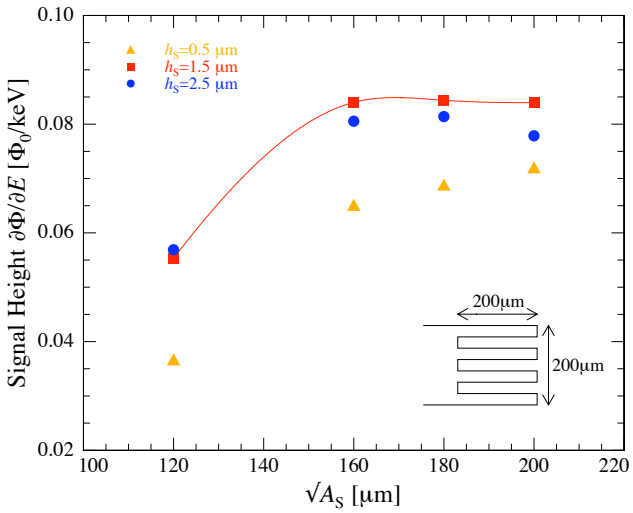

Figure 4.3 Simulated signal sizes as a function of the sensor area A_s for different sensor thicknesss of $h_s = 0.5\mu$m, $h_s = 1.5\mu$m and $h_s = 2.5\mu$m.

As in the discussion of diagram 4.2 the ratio of sensor heat capacity and total heat capacity is small leading to a reduced signal size in this range. Therefore, the signal size increases with increasing sensor area. For areas larger then $(160\mu\text{m})^2$ the displayed curves show substantially different behavior. In the case of $h_s = 0.5\mu$m, the ratio $C_s/(C_{abs} + C_s)$ will reach its optimal value for an area larger than $(200\mu\text{m})^2$. For $h_s = 2.5\mu$m the signal size reaches a maximum between areas of $(160\mu\text{m})^2$ and $(180\mu\text{m})^2$ and clearly decreases again for larger areas. This can be explained by the fact that the magnetic field decreases fast in lateral direction for areas larger then $(160\mu\text{m})^2$ as can be seen from the magnetic field distribution 3.15. Therefore, the magnetization in the sensor material in this region is not sufficiently high to effectively contribute to the signal size. This effect is rather pronounced for sensors with this thickness. In the case of $h_s = 1.5\mu$m the maximum of the signal size is reached for areas between $(160\mu\text{m})^2$ and $(180\mu\text{m})^2$. The maximum is very shallow which makes a sensor of $A_s = (160\mu\text{m})^2$. A reasonable choice since it minimizes the amount of sensor material and leads to 98.7% of the maximum signal size. The maximal signal size achieved with this detector is $S_{max} = 0.08\phi_0/\text{keV}$ which corresponds to a flux change of $0.48\,\phi_0$ at a photon energy of 6keV.

5. Microfabrication

This chapter will give a detailed description of the techniques used to fabricate the detector described in the previous chapter. The lithographic patterning, the sputtering processes and their essential parameters are presented.

5.1 Sputtering the alloy Au:Er

A common choice for the deposition of an alloy is the sputter deposition because this technique does not depend on the melting points of the constituents of the alloy. Since the melting point of gold is 1064°C while erbium melts at 1497°C, a deposition of the sensor material by an evaporation technique is impossible. Therefore, a dc magnetron sputter process is used. The sputter chamber is therefore equipped with a 2“ target made out of bulk gold erbium which is located in a distance of roughly 50 mm from the substrate. The substrate is cooled by a water cooling system which keeps the temperature on the substrate holder below 100C°. Since erbium easily oxidizes and would in consequence loose its paramagnetic properties, a low base pressure and a clean processing gas is of major importance. Therefore, the chamber is evacuated to a base pressure of $5 \cdot 10^{-8}$mbar and then flooded with clean argon (6N) till the pressure reaches $5 \cdot 10^{-3}$mbar which is kept constant during deposition. To initiate

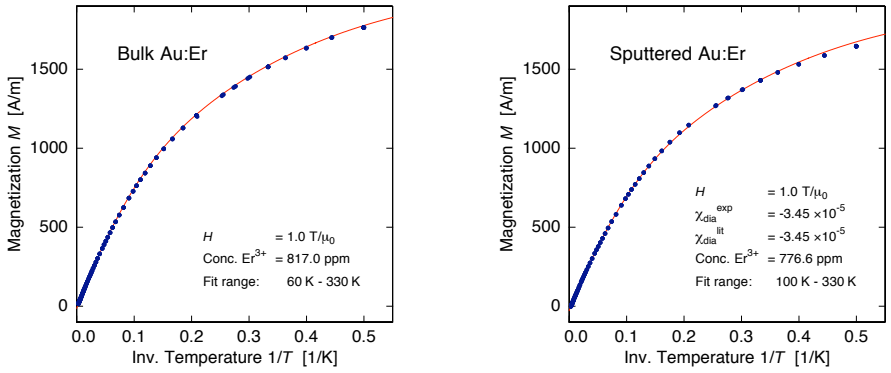

Figure 5.1 Magnetization measurements in a magnetic field of 1 T in the temperature range from 2 K to 300 K using a commercial SQUID Magnetometer[b]. In a) for a flake taken from the Au:Er sputter target and b) for a sputtered foil. The solid line indicates data from a simulation described by [**?**].

[a]MPMS-XL, fabricated by Quantum Design, San Diego, CA
[b]MPMS-XL, fabricated by Quantum Design, San Diego, CA

the sputter process an argon plasma is lighted by a strong electric field between the substrate and the target. By means of a magnetic coil below the target, the argon ions are forced into a spiraling movement which brings the ions back into the electric

field which successively accelerates them onto the target surface. The impact of the ions is high enough to remove atoms and clusters of atoms from the material. In addition the spiraling movement improves the plasma density due to continuous collisions of argon ions with neutral argon atoms. At a power of 40 Watts the achieved deposition rate is 1.6 nm/s. The gold absorber is sputtered with the same parameters and deposition rate resulting in a gold film with an Residual Resistivity Ratio (RRR) of 1.7.

As discussed in section 2.2 the paramagnetic sensor needs to have the thermodynamic properties of bulk Au:Er. Therefore, the agreement of the behavior of deposited material and bulk material is very important to assure the predicted performance of the detector. In fig. 5.1 a) the magnetization behavior of a flake taken from the target is measured (points) and compared to the theoretical data (solid line) calculated as described in [**?**]. The diagram b) in the same figure shows the equivalent comparison for a sputtered gold erbium foil. The measurements were carried out in a magnetometer in the temperature range of 2 K and 300 K. The measured data corresponds to the simulated data for 810 ppm in the bulk material case and 775 ppm in the case of sputtered foil. The difference might be due to the magnetic moments of the erbium ions, which result in a reduced sputtering rate of the dc-magnetron-sputtering process. However, the measured data is in a good agreement with the theoretical curve for the chosen concentration, indicating a good quality of the film.

5.2 Microfabricating a detector with overhanging absorber

Two lithographic processes were used, one to fabricate the sensor and in a second step the absorber on top of the sensor. Figure. 5.2 illustrates the essential lithographic steps of the processes.

To make the processing possible and for an easier handling, the chip was glued into a metal holder which was made out of a copper disc with a hole in its center. To allow for a good alignment of the chip's surface with the surface of the copper disc, the chip was fixed up side down in the hole with a drop of superglue. The hole was then sealed with Stycast 2850 FT[1]. A clean surface is important to achieve a good adhesion between the meander surface and the Au:Er layer. Therefore all cleaning and lithographic steps were carried out in a clean room class 100[2]. The surface of the chip was cleaned from any glue residue with acetone and isopropanol in combination with a ultrasonic bath at low intensities.

In fig. 5.2 I) the basic steps to structure the Au:Er sensor in a lift off process are illustrated. By spin-coating, the chip was covered with a 12μm thick layer of AZ nLOF 2000[3] negative photoresist. After a soft bake of 13 min on a hot plate at 100C°, the resist was exposed in a standard mask aligner for 20 s to the light of a

[1] Emerson and Cuming, Westerlo, Belgium

[2] 100.000 particles smaller 0.1μm per cubic meter of clean-room air; equivalent to ISO 5

[3] All AZ products are developed by Clariant and commercially available from Microchemicals GmbH, Ulm

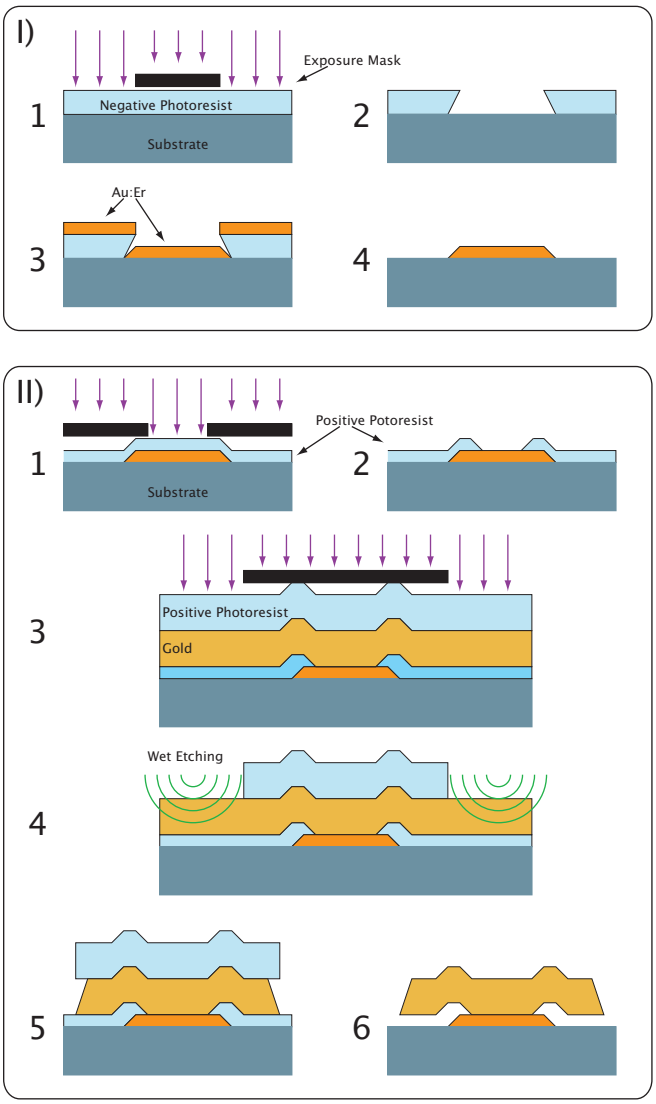

Figure 5.2 Basic steps for the lithographic patterning of an Au:Er sensor I) with a large gold absorber on top II) leading to a mushroom shaped detector.

mercury gas discharge lamp with an intensity of roughly 24mW/cm^2. In this step an exposure mask was used which is transparent to the light except for a $160 \times 160\mu\text{m}$ square aligned to cover the meander. A cross linking bake needed to polymerize the exposed resist was carried out on a hot plate for 2 min at 120C° before developing the photoresist for 1 min 30 s in AZ 826 MIF which is a metal ion free developer. This developer was chosen to minimize the risk of contaminating the sensor material with metal ions. With these parameters the resist forms a reasonably large undercut, like it is sketched in picture 2 of fig. 5.2 I) which is desirable for a clean lift off. The Au:Er sputtering step was performed outside the clean room. To allow for an easy lift off only a small area around the meanders was covered with the Au:Er layer the rest of the chip and the copper disc was protected by an aluminum foil. The lift off

itself was again carried out under clean room atmosphere in a bath of 80C° warm NMP[4].

Fig. 5.2 II) illustrates the steps for a wet etching process which is used to structure an overhanging gold absorber on top of the sensor. An important aspect when choosing the photoresist for an etching process is its resistiveness against the etchant. To etch noble metals like gold or platinum aqua regia[5] is commonly used. The resists for this process were AZ 5214 E for thin layers and AZ TIxLift for thick layers up to $10\mu m$. Both proofed to withstand the acid long enough to cleanly fabricate the absorber.

After cleaning with acetone and isopropanol the chip was spin-coated with a layer of AZ 5214 E positive resist in a way to have roughly the same height as the sensor. Following a soft bake for 2 min at 90C° on a hot plate, the resist was exposed in the aligner for 4 s. To ensure that the structure in the resist does not exceed the boundaries of the sensor, an exposure mask with a $125 \times 125\mu$m square was used. The photoresist was then developed in the metal ion free developer for 2 min resulting in a structure as illustrated in picture 2 in fig. 5.2 II). The absorber gold layer is then sputter deposited in the dc magnetron sputter machine, again outside the clean room. The chip which is now completely covered by the gold film was spin coated with a 7μm thick layer of positive photoresist. The resist used in this step was the positive photoresist TiX Lift which is barely attacked by aqua regia. After a soft bake on a hot plate for 20 min at 90C° an exposure using a mask with a $250 \times 250\mu\text{m}^2$ square was carried out for 10 s. The resulting structure as well as the etching step is illustrated in step 4 in fig 5.2. In a fresh bath of aqua regia at room temperature the etching rate is roughly 1μm/min. After the removal of all the gold around the absorber, the remaining photoresist is dissolved in a DMF[6]-bath for several hours. Fig. 5.3 shows a picture taken in a Raster Electron Microscope (REM) of a series of two by four mushroom structures on a glass substrate which were fabricated with this process. The dimensions are similar to those of the detector. Due to the isotropic etching, gold was also removed laterally on the absorber edges which led to slightly tilted side walls. The resulting absorber side length is thus roughly 5μm smaller on each side compared to the expected area of $250 \times 250\mu\text{m}^2$. This leaves a gap of about 20μm separating the absorbers.

5.2.1 Microstructured detectors on a MagCal 15 chip

With the sputtering and etching process described above two detectors were structured on a MagCal 15 chip. Figiur 5.4 shows a micrograph of the chip after it was already installed on the experimental holder. The imprint of the meandering structure can nicely be seen in the parts of the absorber which are in contact with the sensor. Absorber parts, where this imprint is not present, are thus free standing. The used process has proven to yield clean and precise results, however due to problems

[4] N-Methyl-2-pyrrolidone
[5] $HNO_3 + 3HCl$ in the ration 1:3
[6] Dimethylformamide

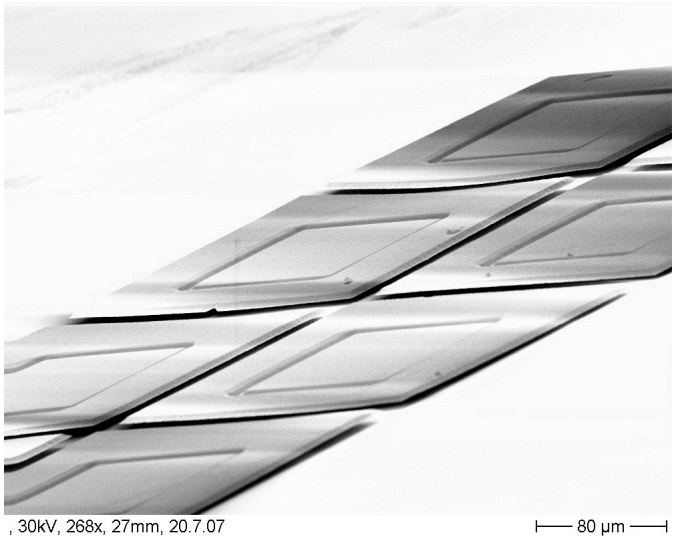

Figure 5.3 REM picture of the first successful test to microstructure 2 by 4 mushroom-shaped structures on a glass substrate with the process described above.

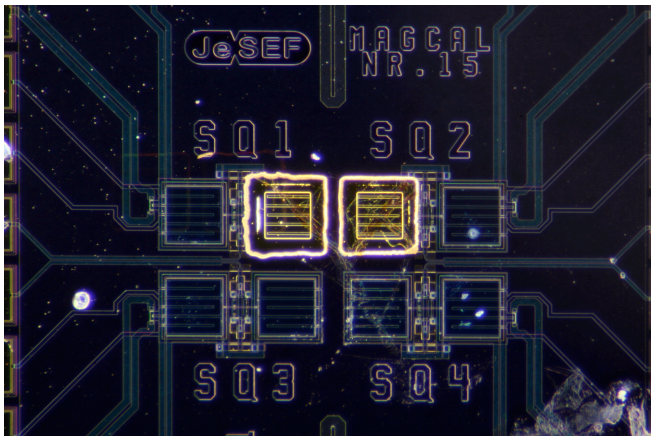

Figure 5.4 MagCal 15 chip with two microstructured detectors with overhanging absorbers on top of a sensor.

during the lithographic structuring of the photo resist for the etching step and during the etching itself, the absorbers have a rather irregular shape and an area smaller then expected. An estimation from this and other picture results in an absorber area of roughly 220x220μm^2.

Alternative techniques

Besides wet etching there exist a few alternatives to achieve structures similar to the one described above, two of them will be described shortly in the following since they represent promising techniques which will be available in the near future.

After the sensor has been deposited, it is possible to create a mushroom shaped mold on top of the sensor out of two layers of photoresist, where the top edge of the mold has to have an undercut. After depositing the absorber, the gold film surrounding the absorber mold can then be removed in a lift off step. Besides its simplicity this process has the advantage of resulting in precise structures without the uncertainty of a lateral removal of the gold like it was present in the wet etching. Furthermore there is not the risk of damaging the chip or the sensor with the acid.

However, this technique was not successful up to now since the absorber was always removed with the photoresist in the lift off step. The reason seems to be that the solvents in the second photoresist layer dissolve some parts of the first layer. This leads to a solid transparent film on top of the sensor which prohibits any contact between sensor and absorber. In the future this problem might be solved by a better choice of the employed resists or an ion-gun cleaning of the sensor surface preceding the sputtering step.

Probably the most advanced technique is the dry- or plasma etching. Plasma etching is based on the chemical reaction of a radical with a metal or non metal surface in combination with the sputtering of the same surface. This leads to an anisotropic etching process which is controllable from the outside and can produce structures with an extremely high aspect ratio. In the process described above it would simply replace the wet etching step. Depending on the amount of oxygen in the plasma, the process can be arranged to produce side walls with or without a tilt. Smooth side walls are desirable when structuring multiple layers of conducting material on top of each other to reduce the risk of electrical shorts since the conducting layers are only separated by a thin isolation layer.

6. Experimental Results

In the following the results obtained with the setup of two detector on a MagCal 15 chip will be presented. To characterize both pixels the behavior of the detectors in terms of noise, the temperature dependence of the magnetization and the performance in spectroscopic measurements of a ^{55}Fe source are discussed. Furthermore this setup offers the possibility to study the magnetic cross talk between two detectors as well as the behavior of the detectors while operating two SQUIDs on the same substrate.

6.1 Noise at 4K

As was already discussed in sections 3.4 and 3.3.6 the noise level of a detector, read out by a two-stage SQUID setup, is a sum of different contributions. A noise measurement at a temperature of 4.2 K of one of the two detectors studied in this work is shown in fig. 6.1. The white noise level between 10 Hz and 10 kHz has a value of $5.5\,\mu\Phi_0/\sqrt{\text{Hz}}$. This overall noise level can be understood by calculating every

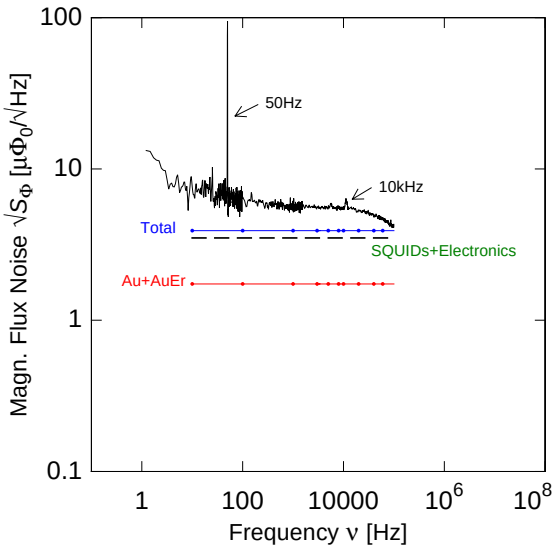

Figure 6.1 Noise measurement at $T = 4.2$K. The prominent peak has its origin in the 50 Hz noise of the mains. At 10 kHz a harmonic of this frequency is visible. The major contributions by the to the noise level are displayed.

contribution already introduced in equation 3.6. Additionally the contribution of magnetic Johnson noise by the sensor and absorber has to be taken into account. These single contributions have to be converted into the apparent flux noise in the detector SQUID. The voltage-to-flux-transfer coefficient of the amplifier SQUID $\partial V/\partial\phi_2 = 1273\mu V/\phi_0$ and the flux-to-flux amplification of $G_\phi = 0.87$. The read out electronics at room temperature contribute with a voltage noise of $0.33\text{nV}/\sqrt{\text{Hz}}$ which equals a flux noise level in the detector SQUID of $0.3\,\mu\Phi_0/\sqrt{\text{Hz}}$. The amplifier SQUID array which is mounted on the 4 K-stage of the cryostat, exhibits a noise

level of $0.4\,\mu\Phi_0/\sqrt{\text{Hz}}$ which adds $0.46\,\mu\Phi_0/\sqrt{\text{Hz}}$ to the detector noise level. The voltage noise of the gain resistor $R_g = 0.27\Omega$ at 4.2 K is $7.9\text{pV}/\sqrt{\text{Hz}}$ which converts to a flux noise of $1.36\,\mu\Phi_0/\sqrt{\text{Hz}}$ in the detector SQUID. For this last conversion the voltage-to-flux-transfer coefficient of the detector SQUID alone ($5.8\mu\text{V}/\phi_0$) had to be considered. The SQUIDs on a MagCal chip have a relatively high intrinsic noise level of $3.2\,\mu\Phi_0/\sqrt{\text{Hz}}$. All these contributions added up quadratically gives a flux noise level of $\sqrt{S_{\phi_0}} = 3.5\,\mu\Phi_0/\sqrt{\text{Hz}}$. This noise level is indicated in fig. 6.1 by the dashed line.

The contribution of sensor and absorber was calculated in section **??** and the results are displayed in fig. 6.1. For the absorber a sputtered gold film of the dimensions $240 \times 240 \times 5\mu\text{m}^3$ with an RRR of 1.7 was simulated and for the a sensor a sputtered Au:Er film with the dimensions $160 \times 160 \times 1.5\mu\text{m}^3$. Taking all of these contributions into account results in an overall noise level of $3.9\,\mu\Phi_0/\sqrt{\text{Hz}}$. There is not a good explanation for this discrepancy. One possibility is that the collimator made out of high purity (5N) gold is too close to the absorber surface and thus the magnetic Johnson noise due to the collimation has to be taken into account.

6.2 Noise at Low Temperatures

In the range of the working temperatures, the white noise level of the magnetic flux noise is reduced according to the temperature dependence of all contributions. Additionally low frequency contributions like they were discussed in section 2.3 become only visible for temperatures below 120 mK. The data set in fig. 6.2 which reaches up to 10^6Hz shows a white noise level at a value of $1.9\,\mu\Phi_0/\sqrt{\text{Hz}}$. It was measured for a persistent current through the meander coil of 80 mA and a temperature according to the cryostats thermometry of 27 mK on the experimental platform. For low frequencies the noise shows a $1/\sqrt{f}$ until it levels into a plateau roughly at 10 kHz. For frequencies beyond 100 kHz, the noise level drops because of the skin effect. The acquisition program averages over several hundred time windows and for this spectrum an algorithm was applied which rejects time windows in which a pulse occurred. The contribution of the room temperature electronics remains unchanged because its operating conditions are similar at all temperatures. Since voltage noise exhibited by the gain resistor scales with the square root of the temperature it adds $0.5\text{n}\phi_0/\sqrt{\text{Hz}}$ to the flux noise and is compared to other contributions negligibly small. In section 3.2.2 an estimation of the intrinsic SQUID noise was given which is proprtional to $\sqrt{T}$. Since the liquid helium bath is pumped, the temperature of the 4 K-stage drops to 1.9 K. The noise contribution of the array is thus reduced by the factor $\sqrt{1.9\text{K}/4.2\text{K}}$ to a value of $0.3\,\mu\Phi_0/\sqrt{\text{Hz}}$. Due to the integrated design of the MagCal discussed in section 3.3.1 the constant biasing of the SQUIDs and the decoupling of the electrons from the phononic system the shunt resistors remain between 200 mK and 300 mK. Taking this into account the intrinsic noise of the detector SQUIDs is reduced by the factor $\sqrt{300\text{mK}/4.2\text{K}}$ which leaves a contribution of $0.8\,\mu\Phi_0/\sqrt{\text{Hz}}$. The largest contribution to the noise level at low temperatures comes from the gold absorber and has a calculated value of $1\,\mu\Phi_0/\sqrt{\text{Hz}}$. In total these contributions re-

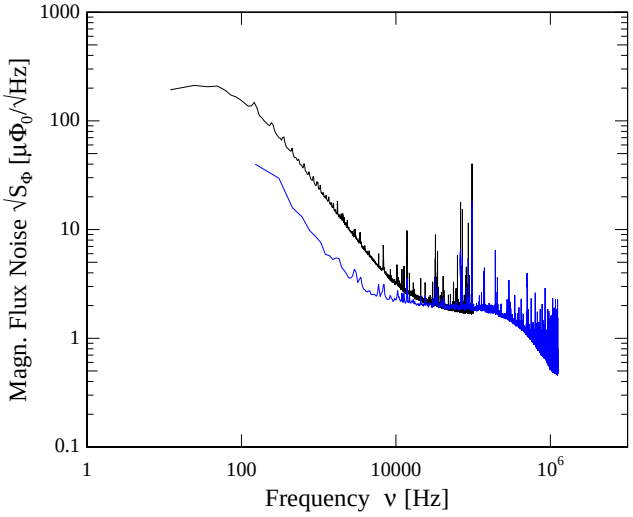

Figure 6.2 Both curves are noise measurements taken at 27 mK. For the dark curve the contribution due to x-ray pulses are filtered out. The light curve shows the unfiltered case.

sult in a noise level of only $1.3\,\mu\Phi_0/\sqrt{\text{Hz}}$. The discrepancy to the measured value can not be easily explained. Since these SQUIDs are only designed for temperatures down to 2 K it is likely that the frequencies

The black curve in fig. 6.2 shows a noise measurement without filtering the contribution due to x-ray pulses. Since the pulses which are surveyed with this detector rise and decay with time constants in the milli-second range, their contribution lies mainly below 1 kHz. By adding this to the already existing contributions the offset for low frequencies can be explained. The noise levels into a plateau of roughly the same value as the curve taken with a pulse rejection filter. This comparison shows that the white noise level is not lifted due to x-rays and thus represents no limitation for the energy resolution that can be obtained.

6.3 Magnetization of the Au:Er Sensor

As the magnetic field produced by the meander-shaped coil is inhomogeneous, the absolute value of the magnetic field as well as the magnetization of the sensor material is a function of the position inside the sensor volume. Therefore, the magnetization $M(B,T)$ of the sensor material Au:Er can not directly be measured with this setup. However, the magnetic flux $\phi(I_0,T)$ in the SQUID is a quantity that is closely related to the magnetization and it can directly be observed in the experiment. For any given persistent current I_0 and temperature T, $\phi(I_0,T)$ can be calculated using the magnetic field distribution $P(B)$ introduced in section 3.3.5 and the numerically calculated magnetization $M(B,T)$ of Au:Er as described in section 2.2.2. While sweeping through the temperature range during the experiment, the voltage drop across the feedback resistance of the FLL circuit is measured for both detectors P1 and P2. To avoid large feedback currents a voltage reset level can be set which forces the the working point to jump, by an integer number of flux quanta, to a new position, in which less flux is in the SQUID loop when the threshold level is

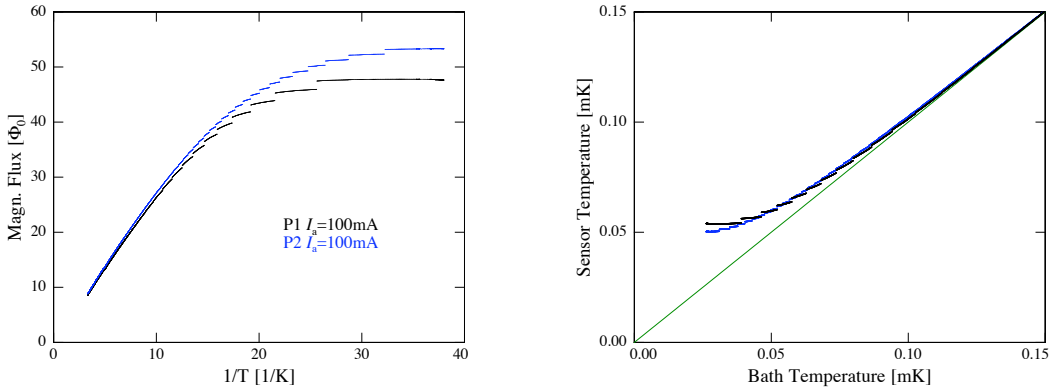

Figure 6.3 Magnetic flux in SQUID one and SQUID two of detector P1 and P2, respectively, as a function of inverse temperature. The injected persistent current was $I_a = 100mA$ for both detectors. From numerical simulations a value of an effective persistent current of 74 mA in meander one and 68 mA in the second meander, were deduced.

reached. Unfortunately, the current running through the superconducting feedback coil appears to be a large source of parasitic heating in the setup discussed here. The measurements obtained in FLL mode show a behavior which is displayed in the left diagram in fig. 6.3 and can be explained as follows. Due to the heating of the feedback currents, the sensor is not in thermal equilibrium with the experimental platform. In the high temperature part these heating effects are small compared to the bath temperature and thus not dominant. Towards lower temperatures the heating increasingly distorts the measurement which can be seen in fig. 6.3. When the feedback current is set back to a small value and the heating is likewise small, the chip temperature drop suddenly till it reaches an equilibrium with the bath temperature. These sudden drops can nicely be seen in the measurements since each time several flux quanta are passed.

To obtain the actual value of the persistent current in the meander the slope of the curve at high temperatures is compared to the one of numerical calculations for a set of currents I_a. Once the current that describes the measured data is found, the relation $\phi_{\mathrm{theo}}(T)$ can be used to calculate the chip temperature by $T_{\mathrm{chip}} = \phi^{-1}_{\mathrm{theo}}(\phi_{\mathrm{exp}})$, where $\phi^{-1}_{\mathrm{theo}}(\phi_{\mathrm{exp}})$ is the inverse function of $\phi_{\mathrm{theo}}(T)$. The diagram on the right in fig. 6.3 shows the sensor temperature extracted in this way as a function of the temperature of the bath measured by the thermometry of the cryostat. This comparison was then used to derive the actual sensor temperature. The data deviates from the linear behavior towards low temperature which can be explained by the power dissipation on chip due to bias- and feedback currents. The difference of pixel one and pixel two results most likely from a higher bias- and feedback current of the second detector P2.

As demonstrated in fig 6.3, for each magnetization curve a current was simulated which agrees with the high temperature part of the data and therefore represents an effective persistent current in the meander. In figure 6.4 the magnetization curves for

both pixels are compared. Additionally two simulated curves for 60 mA and 80 mA are displayed. It has to be recognized that the effective persistent currents deviate from the injected values. The effective current in the meander when 60 mA was

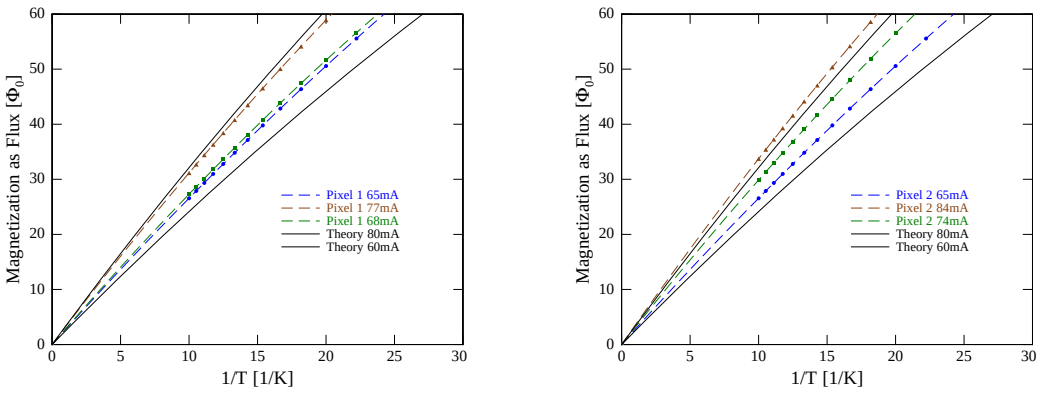

Figure 6.4 Comparison among magnetization curves for three effective currents.

injected is roughly 65 mA for both detectors. For an injected current of 80 mA an effective current of 77 mA was found for the first detector and an effective current of 84 mA for the meander of the second detector. In the case of injected 100 mA, an injected current of only 68 mA and 74 mA was found in meanders one and two, respectively.

An interpretation of this behavior based only on this set of data is difficult to give. Since the power dissipation strongly deforms the curves, magnetization measurements were obtained with a new technique which does not use the FLL circuitry and thus no heating due to feedback currents was present. These measurements showed results which could be interpreted better. A measurement without a current in the meander and with different polarities of the current running through the ADR magnet showed that a remanent field existed in the region of the detectors. This field lead to a magnetization curve $\phi(T)$ that corresponds to a persistent current of roughly 60 mA and a mean field of 1.9 mT. It was found to be independent of the ADR-magnet. To support this observation, two measurements were carried out in which a small current with a positive sign was injected in the first SQUID and a small current with a negative sign in the second. The resulting magnetization curves were significantly different which would result from the enhancement of the field by the current with one sign while the current with opposite sign decreased the local field at the sensor.

A possible explanation for this large background field is a magnetic field which was frozen in the superconducting lead shields. This scenario is possible when the superconducting lead becomes normal conducting in an external magnetic field while recharging the salt pills. Once the superconducting state is restored, the field which is present inside is kept constant by screening currents. Therefore, the larger part of the magnetization signal is caused by the parasitic background field which leads to difficulties in the interpretation of the measured data. The open-loop measurement

technique and the magnetization data acquired wit this techique will be presented in section 6.6.1.

6.4 X-Ray Spectroscopy

In the following detector signals caused by the absorption of single x-rays at different temperatures and persistent currents will be analysed. In the last two paragraphs of this section a full spectrum of a ^{55}Fe source is presented and by means of this spectrum the linearity of the detector will be discussed. The radioactive source used in this experiment is an ^{55}Fe-source with an activity of 4 MBq. 90% of all decays end via a K-electron capture in ^{55}Mn. The line with the highest x-ray intensity is caused by the subsequent transition of an electron from the L- into the K-shell, called K_α-line, emitting photons with an energy of 5.9 keV. The transition of an electron from the M- into the K-shell, the K_β-line, is nine times less frequent and results in the emission of a 6.5 keV photon (see [Höl97]). Single events where recorded with the acquisition scheme mentioned in section 3.2.5.

6.4.1 Pulse Shape

Fig. 6.5 shows a typical K_α pulse with an energy of 5.9 keV at a temperature of the sensor of 51 mK. The magnetic field in which the sensor is located in this measurement is the sum of the parasitic background field, as discussed in the previous section, and the field that is produced by the persistent current $I_0 = 75$mA in the meander. The injected current in this measurement was $I_a = 100$mA.

The change of magnetization in the sensor upon an incident x-ray is measured as the change of magnetic flux in the SQUID. The conversion of the absorbed energy into thermal energy is a sequence of different processes explained in detail in [CE05]. Regarding these processes and their characteristic time constants, a rise time below 1μs for pulses at 50 mK is expected. Before the absorption of energy the value for the magnetic flux is constant except for high broad band frequency noise contributions. After the absorption of energy the magnetization in the sensor changes and maximal pulse height is reached after about 2μs. The decay is a sum of two exponential functions

$$a_1 e^{-t/\tau_2} + a_2 e^{-t/\tau_2} \tag{6.1}$$

with a short time constant τ_1 and a long second time constant τ_2 which describes the thermalization of the sensor with the thermal bath. The fast time constant is likely to be the result of a heat flow into a separate system which has its origin in the interaction of the nuclear spins of the gold atoms with the embedded erbium ions in the gold matrix which lifts the degeneracy of the energy levels of the gold nuclei. A more detailed explanation of this interaction mechanism and the resulting heat capacity can be found in [Fle03].

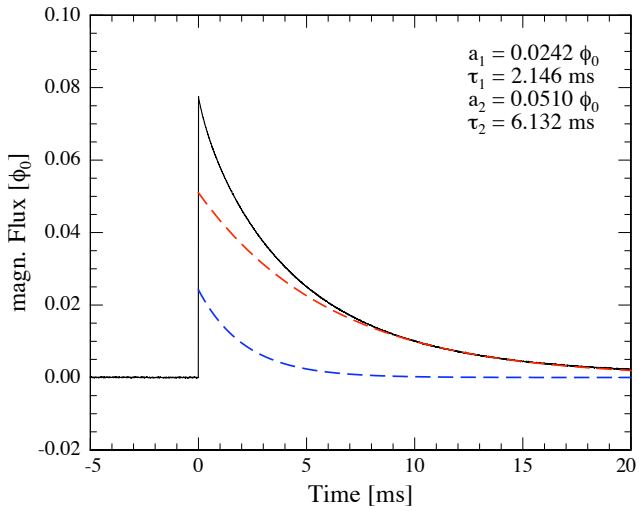

Figure 6.5 K_α pulse acquired at 51 mK with an effective current of 100 mA. The dashed lines mark the exponentials which were used to fit the decay time of the pulse.

6.4.2 Pulse Height

Fig. 6.6 shows the change of flux in the SQUID when a x-ray with the energy of 5.9 keV is absorbed. The pulses were acquired in the condition described in the previous paragraph at three different bath temperatures. Pulse height as well as decay time decrease with increasing temperature. For small constant magnetic fields, like it is the case in these measurement, the heat capacity of the spin system decreases with rising temperature while the heat capacity of the electron system rises. Therefore, an energy input δE at low temperatures leads to more spin flips than the same energy input at higher temperatures and thus also to a smaller flux change $\delta\phi$ in the SQUID. The decay time τ_2 also decreases with increasing temperature. This

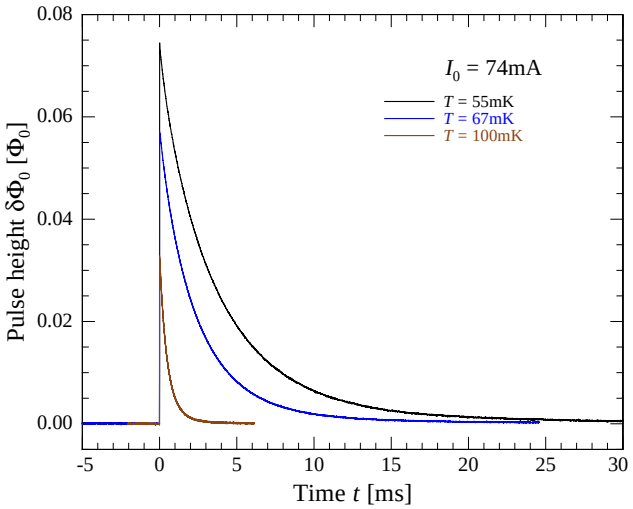

Figure 6.6 K_α pulses acquired with a persistent current of 74 mA at three different temperatures.

behavior is due to an improved thermal conductance between the sensor and the surface of the chip at higher temperatures. This thermal conductance is limited by

the Kapiza resistance which is proportional to T^3. This strong temperature dependence dominates the temperature dependence of the relaxation time, which can be approximated by $\tau \simeq C/G$, because the total heat capacity of the detector shows only a rather weak temperature dependence in this temperature range.

For a thorough understanding of the detectors, a comparison between the simulated pulse heights and the measured heights is analyzed for different currents as a function of temperature. The K_α pulse at 100 mK, shown in fig 6.6 has an amplitude of 3.3% of a ϕ_0. From the numerical simulation for this persistent current and temperature, an amplitude of 9.8% of a ϕ_0 was predicted which is a factor three more. This discrepancy is likely to be explained by the parasitic magnetic background field and the enormous heating with the feedback current during the acquisition. In particular the external field can cause the alignment of spins in parts of the sensor which are not coupled well to the meander. This is for example the case for the region directly over a niobium stripe. Aligned spins in these regions increase the heat capacity of the spin system while they barely contribute to the signal. Therefore, due to the increased heat capacity they reduce the signal size.

6.4.3 The X-Ray Spectrum of a ^{55}Fe-Source

After the discussion of single events and the basic properties of the detector, a x-ray spectrum of a ^{55}Fe source will be discussed. To assign energies to each event, a the χ^2-minimization method was used. It deploys an algorithm that assigns to each signal $s(t)$ the energy E which minimizes the root-mean-square-deviation given by $\chi^2 = \sum_i (s(t_i) - E \cdot r(t_i) + E_0)^2$, where $r(t)$ is a reference signal which is obtained by averaging a large number of pulses and E_0 represents a variable signal offset. At the minimum of χ^2 the energy E is found to be

$$E = \frac{\langle sr \rangle - \langle s \rangle \langle r \rangle}{\langle r^2 \rangle - \langle r \rangle^2} \quad . \tag{6.2}$$

The spectrum is shown in fig. 6.7 in form of a histogram divided into energy intervals

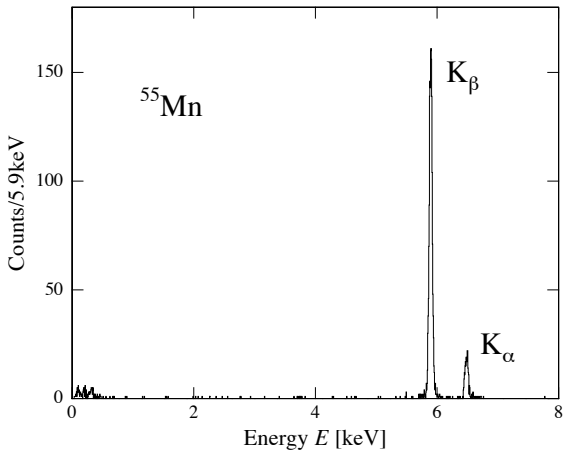

Figure 6.7 Measured spectra of the characteristic x-ray radiation of ^{55}Mn. The prominent peaks belong to the K_α-line (5.899 keV) and the K_β-line (6.490 keV).

of 5.9 eV. It was acquired at a temperature of $T = 50$mK. The magnetic field inside the sensor volume is the sum of the parasitic background field discussed above and the field that is produced by the persistent current of $I_0 = 68$mA in the meander. The spectrum comprises 2500 events which were acquired at an average rate of 2.4 events per second in a total acquisition time of 17 min. During the time of this measurement the temperature of the experimental platform was not actively stabilized.

The most prominent peak is the K_α-line which was also used to calibrate the energy scale. The majority of events at lower energies in the spectrum are caused by photons which do not deposit their energy in the absorber, but are absorbed by the substrate or the absorber of the neighboring detector. Those events can be clearly distinguished from direct hits because of the slower signal rise time.

To determine the energy resolution in the spectrum, the K_α-line displayed in fig. 6.8 was further analyzed. A value for the energy resolution was obtained by fitting a gaussian distribution to the K_α-line and determining the full width of the fit at its half maximum (FWHM). An energy resolution of $\triangle E_{\mathrm{FWHM}} = 71$eV at 5.9 keV was found. Further understanding of the detector performance can be gained from the energy distribution of baselines which have been acquired with every 10^{th} pulse. A baseline contains the noise contributions which is superimposed on every event. If the same algorithm, that assigns an energy to each triggered event, is applied to acquired baselines, one obtains a line in the spectrum at $E = 0$, which represents the contribution of broad band noise to the instrumental line width. On the right side in fig. 6.8 this distribution is displayed in form of a histogram in which the energies are sorted into intervals of 5.9 eV. The gaussian fit results in an energy resolution of $E_{\mathrm{FWHM}} = 67$eV. The difference between the baseline width and the energy resolution at 5.9 keV might be due to small variations of the working temperature of the detector, which would result in a broadening of the line at 5.9 keV, but one needs to state that this difference is statistically not significant.

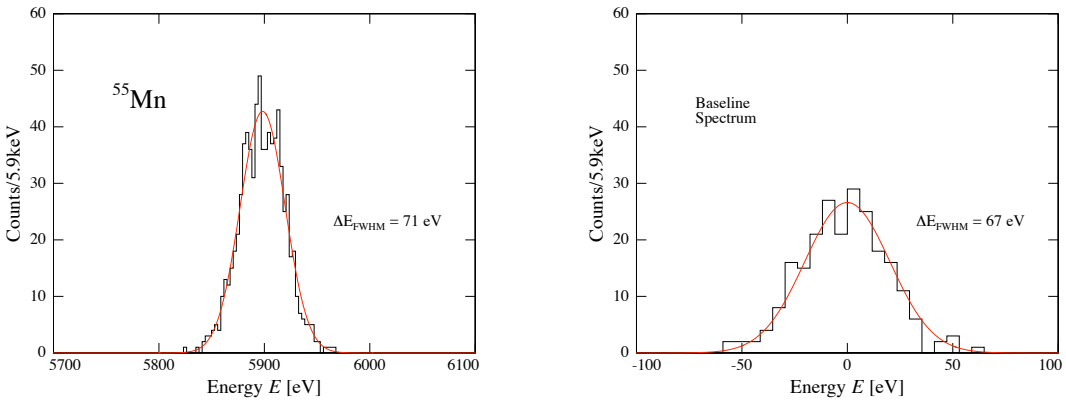

Figure 6.8 In the left diagram the energy spectrum of the K_β-line is shown. By the fit of a gaussian function with a $E_{\mathrm{FWHM}} = 71$eV the peak can be described. The histogram on the right displays the distribution of energies which were assigned to the baselines is. A gaussian fit function with $E_{\mathrm{FWHM}} = 67$eV was used to describe the peak.

Linearity of the Detector

An important detector property is to have a linear relation between deposited energy and amplitude of the detector response. To analyze this property, the measured energies of characteristic lines can be compared to their expected values. An ideal detector would show no discrepancy between the measured and the expected energy. The deviation from a linear behavior has its origin in the temperature dependence of the thermodynamic properties of the sensor and absorber materials. Due to the temperature increase upon the absorption of energy, the heat capacity of the sensor C_s and the dependency of the magnetization on the temperature $\partial M/\partial T$ change. This leads to a smaller amplitude of the detector signal as expected from the linear relation $\delta\phi \propto \delta E$. In fig. 6.9 the measured amplitude of K_α- and K_β-lines are shown

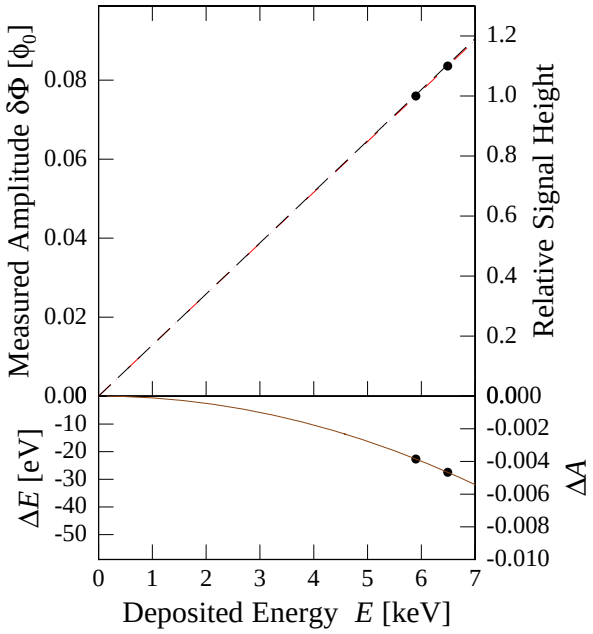

Figure 6.9 Top: Measured amplitude $\delta\phi$ as a function of the deposited energy E in the sensor for the K_α and K_β line from the spectrum shown in fig. 6.7. Bottom: Deviation to the deposited Energy in [eV] and as an amplitude relative to the reference pulse.

as a function of the deposited energy. On the right abscissa the signal amplitude relative to a reference pulse at 5.9 keV is shown. The data points lie on the solid curve which marks a function given by

$$\delta\phi = \frac{\partial\phi}{\partial E}\delta E + \frac{1}{2}\frac{\partial^2\phi}{\partial E^2}\delta E^2 \quad . \tag{6.3}$$

If the detector was linear the data points would lie on the dashed line given by the linear part in equation 6.3. The deviation from linear behavior in units of energy and flux is displayed in the bottom diagram in fig. 6.9 by plotting the quadratic term of equation 6.3 as a function of the deposited energy. At x-ray energies of 5.9 keV and 6.5 keV the relative deviation from linear behavior is $3.9 \cdot 10^{-3}$ and $4.7 \cdot 10^{-3}$, respectively. A correction of the spectrum shown in fig. 6.7 was not done since the effect of this linearization on the derived energy resolution is negligible.

6.5 Thermal Crosstalk

This detector setup consists of two separate magnetic calorimeters on the same substrate which can each be read out by a separate circuit, fulfilling therefore the requirements to analyze thermal crosstalk effects via the substrate. Therefore, the events in both channels were acquired simultaneously in the same time window. Every time the trigger channel acquired a pulse, the other channel was acquired as well.

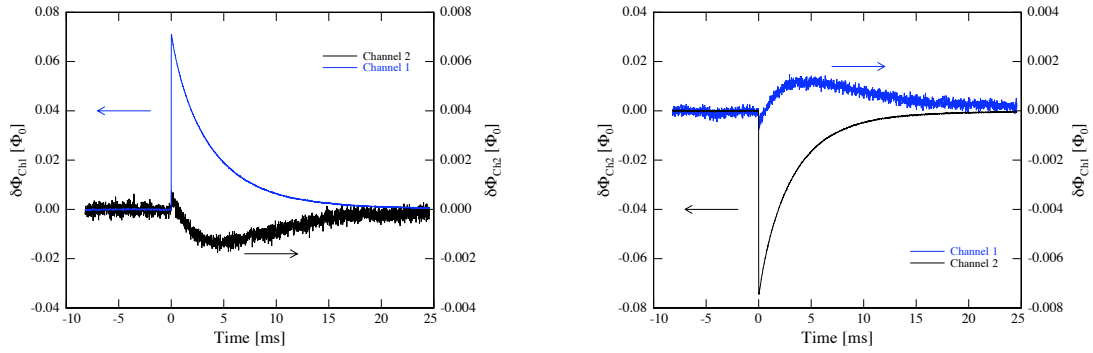

Figure 6.10 Crosstalk at a temperature of 50 mK; Left: Response of both channels while a K_α photon was absorbed in channel one. Right: Response of both channels while a K_α photon was absorbed in channel two.

In fig. 6.10 the time evolution of a K_α pulse which was detected by the one channel as well as the response observed in the other channel is displayed. In the case shown on the left, the trigger was set to the first channel and on the right to the second channel. The pulses were acquired at a stable bath temperature of 50 mK. The response of the channel which was not triggered, the indirect signal, is generated after x-ray absorption in the other detector, when this other detector equilibrates with the substrate and the substrate temperature increases. As a result of this, the rise time of the indirect signal is comparable to the decay time of the direct signal. The amplitude of the indirect signals is in both cases roughly 2% of the amplitude of the direct signals. Looking at the indirect signals in detail, one observes a tiny component with a fast rise time, which might be caused by magnetic crosstalk between the SQUID inductances of the two neighboring detectors.

At a temperature of 100 mK, the same measurement was repeated with the result shown in fig. 6.11. Since the thermal conductivity between the sensor and the substrate increases with temperature, the rise time of the indirect pulses becomes faster and the amplitude becomes larger. At $T = 100$mK the amplitude of the indirect pulse is for both channels roughly 5.5% of the large pulse. This interpretation is only correct if the thermal conductance between the sensor and the chip increases faster with increasing temperature than the one between chip and brass holder. This is indeed expected because the first should be limited by the Kapitza resistance with $G \propto T^3$, whereas the second should be limited by the thermal conductance of the glue layer with $G \propto T^2$.

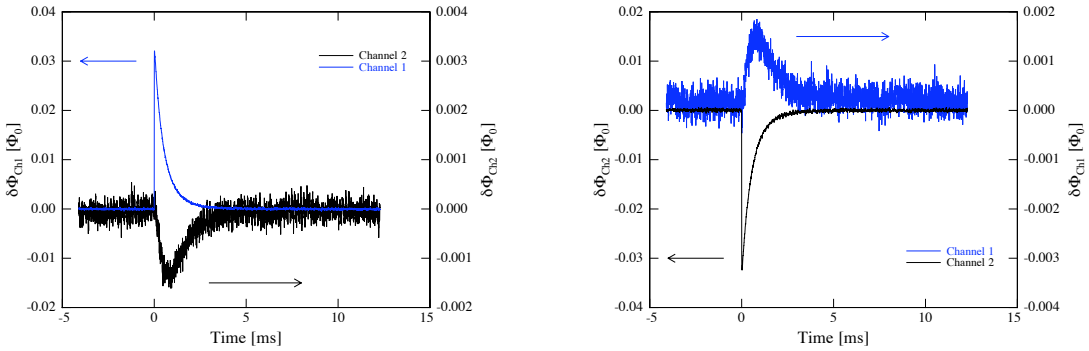

Figure 6.11 Crosstalk at a temperature of 100 mK; Left: Response of both channels while a K_α photon was absorbed in channel one. Right: Response of both channels while a K_α photon was absorbed in channel two.

From this basic analysis two important conclusions can already be drawn. A thermal cross talk of this dimension can compromise the energy resolution of future detector arrays. Assuming that each pixel on the array runs at its maximal count rate, with still only a small amount of pile-up events. In this case the pulses will be distorted on the level of the crosstalk amplitude which was here in the order of several percent. This would lead to a degradation of the energy resolution in the same order of magnitude. However, in applications where a large number of pixels is required to achieve at least a small but tolerable count rate, the distortion of the direct pulses by indirect pulses will be negligible due to the small probability of indirect pulses and therefore the energy resolution will not be compromised. For the future development of arrays a design has to be considered which reduces the thermal conduction via the substrate from one pixel to another to a minimum. An approach which is pursued in the fabrication of Transition-Edge-Sensors (TES) is to heat sink each sensor separately and suspending them from membranes, leaving only small bridges of the full substrate material in between.

6.6 Detector Operation in Open-Loop Mode

Spectroscopic measurements with magnetic calorimeters are usually carried out in flux-locked-loop mode which was already introduced in section 3.2.2. Due to this additional circuitry it is possible to linearize the flux to voltage conversion over a range of several flux quanta.

In the following, a data acquisition technique will be presented which does not make use of the flux-locked-loop circuitry. It will be shown that this method of measuring can be used in the limit of small pulses $\delta\phi < 1/2\phi_0$, which was the case for all spectroscopic measurements carried out in FLL mode during this work. Detector read out without FLL circuitry is very interesting for the application in arrays since once each SQUID is tuned at the right working point, there is no need for a continuos feedback for each channel.

6.6.1 Magnetization Measurement

Figure. 6.12 shows the result of a magnetization measurement in open-loop mode where the magnetic field in the sensor volume is the sum of the parasitic background field discussed above and field caused by a persistent current 20 mA in the meander. The SQUID was biased with a current slightly higher then the lowest critical current.

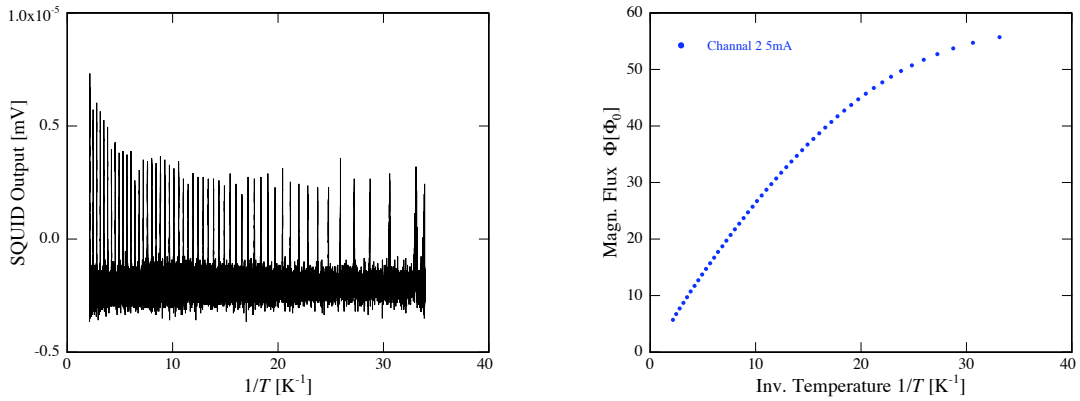

Figure 6.12 Magnetization measurement carried out in open-loop mode. Left: output voltage of the SQUID as a function of the inverse temperature. Right: each point resembles the sum of the flux quanta which have been passed while decreasing the temperature.

Therefore, the SQUID output shows only a finite voltage when the flux in the SQUID loop passes $(n+1/2)\phi_0$. Important to notice is that this is also the only flux interval when there is power dissipation on the chip, reducing the heating on the chip to a minimum. By displaying the number of passed flux quanta as a function of the temperature, which can be seen on the right in fig. 6.16, all information about the magnetization of the sensor is gathered. Since no distortion of the data by power dissipation on the chip can be expected, with this method it is possible to measure more precisely the residual magnetization of the sensor in the parasitic background field without persistent current in the meander.
Figure 6.13 displays the result of this measurement. The observed magnetization shows that indeed a rather large background field must be present in the sensor volume which could be described by an effective current of 55 mA in the meander of pixel 1 and 60 mA in the meander of pixel 2. In terms of magnetic field this corresponds to a mean field of 1.9 mT. How ever, the observed parasitic back ground field can hardly be assumed to have the same geometry as the field produced by the meander and the deduced value for this effective current needs to be interpreted with care.

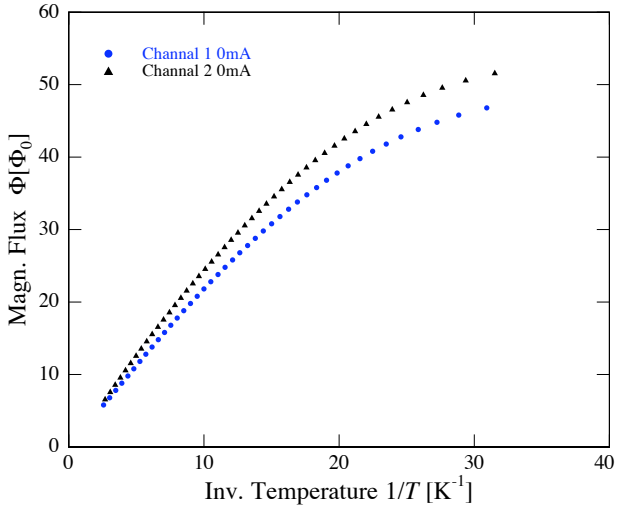

Figure 6.13 Magnetization measurement without a persistent current carried out in open-loop mode. The diagram shows the magnetic flux in the SQUID as a function of the inverse temperature.

6.6.2 Acquisition of Pulses

Power Dissipation

For the analysis of x.ray signals in the open-loop mode, a few considerations have to be made which are not necessary when acquiring in FFL mode. It has to be taken into account that due to small changes of the temperature, the flux in the SQUID loop changes which shifts the working point and consequently also alters the power dissipation. In fig. 6.14 this effect is sketched. According to the initial flux in the SQUID loop which determines the working point, a small positive change of flux can move the working point into regions of higher or lower power dissipation. In fig. 6.14

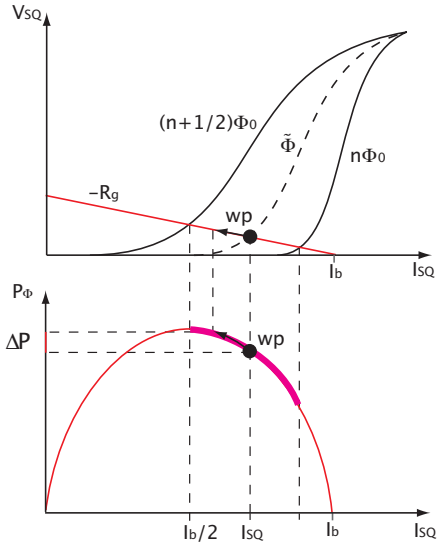

Figure 6.14 The picture on the top shows a schematic I-V-curve of a SQUID. For given bias current all possible working points lie on a line with slope $-R_g$ between the I-V curve for $(n + 1/2)\phi_0$ and $n\phi_0$. The power dissipation corresponding to equation 6.5 is pictured on the bottom. Due to a shifting working point, the power dissipation increases by $\triangle P$.

a situation is displayed, where a working point with a flux $\tilde{\phi}$ in the SQUID loop was chosen where a positive flux change moves the working point towards smaller

currents. An increasing flux shifts the working point to a new position which results in an increased power dissipation. The power dissipation on the chip due to the current I_{SQ} flowing through the SQUID is given by

$$P = V_{\mathrm{SQ}} \cdot I_{\mathrm{SQ}} \ . \tag{6.4}$$

When taking into account that the bias current I_{b} splits into two branches, I_{SQ} and $V_{\mathrm{SQ}}/R_{\mathrm{g}}$, as explained in section 3.7, the power dissipation has a dependence on the SQUID current, given by

$$P = -R_{\mathrm{g}} I_{\mathrm{SQ}}^2 + I_{\mathrm{b}} R_{\mathrm{g}} I_{\mathrm{SQ}} \ . \tag{6.5}$$

This relation has a maximum at $I_{\mathrm{SQ}} = I_{\mathrm{b}}/2$ with a value of

$$P_{max} = \frac{1}{4} I_{\mathrm{b}}^2 R_{\mathrm{g}} \ . \tag{6.6}$$

In combination with the value for the gain resistor, the range of function (6.5) is limited by the I-V curve of the SQUID as shown in figure 6.14. Therefore, the power dissipation depends strongly on the value of I_{b} and in particular on the part I_{SQ} of the bias current flowing through the SQUID. In order to have a monotone relation between voltage output and power dissipation, it is important that the $I_{\mathrm{b}}/2$ is smaller than the lowest critical current of the SQUID or larger than the largest.

Electro-Thermal-Feedback and Pulse Shapes

In the following a qualitative thermodynamic model is given which aims to explain the effect of electro-thermal-feedback effects observed while acquiring pulses in open-loop mode. Fig. 6.15 schematically describes this model. A thermal system is considered which consists of two heat capacities, C_{s} belonging to sensor and absorber and C_{c} belonging to the chip substrate. Since the SQUID and the detector are on the same chip, the biasing of the SQUID effects the temperature of the substrate itself. Assuming a working point is chosen where an input power $P(t) = E \cdot \delta(t)$ in the sensor, caused by the absorption of an x-ray shifts the working point to a region where the power dissipation P_ϕ due to the change of flux in the SQUID is smaller, the temperature of the substrate T_{c} decreases and the temperature difference between the sensor and the substrate becomes larger. The thermalization time becomes shorter.

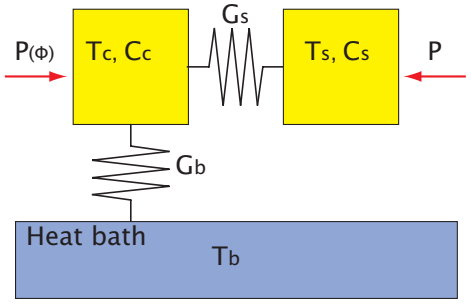

Figure 6.15 Thermal model with two heat capacities C_s and C_c representing the detector and the substrate, respectively. They are thermally connected via links with the thermal conductivity G_{s} and G_{b}.

For the other case, in which a temperature pulse in the sensor results in an increasing P_ϕ, the thermalization times of the pulses will become slower.

In order to increase the count rate of the detector it is very important to reduce the decay time of pulses. A good understanding of open-loop acquisition will therefore provide valuable information for the development of fast detectors.

Finding the Optimal Working Point

Three working points of a two stage SQUID read out are marked in fig. 6.16 by the letters A), B) and C). The characteristics which these working points belong to were obtained by changing the external flux ϕ_b fed into the detector SQUID. A temperature pulse corresponding to an identical change of flux $\triangle\phi$ in the sensor results in different pulse amplitudes depending on the working point. The pulses observed while operating the read out SQUID in working point A) have a larger amplitude compared to the pulses belonging to working point B) and C). This is simply due to a larger voltage-to-flux transfer coefficient at point A). For B) and C) the pulse amplitude is the same but they are pointing in opposite directions. Therefore, in open-loop mode, the voltage pulse can have different amplitude and sign, for the same flux change into the SQUID. The same amplitude of the pulses

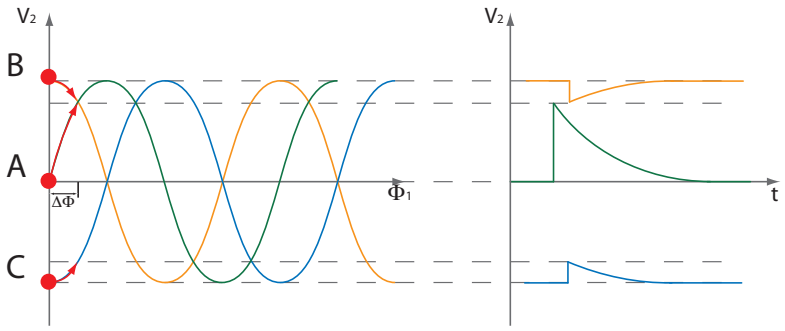

Figure 6.16 On the left side a SQUID characteristic is shown with three different working points. On the left side the pulse shaped obtained at each working point is sketched.

observed when operating the read out SQUID in working point A can be obtained in four different working points marked in fig. 6.17 with A), D), E) and F). At each of these working points a pulse generates a different power dissipation. Since the minimum SQUID voltage out put level belongs to the case $n\phi_0$, working point A) corresponds to $\tilde{\phi} \simeq (n+1/4)\phi_0$ and a temperature pulse will move the working point closer to the curve $(n+1/2)\phi_0$. In this case the power dissipation on the chip P_ϕ will increase. Point D) corresponds to a flux in the SQUID loop of $(n+1/2)\phi_0 < \tilde{\phi} < (n+3/4)\phi_0$. Therefore, a temperature pulse will result in a smaller P_ϕ and a pulse in negative direction. The flux in the detector SQUID at working point E) is again $(n+1/4)\phi_0$, but the pulses point in negative direction and the power dissipation becomes smaller upon a positive change of flux. The operation of the detector SQUID at working point F) shows the lowest starting power dissipation

before a temperature pulse occurs, but upon a temperature pulse the working point is shifted in a way that P_ϕ increases. From these considerations point E is the preferable working point, since the intrinsic power dissipation is low and the pulse decay fast due to negative electro-thermal-feeback.

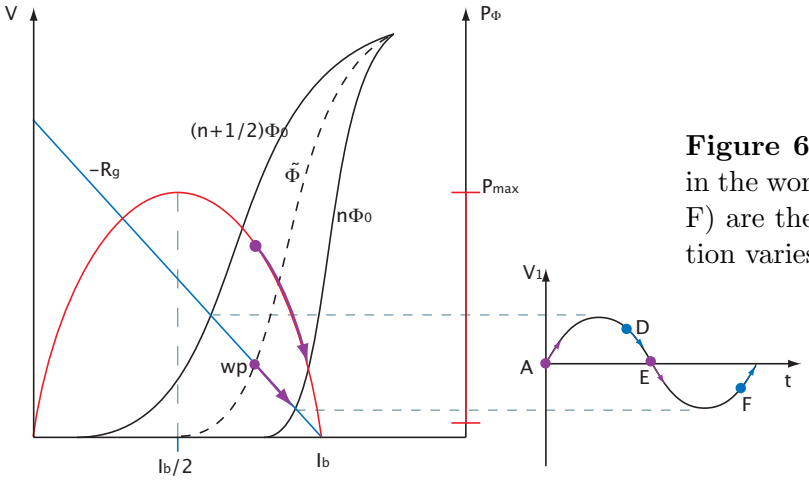

Figure 6.17 The pulse amplitude in the working points A), D), E) and F) are the same but the thermalization varies from point to point.

Fig. 6.18 displays three pulses acquired under identical conditions, at a bath temperature of $T = 23$mK, an injected current of $I_0 = 100$mA and one constant bias current I_b. The pulses are normalized to the same hight to analyze the decay time. The pulse with the medium decay time was acquired in FLL mode and the time evolution of the pulse depends only on the value of the heat capacity and the thermal conduction between the sensor and the substrate. The other two pulses were acquired in open-loop mode and their different decay time depends on the working point. The pulse with a fast decay time corresponds to a change of flux which generates a reduced power dissipation on the chip.

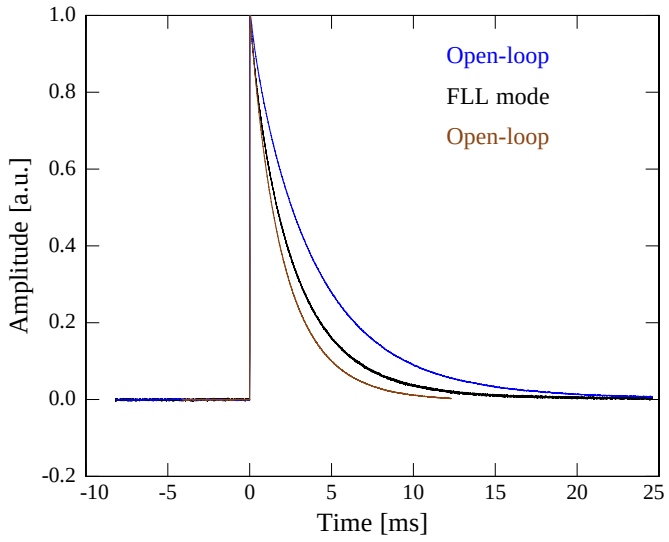

Figure 6.18 Pulses obtained in different acquisition modes. The pulses with the fastest and the slowest decay time were acquired in open-loop mode at two different working points. The pulse with medium long decay time was acquired in FLL-mode.

A point left out of the discussion so far is the noise. In general, flux noise that is dependent on the voltage-to-flux coefficient of the SQUID like it is the case for magnetic Johnson noise in open-loop, is very complicated to describe. However, to minimize the noise contribution from the read out electronics the best working point can be identified by the largest voltage-to-flux transfer coefficient $\partial V/\partial\phi_1$. Since this is also the point where the amplitude of the pulses is maximized, the optimization of the pulse height automatically reduces the noise to a minimum.

Linearity

The linear relation between the change of temperature and the change of magnetization in the sensor material given by equation 2.2 is a reasonable approximation for small changes of temperature. Once the relation between temperature and flux is linear, the FLL mode read out of the SQUID linearizes also the relation between voltage and flux. In open-loop mode the voltage-to-flux characteristics is of course not linear, but for signals with an amplitude smaller then $0.5\phi_0$, the relation between voltage and flux is monotonically either rising or falling.

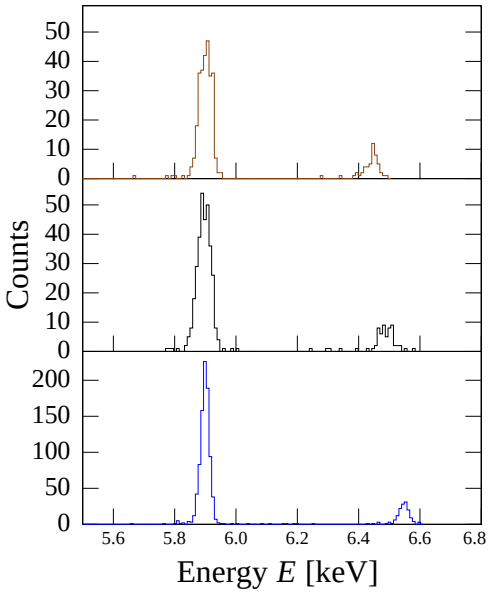

Figure 6.19 Middle: Spectrum acquired in FLL mode. K_α and K_β line lie at the exact positions. Top and bottom: Spectra acquired in open-loop mode. The K_β was used as a reference line and lies at 5.9 keV. The deviation from a linear behavior of the detector can be seen from the shifted position of the K_α line.

An example of three acquired ^{55}Mn spectra are displayed in fig. 6.19. The spectrum in the middle was acquired in FLL mode. In this case the relation between energy and SQUID output voltage is linear to within better then 0.5%. The other two spectra were acquired in open-loop mode. In the first one, the center of the K_β line is shifted towards smaller energies while in the third spectrum, the same line is shifted to higher energies. In each spectrum the K_α line lies at the right energy value since it was used as a reference line during the acquisition. The shifted line positions can be explained by the non linear relation between voltage and flux. In fig. 6.20 the SQUID characteristics of the two stage setup used in this experiment is shown.

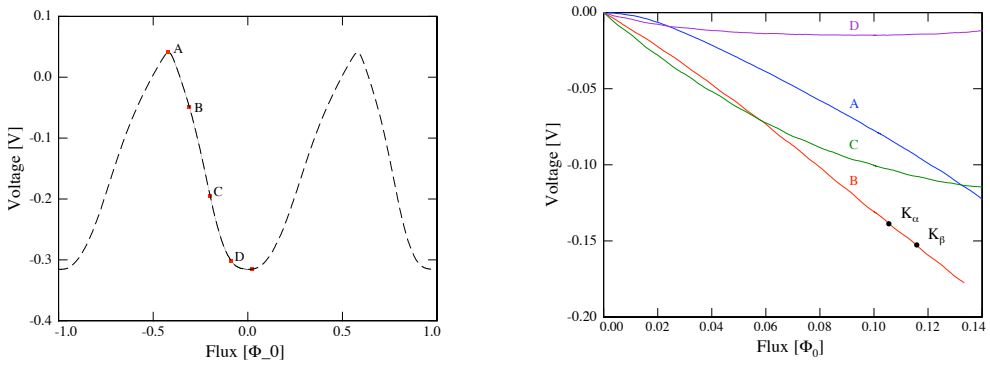

Figure 6.20 Voltage-to-flux characteristics of the two stage SQUID setup used in this experiment with four possible working points labeled A) through B)

On one slope four possible working points are indicated, labeled A) through D). The figure on the right shows four short parts of this voltage characteristics, each of them starting in one of the four labeled working points. A constant voltage is added to these curves to shift the voltage at the working point to zero. An acquisition of pulses in a working point with a curvature as in point A) would result in a spectrum like the one shown in the top diagram of fig. 6.19 while a curvature like in working point C) leads to a spectrum like the last one in fig. 6.19.

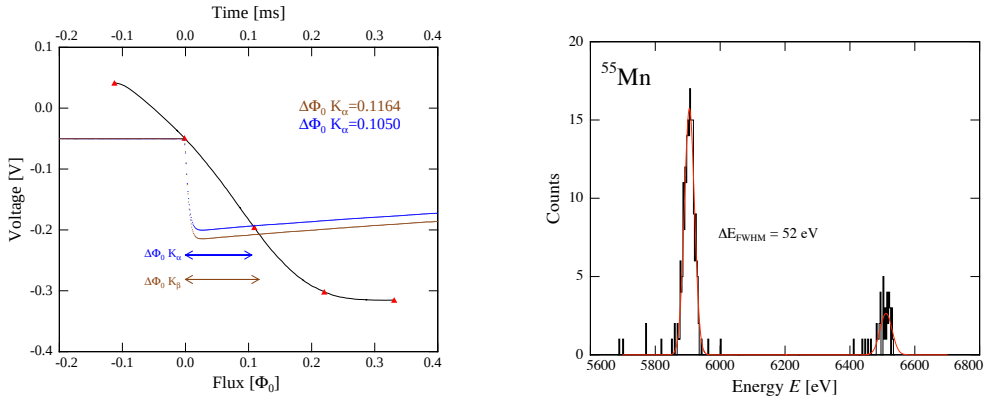

Figure 6.21 Left: The voltage pulses themselves are displayed in together with the corresponding part of the SQUID characteristics. Right: non-linearized spectrum. The voltage response is almost linear in the energy range of the K_α and K_β

In one of the experiments, the working point of the detector SQUID was chosen to be B) and K_α and K_β photons of ^{55}Mn were acquired. The signal size of the corresponding voltage pulses are shown by the two data points on curve B) labeled with K_α and K_β. The voltage pulses themselves are displayed in fig. 6.21 (left), together with the corresponding part of the SQUID characteristics, in order to show the relation between signal size and underlying flux change as direct as possible. In

this case the working point provided an almost linear voltage response in the energy range of the K_α and K_β photons, as can also be seen in the non-liearized energy spectrum on the right hand side of fig. 6.21.

In the general case, the non-linear behavior can be a lot more pronounced. However, since the working point of the detector can be identified by the DC-level of the SQUID output signal and the polarity of the voltage pulses, and since the shape of the SQUID characteristics can be determined precisely, one will always find a unique and well defined function, that relates the size of the open-loop-voltage pulse to the underlying change of flux and with this to the energy deposited in the detector. It seems therefore feasible that MMCs in open-loop are used in x-ray spectroscopy, greatly reducing the complexity of the readout electronics, a detail of special importance on the way to large detector arrays.

7. Summary

In the this work the development of metallic magnetic calorimeter detectors and their characterization by means of spectroscopic measurements were presented. A MMC type detector consists of a paramagnetic temperature sensor placed in a weak magnetic field. Upon the energy deposition in the detector a temperature rise generates a change in magnetization in the sensor which is read out by a low noise SQUID magnetometer in a two stages configuration.

Taking the interaction mechanisms into account which are present among magnetic moments in metals as well as the interaction of these magnetic moments with the magnetic moment of a nucleus a good understanding of the thermodynamic properties of the sensor material Au:Er can be achieved. This allows for numerical calculations of the magnetization of the sensor, pulse height and noise contributions. Considering an application for x-ray spectroscopy on highly charged ions at the Heidelberg EBIT a new detector design, based on the SQUID chip MagCal 15 was numerically optimized. The optimization of the detector was carried out in order to have a high quantum efficiency for x-rays according to the requirements of the EBIT experiments. This turns out to constrain the absorber thickness to 5μm. Moreover the fixed geometry of the SQUID, the given erbium concentration of the Au:Er target, together with the volume of the absorber, reduced the number of parameters that can freely be adjusted to optimize the resolving power to only two which are the area and the height of the sensor. This optimzation resulted in a sensor with an area of 160x160μm^2 and a thickness of 1.5μm, the gold absorber has the dimensions 250x250x5μm^3 which alltogether results in a mushroom shaped detector geometry. A microfabrication process was developed which allows for detector array preparation. By means of this process, two detector pixels were patterned onto two meander-shaped SQUIDs which were read out by separate channels. Due to problems in the fabrication process, the obtained absorber dimensions deviate in area compared to the values obtained from the numerical optimization. Nevertheless, both detectors showed a similar performance and a characterization was carried out by measuring the magnetic properties of the sensor and analyzing the detector response upon the absorption of x-rays emitted by an external ^{55}Fe-source . The detector was operated in a liquid helium bath cryostat which cools the experiments to working temperatures below 100 mK by means of adiabatic demagnetization.

Two sets of experiments were performed. In the first, the detector readout was operated in the flux-locked-loop mode, which is used to maintain a stable working point. Three different persistent currents were prepared in the meander. The magnetization measurements and the pulse shapes at different temperatures were analyzed. A full spectrum was discussed which showed an energy resolution at 6 keV of $\Delta E_{\mathrm{FWHM}} = 71$eV and a baseline width of 67 eV. Due to a very high power dissipation by currents flowing through the feedback coil of the SQUID, the sensor temperature was always higher then 60 mK. Another problem encountered while

measuring was a parasitic magnetic field in the sensor material which strongly influenced the magnetization measurement and the size of detector signals. Moreover in order to analyze the magnetic and thermal crosstalk between the two detectors, contemporaneous time windows were recorded containing the simultaneous signal from the two detectors. For the first time it was possible to quantify the crosstalk when two detectors are running on the same silicon substrate. The result of this measurement was that a thermal crosstalk was present on the level of few percent, while the magnetic crosstalk has smaller influence.

To better interpret the measurements discussed above, a second set of experiments was carried out in which the readout electronics was operating in open-loop mode. With an adequate tuning of the SQUIDs a new way of measuring the magnetization was established which minimizes the power dissipation due to SQUID biasing and feedback currents. In this mode the distorsions due to parasitic heating were eliminated from the magnetization curve and due to the lower power dissipation a lower temperature was reached on the SQUID chip. The magnetization measurements carried out in open loop mode also strongly confirmed the presence of a residual magnetic field in the region of the detectors which is independent of the current in the ADR magnet. The thermal response upon the absorption of x-rays was analyzed. A very interesting electro-thermal effect was observed which is due to a change of power dissipation during the pulse formation, according to the fact that the SQUID changes its working point after a change of magnetic flux. The main result of this effect is that the decay time of the detector signals is modified depending on the working point. It has been shown how to tune the SQUIDs to create faster pulses in order to allow for higher count rates. A drawback of the open loop mode spectrum acquisition, is the intrinsic non linearity. However, due to the possibility to reconstruct the working point, the relation between measured voltage and energy can be easily linearized. Reading out detectors in the presented way holds a great opportunity for future detector arrays to minimize the power dissipation and to reduce the amount circuitry. The thorough theoretical understanding of the thermodynamic processes of the calorimetric detection principle, the possibility of microfabricating arrays and the excellent results proven to be achievable with these detectors, show that metallic magnetic calorimeters have a great future potential which still has to be exploited.

Bibliography

[Ban93a] S.R. Bandler. The magnetization of localized spins in metals is discussed as a sensor for low temperature calorimetric detection of particles. *Journal of Low Temperature Physics*, 1993.

[Ban93b] S.R. Bandler. Metallic magnetic bolometers for partical detetction. *Journal of Low Temperature Physics*, 93(3):709–714, 1993.

[Büh88] M. Bühler. A magnetic bolometer for single-particle detection. *Europhysics Letters*, 1988.

[CA03] Pierre Curie and A.Laborde. *Séance, Academie Science Paris*, 136:673, 1903.

[CAB03] J. Clark and editors A.I. Barginski. *The Squid Handbook: Fundamentals and Technology*. John Wiley and Sons, 2003.

[CE05] Siegfried Hunklinger Christian Enss. *Low Temperature Physics*. Springer, 2005.

[Dan05] T. Daniyarov. *Metallische magnetische Kalorimeter zum hochauflösenden Nachweis von Röntgenquanten und hochenergetischen Molekülen*. PhD thesis, Kirchhoff-Institut für Physik, Universität Heidelberg, 2005.

[Dav73] D. Davidov. Crystalline-field effects in the electron-spin resonance of rare earths in the noble metals. *Phys. Rev. B*, 8(8):3563–3568, 1973.

[DH05] C.Hinnrichs D.Drung and H.Bartelmess. A low-noise ultra-high-speed dc squid readout electronics. *ISEC*, 2005.

[Fle03] Andreas Fleischmann. *Magnetische Mikrokalorimeter: Hochauflösende Röntgenspektroskopie mit energiedispersiven Detektoren*. PhD thesis, Kirchhoff-Institut für Physik, Universität Heidelberg, 2003.

[Fle05] A. Fleischmann. *Metallic Magnetic Calorimeters*. Springer, 2005.

[Hah92] W. Hahn. Crystal field excitations in dilute rare earth noble metal alloys. *Physica B*, 27(10):670–671, 1992.

[Her00] T. Herrmannsdörfer. Properties of er-doped au at ultralow temperatures. *Physica B*, 284-288:1698–1699, 2000.

[Höl97] G. Hölzer. $k_{\alpha_{1,2}}$ and $k_{\beta_{1,3}}$ x-ray emission lines of the 3d transiton metals. *Phys. Rev. A*, 1997.

[Joh28] J.B. Johnson. Thermal agitation of electricity in conductors. *Phys. Rev.*, 32(1):97–109, 1928.

[Jos62] B.D. Josephson. *Physical Review Letters*, 1962.

[Lin07] M. Link. *Entwicklung eines meatallischen magnetische Kalorimeters für die hochauflösende Röntgenspektroskopie*. PhD thesis, Kirchhoff-Institut für Physik, Universität Heidelberg, 2007.

[Lon50] F. London. *Superfluids*. Wiley, New York, 1950.

[Nyq28] H. Nyquist. Thermal agitation of electric charge in conductors. *Phys. Rev.*, 32(1):110–113, 1928.

[Rön96] W.C. Röntgen. *Sience*, 3(227):726, 1896.

[Sch00] J. Schönefeld. *Entwicklung eines mikrostrukturierten magnetischen Tieftemperaturkalorimeters zum hochauflösenden Nachweis von einzelnen Röntgenquanten*. PhD thesis, Kirchhoff-Institut für Physik, Universität Heidelberg, 2000.

[Sim35] F. Simon. *Nature*, 135:763, 1935.

[SS75] M.E. Sjöstrand and G. Seidel. Hyperfine resonance properties of er^3+ in au. *Phys. Rev. B*, 11(9):3292–3297, 1975.

[Tes77] C.D. Tesche. Dc squid: noise and optimization. *Jornal of Low Temperature Physics*, 1977.

[WH69] G. Williams and L.L. Hirst. Crystal-field effets in solid solutions of rare earths in nobel metals. *Phys. Rev.*, 185(2):407–415, 1969.

Acknowledgments

In looking back on the last year, there have been many persons supporting me in equally many ways. While writing this I am thinking of friends, family and my girl friend who were always there with an opinion when asked for, ready to give an advice when needed and for any diversion when it was necessary. An overwhelming experience was the team work throughout the F3 and F4 group. Although everyone has an individual project a major part in every thesis is for the benefit of the whole group. This is in the end a credit of Christian Enss who I have got to know as a true patron, never avoiding any effort to improve the atmosphere in the group and the quality of the research work. I am especially grateful for the tutoring by Andreas and Loredana Fleischmann whose dedication, intuition and ability to solve problems in no-time has led me through many difficulties and pushed me through the last couple of days of writing. Last but not least, I am very thankful for the help of Thomas Wolf whose clean and thoughtful way of working I have learned to appreciate. With great time and effort he makes it possible to use all microfabrication techniques, this thesis depended on so much.